UNIVERSITY OF LIVERPOOL

Carbocations in Heterogeneous Catalysis Caught in the Act by (Dynamic Nuclear Polarization Enhanced) Multidimensional and Multinuclear Nuclear Magnetic Resonance

Thesis submitted in accordance with the requirements of the University of Liverpool for the degree of Doctor in Philosophy

by

Dong Xiao

Department of Chemistry

August 2019

Carbocations in Heterogeneous Catalysis Caught in the Act by (Dynamic Nuclear Polarization Enhanced) Multidimensional and Multinuclear Nuclear Magnetic Resonance

Dong Xiao

Abstract

Probing and determining the carbocation intermediates formed during heterogenous catalytic reactions are crucial steps for understanding the reaction mechanisms, such as the methanol to hydrocarbon (MTH) reaction. Nevertheless, the observation of carbocations and their structural identification are not straightforward as they are reactive, transient, difficult to capture and exist in generally low concentrations and therefore their spectroscopic characterization is very challenging. Solid-state NMR is useful in detecting reactive carbocations on solid catalysts. However, previous NMR studies of carbocations were only limited to the use of one-dimensional (1D) NMR methods combining with some indirect methods to elucidate the carbocation structures, those methods require prior assumption of possible structures and may lead to misinterpretation. In this thesis, the carbocation intermediates formed in various zeolite catalysts under MTH conditions are directly identified *via* multidimensional NMR techniques which provide unambiguously experimental support for previously proposed structures and more importantly identify previously undetected ones. Moreover, the interactions between the confined carbocations and zeolite framework are quantitatively probed by multinuclear NMR methods. Since low sensitivity of NMR is also key limiting factor challenging NMR studies of carbocations, the advanced sensitivity enhancement technique known as dynamic nuclear polarization (DNP) is successfully applied to the detection of carbocations and their subsequent multidimensional and multinuclear NMR studies. These successful applications of DNP provide new opportunities for research on carbocations.

Acknowledgements

First, I would like to express my sincere gratitude to my primary supervisor Dr. Frédéric Blanc for the guidance and help he has offered me throughout my two years of this PhD in Liverpool and his continuous support on my PhD project after my return to Dalian Institute of Chemical Physics (DICP), China. His help and guidance enable me to publish four papers which are prerequisites for doctoral degree in DICP. I am grateful to BP, University of Liverpool and DICP for the dual PhD scheme and a studentship (75139) funding this scheme.

My sincere thanks also go to my co-supervisors Prof. Xinhe Bao and Prof. Xiuwen Han who have given me guidance and help in DICP. I also thank Prof. Shutao Xu for his collaboration on some sample preparation, and Prof. Guangjin Hou and my colleagues in DICP for their great help.

Many work in this thesis were conducted in different facilities, accesses and travel grant from EPSRC (EP/M00869X/1) for Frédéric to these facilities are acknowledged. I would like to thank Dr. Subhradip Paul (University of Nottingham), Dr. Shane Pawsey (Bruker BioSpin), and Dr. Fabien Aussenac (Bruker BioSpin) for their generous help with the instruments in these facilities. The UK 850 MHz solid-state NMR Facility used in this research was funded by the EPSRC and BBSRC (contract reference PR140003), as well as the University of Warwick via part funding through Birmingham Science City Advanced Materials Projects 1 and 2 supported by Advantage West Midlands (AWM) and the European Regional Development Fund (ERDF). Collaborative assistance from the 850 MHz Facility Manager (Dr. Dinu Iuga, University of

Warwick) is acknowledged.

Many thanks to my colleagues Dr. Nick J. Brownbill, Kenneth K. Inglis and Ashlea R. Hughes in Liverpool for their support in NMR experiments and fruitful discussions and suggestions. I also thank Dr. Jonathan A. Iggo, Dr. Konstantin Luzyanin for their help in Liverpool.

Last, I would like to express my deepest gratitude to my family for their endless love and support, without them I wouldn’t have achieved anything. I am grateful to have Peipei as my partner who helped me enormously.

Awards, Presentations and Publications

Awards

2016-2017 Studentship of BP-University of Liverpool-Dalian Institute of Chemical Physics

2017 The UK 850 MHz Solid-state NMR facility PhD travel fund for Alpine Conference on Solid-State NMR

Presentations

2017 Round Table Talk at the 10th Alpine Conference on Solid-State NMR

2017 Poster at the 10th RSC Annual NMR Discussion Group Postgraduate Meeting

2016 Poster at the 9th RSC Annual NMR Discussion Group Postgraduate Meeting

Publications

"Direct structural identification of carbenium ions and investigation of host–guest interaction in the methanol to olefins reaction obtained by multinuclear NMR correlations". **D. Xiao**, S. Xu, X. Han, X. Bao, Z. Liu and F. Blanc, *Chemical Science*., 2017, **8**, 8309–8314. *(Chapter 2 of this thesis)*

"Fast detection and structural identification of carbocations on zeolites by dynamic nuclear polarization enhanced solid-state NMR". **D. Xiao**, S. Xu, N.

J. Brownbill, S. Paul, L.-H. Chen, S. Pawsey, F. Aussenac, B.-L. Su, X. Han, X. Bao, Z. Liu and F. Blanc, *Chemical Science*., 2018, **9**, 8184–8193. *(Chapter 4 of this thesis)*

"Identification of different carbenium ion intermediates in zeolites with identical chabazite topology *via* ^{13}C-^{13}C through-bond NMR correlations". **D. Xiao**, X. Han, X. Bao, G. Hou and F. Blanc, *RSC Advances*., 2019, **9**, 12415–12418. *(Chapter 3 of this thesis)*

"Oxidative desulfurization of diesel fuel catalyzed by polyoxometalate immobilized on phosphazene-functionalized silica"
M. Craven, **D. Xiao**, C. Kunstmann-Olsen, E. F. Kozhevnikova, F. Blanc, A. Steiner and I. V. Kozhevnikov, *Applied Catalysis B: Environmental*., 2018, **231**, 82–91. *(not included in this thesis, as it is a collaborative project and is outside the topic of this thesis)*

List of Abbreviations

CHA	Chabazite
CP	Cross-Polarization
CSA	Chemical shift anisotropy
CW	Continuous-wave
DARR	Dipolar Assisted Rotational Resonance
DFT	Density Functional Theory
DICP	Dalian Institute of Chemical Physics
DNP	Dynamic Nuclear Polarization
DNP-SENS	DNP surface enhanced NMR spectroscopy
EPR	Electron Paramagnetic Resonance
FWHM	Full Width at Half Maximum
GC-MS	Gas Chromatography-Mass Spectrometry
HCP	Hydrocarbon Pool
HMQC	heteronuclear multiple quantum correlation
INADEQUATE	Incredible Natural Abundance DoublE QUAntum Transfer Experiment
IR	Infrared spectroscopy
MAS	Magic Angle Spinning
µw	Microwave
M-β	Microporous β-zeolite
MMM-β	Micro-Meso-Macroporous β-zeolite
MTH	Methanol to Hydrocarbons
MTO	Methanol to Olefins
NMR	Nuclear Magnetic Resonance
PDSD	Proton Driven Spin Diffusion
REDOR	Rotational Echo DOuble Resonance
rf	radio-frequency
S/N	Signal-to-Noise
S-RESPDOR	Symmetry-based Resonance-Echo Saturation-Pulse DOuble-Resonance sequence
TCE	1,1,2,2-tetrachloroethane
UV-Vis	Ultraviolet–visible spectroscopy
WHSV	Weight Hourly Space Velocity
1D	One-dimensional
2D	Two-dimensional

Contents

Chapter 1: Introduction

1.1 Nuclear Magnetic Resonance (NMR) spectroscopy

1.1.1 Energy levels and vector model

NMR spectroscopy is a very powerful and versatile analytical technique which has been widely used for structural characterization in various fields such as organic synthesis. The nuclei that can be studied by NMR must be those with a nuclear spin quantum number $I \neq 0$. These nuclei possess a magnetic moment and can interact with a magnetic field, which is prerequisite to generate NMR signals. For these nuclei, there are $(2I+1)$ spin states which are degenerate in the absence of an external magnetic field. However, the introduction of a magnetic field will break this degeneracy. As a consequence, each of the $(2I+1)$ spin states will have slightly different energies. This phenomenon is called the Zeeman effect. These $(2I+1)$ spin states were specified by another quantum number m (whose values vary from $-I$ to I in integer steps). For spins with $I = 1/2$ (^{1}H, ^{13}C, ^{29}Si, *et al*), there are two spin states with $m = 1/2$ (α state) and $-1/2$ (β state). The α and β states sometimes are also denoted as “spin up” and “spin down”, respectively (as shown in Figure 1.1(a)). The energy gap between these spin states can be described by the following equation (also shown in Figure 1.1(b)):

$$\Delta E = \frac{h}{2\pi}\gamma B_0 \qquad \text{Equation 1.1}$$

where γ is the gyromagnetic ratio of the nuclei (rad $\cdot$ s^{-1} $\cdot$ T^{-1}), h is Planck’s constant (J $\cdot$ s) and B_0 is the external magnetic field (T).[1,2]

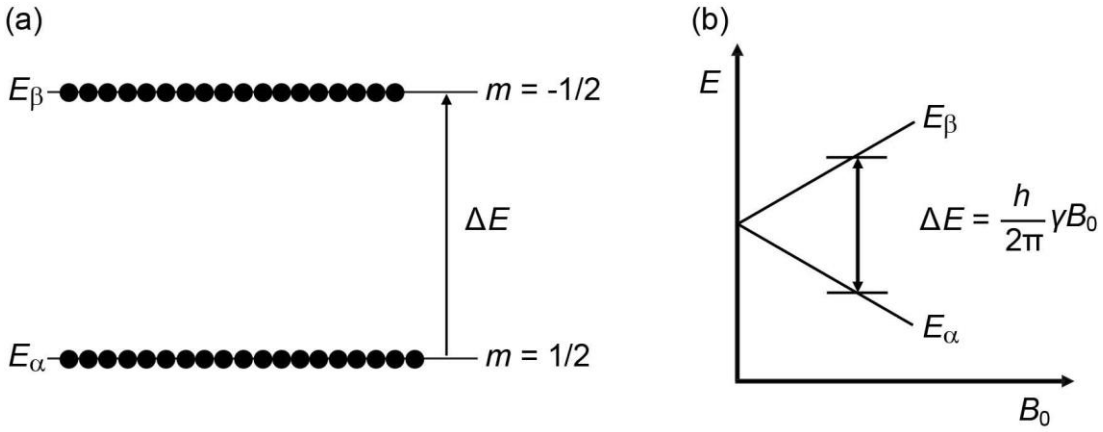

Figure 1.1 (a) Distribution of nuclear spins at α and β states with an energy gap of Δ*E*. (b) Splitting of spin states against an increasing magnetic field B_0.

The transitions between spin states are induced by radio-frequency (rf) waves and will generate NMR signals. These signals will then be Fourier transformed to the commonly known NMR spectra. We refer the peaks observed as having a certain chemical shift (*vide infra*). The intensity of these spectroscopic transitions is dependent on the difference in populations of spin states at equilibrium, which can be expressed using Boltzmann's equation:

$$\frac{n_\beta}{n_\alpha} = e^{-\frac{\Delta E}{k_B T}} \qquad \text{Equation 1.2}$$

where n_β and n_α are the number of spins at the α and β spin states, k_B is Boltzmann's constant, and Δ*E* is the energy gap between the two spin states.[1] For ^{1}H at 9.4 T (a typical magnetic field strength used in NMR) and 300 K, the population difference of both energy levels is n_β/n_α = 0.999936, which is extremely small (1 in 20000). Therefore, NMR signals are inherently weak.

The Larmor frequency *v* (unit in "Hz") of a nucleus depends on its gyromagnetic ratio and the strength of the surrounding magnetic field B_0, which is defined by the following equation:

$$\nu = -\frac{\gamma B_0}{2\pi} \qquad \text{Equation 1.3}$$

The above description of NMR spectroscopy is in terms of energy levels and transitions between these levels.[1] NMR spectroscopy can also be described using the vector model. In the absence of a magnetic field and at thermal equilibrium, the magnetic moments of nuclear spins can align in any direction with no net magnetic moment present (as shown in Figure 1.2(a)). When an external magnetic field B_0 is introduced, the magnetic moments tend to align along the direction of the applied field, yielding a net magnetic moment which is called the bulk magnetization along B_0 at thermal equilibrium (Figure 1.2(b)). The introduction of B_0 will also induce the magnetic moments rotating about the direction of B_0 at frequency ν whose value is defined by equation 1.3. This particular motion is called Larmor precession and ν is also called Larmor frequency. The direction of rotation depends on the gyromagnetic ratio γ. For $\gamma > 0$ (*e.g.* ^{1}H, ^{13}C) the precession is clockwise, as shown in Figure 1.2(b), while the procession of negative γ (*e.g.* ^{15}N) is anti-clockwise. The bulk magnetization also rotates around B_0 at frequency ν when the magnetization vector is tilted away from the magnetic field (Figure 1.2(c)). Such tilt can be accomplished by applying rf pulses. In NMR we manipulate the magnetization vector by a combination of pulses and detect the precession of the magnetization vector.[1,2]

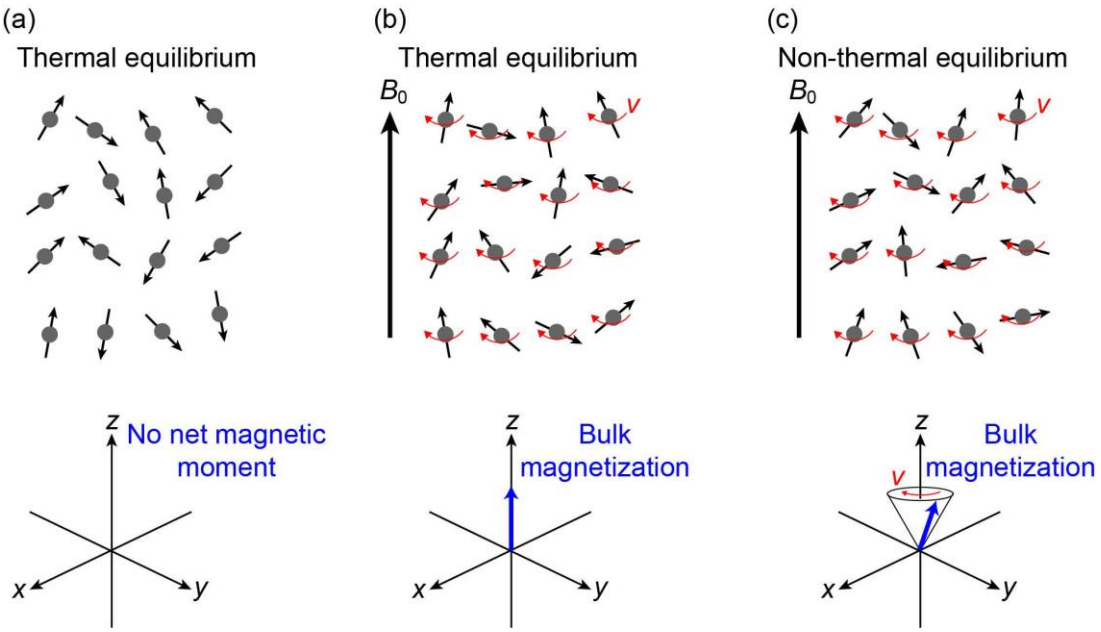

Figure 1.2 (a) Magnetic moments at thermal equilibrium in the absence of a magnetic field. (b) Procession of magnetic moments at thermal equilibrium in a magnetic field B_0 and the corresponding bulk magnetization. (c) Magnetic moments not at thermal equilibrium, which can be induced by applying rf pulse irradiation in a magnetic field B_0 and the Larmor precession of the bulk magnetization.

Equation 1.3 indicates that nuclei of the same isotope should have the same NMR frequency v when located in the same magnetic field B_0 which is certainly not true. This is only valid for isolated spins with their surroundings neglected which are rather idealized conditions. The nuclei in real samples are located in certain electronic environments. The motion of electrons surrounding the nuclei will generate a magnetic field induced by the external magnetic field B_0, altering the strength of the actual local field applied to the nuclei and the corresponding NMR frequency. Therefore, although NMR detects the signals from the nuclei, the signals are very sensitive to local electronic environments, which makes NMR spectroscopy a widely used

technique for characterizing molecular structures or local electronic structures of nuclei.

Considering the effects of surrounding electrons, the actual field that a nucleus can feel is denoted as B_{loc}, which is defined by the following equation:

$$B_{loc} = B_0 + B_{induced} \qquad \text{Equation 1.4}$$

with $B_{induced} = - \sigma B_0$, combined with expression 1.4, gives:

$$B_{loc} = B_0 (1 - \sigma) \qquad \text{Equation 1.5}$$

where B_0 is the external magnetic field, σ refers to chemical shielding. As a result, the resonance condition becomes:

$$\nu = - \frac{\gamma B_0}{2\pi} (1 - \sigma) \qquad \text{Equation 1.6}$$

For nuclei at varied chemical environments, they suffer from different chemical shielding effects, resulting in the difference of the frequency of their NMR signals. For convenience, the frequencies are quoted relative to an agreed reference compound, *e.g.* tetramethylsilane (TMS) for ^{1}H and ^{13}C and ^{29}Si NMR. The differences between sample and reference compounds are usually very small, therefore it is a practical standard to convert these values into parts per million. The chemical shift δ is thus defined:

$$\delta = 10^6 \frac{\nu - \nu_{ref}}{\nu_{ref}} \qquad \text{Equation 1.7}$$

with its unit being “ppm” (parts per million).[1]

1.1.2 Solid-state NMR spectroscopy

In NMR, there are several interactions within the molecule that will affect the lineshape and the positions of NMR signals. These interactions can be

described quantum mechanically by appropriate nuclear spin Hamiltonians in the following equation:

$$\hat{H} = \hat{H}_Z + \hat{H}_{CS} + \hat{H}_D + \hat{H}_J + (\hat{H}_Q) \qquad \text{Equation 1.8}$$

The Hamiltonians from left to right are corresponding to the Zeeman effect, chemical shift, dipolar coupling, scalar coupling and quadrupolar coupling (for $I > ½$ nuclei only), respectively. The magnitude of these interactions is shown in Table 1.1. In liquid-state NMR, the anisotropic part of chemical shift, dipolar interaction and quadrupolar interaction are averaged to 0 by the rapid molecular tumbling, leading to spectra of high resolution with narrow peaks. In solid-state NMR, the restricted molecular motion cannot average out those interactions. These anisotropic interactions in combination with the range of molecular orientation *vs* B_0 in the solid materials result in much broader peaks. Although those broad peaks in solid-state NMR spectra are difficult to interpret, they contain a wide range of structural information and are therefore much more informative.

Table 1.1 Size of the NMR interactions in solids

Hamiltonian	Interaction	Magnitude
$\hat{H}_Z$	Zeeman effect	MHz
$\hat{H}_{CS}$	Chemical Shift	Hz ~ MHz
$\hat{H}_D$	Dipolar Coupling	Hz ~ kHz
$\hat{H}_J$	Scalar Coupling	Hz ~ kHz
$\hat{H}_Q$	Quadrupolar Coupling	kHz ~ MHz

The Zeeman effect ($\hat{H}_z$) defines the nuclear resonance frequency. The

chemical shift ($\hat{H}_{CS}$) reflects how nuclei are affected by their local environments due to the chemical shielding. The mathematical description of $\hat{H}_{CS}$ is shown in equation 1.9 and contains isotropic and anisotropic parts.

$$\hat{H}_{CS} = -\gamma B_0 \hat{I}_z[\sigma_{iso} + \frac{1}{2}\sigma_{aniso}(3\cos^2\theta - 1)] \qquad \text{Equation 1.9}$$

where $\hat{I}_z$ is the z component of the nuclear spin angular momentum operator $\hat{I}$. σ_{iso} is the isotropic chemical shielding factor, and σ_{aniso} is the anisotropic chemical shielding factor dictates the magnitude of the chemical shift anisotropy (CSA). The angle θ is the angle that the long axis of the CSA ellipsoid makes with the static field.[3] The term $(3\cos^2\theta - 1)$ in this equation clearly indicates that the chemical shift interaction $\hat{H}_{CS}$ is orientation-dependent. The CSA arises from non-spherical electron distributions around the nuclei and the random orientations of these non-spherical electronic environments relative to the magnetic field B_0 in solid samples. The induced magnetic field $B_{induced}$ is thus orientation-dependent. For molecules with the same electronic environments, but varied orientations relative to B_0, $B_{induced}$ has different values, leading to a spread of resonance frequencies. This reflects in the spectra is the emergence of broadened peaks, as shown in the static ^{13}C NMR spectrum of glycine whose carbonyl signals show a typical CSA pattern covering a range of more than 120 ppm (Figure 1.3).

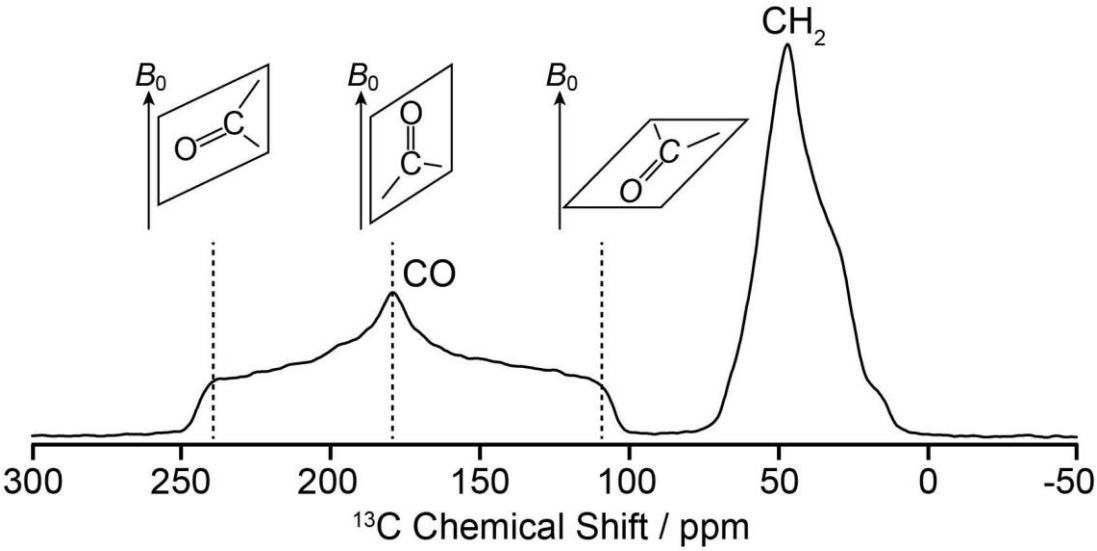

Figure 1.3 Static ^{13}C cross polarization (CP) NMR spectrum of glycine. Depiction of the orientation of carbonyl groups and their corresponding resonances[3] in the NMR spectrum. Spectrum was recorded at 9.4 T on a Bruker Avance III HD solid-state NMR spectrometer.

The nuclear dipolar coupling ($\hat{H}_D$) comes from direct interactions among the nuclear magnetic moments of nuclear spins. When placed in an external magnetic field, the nuclear magnetic moment will produce a small magnetic field which will affect the actual magnetic field felt by its adjacent nuclei. This will broaden the resonance frequencies of those adjacent nuclei. The dipolar coupling is transferred through space and its magnitude depends on the internuclear distance. A more detailed description of the dipolar coupling Hamiltonian is showed in the following equations including the one for heteronuclear dipolar coupling (equation 1.10) and the one for homonuclear dipolar coupling (equation 1.11):[3]

$$\hat{H}_D^{\text{hetero}} = -d(3\cos^2\theta - 1)\hat{I}_z\hat{S}_z \qquad \text{Equation 1.10}$$

where $\hat{I}_z$ and $\hat{S}_z$ are the z components of the nuclear spin angular momentum

operators $\hat{I}$ and $\hat{S}$, respectively, while *d* is the dipolar coupling constant. The angle θ refers to the orientation of the internuclear vector with respect to the orientation of the external magnetic field.

$$\hat{H}_D^{homo} = -\ d \cdot \frac{1}{2}(3\cos^2\theta - 1)\,[3\hat{I}_{1z}\hat{I}_{2z} - (\hat{I}_1 \cdot \hat{I}_2)] \qquad \text{Equation 1.11}$$

where $\hat{I}_{1z}$ and $\hat{I}_{2z}$ are the z components of the nuclear spin angular momentum operators $\hat{I}_1$ and $\hat{I}_2$, respectively.

The dipolar coupling constant *d* (unit in "Hz") is further defined as:

$$d = \frac{\mu_0}{8\pi^2}\frac{\hbar\gamma_I\gamma_S}{r_{IS}^3} \qquad \text{Equation 1.12}$$

where r_{IS} is the internuclear distance between *I* and *S* spins, γ_I and γ_S correspond to the gyromagnetic ratios of *I* and *S* spins, respectively, $\hbar$ is the reduced Planck's constant, and μ_0 is the vacuum permeability. The coupled *I* and *S* spins can be the same or different with *d* corresponding to homonuclear or heteronuclear dipolar coupling constant. The term $(3\cos^2\theta - 1)$ in equation 1.10 and 1.11 also indicates that the $\hat{H}_D$ interaction is orientation-dependent. The dipolar coupling strength *d*, as shown in equation 1.12, is proportional to the product of the gyromagnetic ratios while it is inversely proportional to the cube of the internuclear distance.[3]

The scalar coupling (also called *J* coupling) interaction is an indirect spin-spin coupling interaction. This interaction is mediated by the electrons around the nuclei. Therefore, scalar coupling only exists amongst nuclei connected by shared electrons, *i.e.*, nuclei that are bonded. Unlike dipolar coupling, the scalar coupling is not orientation-dependent.[2]

For nuclear spins with $I > ½$, the distribution of their electrical charge is non-spherical, and there is electric quadrupole moment for these nuclei. Their

quadrupole moment will interact strongly with the electric field gradient generated by the surrounding electron clouds. This interaction with an order of magnitude of MHz is quadrupolar coupling $\hat{H}_Q$. $\hat{H}_Q$ is orientation-dependent and since it has large magnitude it is far more difficult to resolve in the solid-state NMR spectra.[2,3]

1.1.3 Magic Angle Spinning (MAS)

In section 1.1.2, we discussed spin interactions in NMR spectroscopy, especially anisotropic interactions. These anisotropic interactions can significantly broaden the signals and are detrimental to the resolution of solid-state NMR spectra. The mathematic description of many orientation-dependent first order interactions contains the term $(3\cos^2\theta - 1)$. This means that the effects of these anisotropic interactions will be zero if $(3\cos^2\theta - 1)$ is equal to 0 corresponding to θ being 54.74° (the magic angle θ_m). A visual description of θ_m is that it's the angle between a cube's space diagonal and any of its three connecting edges. By rapidly spinning the sample about an axis inclined at 54.74°with respect to the static magnetic field (as shown in Figure 1.4), the anisotropic interactions $\hat{H}_{CSaniso}$, $\hat{H}_D$, and part of $\hat{H}_Q$ can be removed, whilst isotropic interactions $\hat{H}_Z$, $\hat{H}_{CSiso}$ and $\hat{H}_J$ are unaffected by spinning, yielding much narrower peaks than under static experimental conditions (as shown in Figure 1.5). This technique is known as MAS.[3,4]

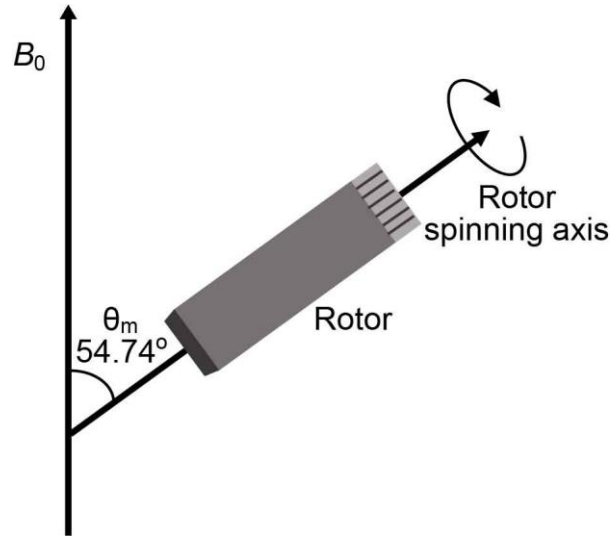

Figure 1.4 Schematic representation of a rotor spinning at the magic angle θ_m = 54.74° with respect to the external magnetic field B_0.

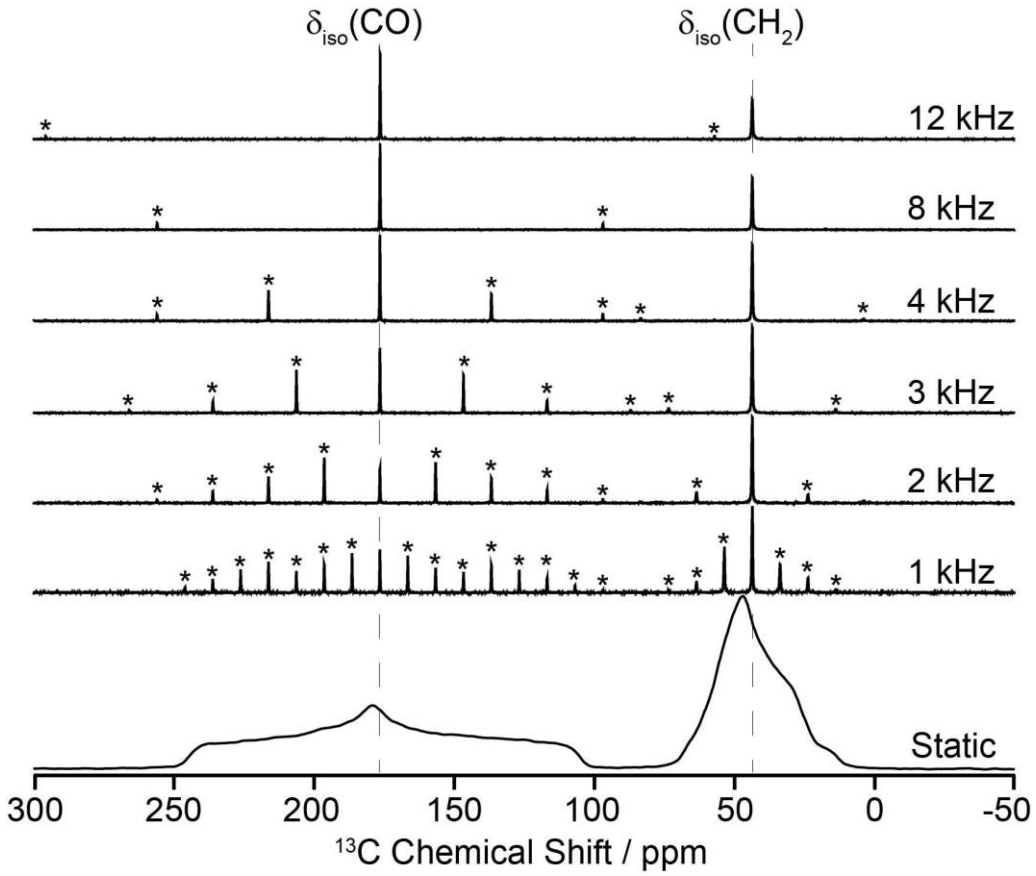

Figure 1.5 ^{13}C CP NMR spectra of glycine at different MAS rates. Asterisks (*) denote spinning sidebands. Spectra were recorded at 9.4 T on a Bruker Avance III HD solid-state NMR spectrometer.

The anisotropic interactions will not be averaged out completely by MAS when the spinning rate does not exceed the magnitude of these interactions. The residual interactions will yield peaks appearing at frequencies of $\delta_{iso} \pm n\nu_{MAS}$ on both sides of the isotropic peak, known as spinning sidebands as shown in Figure 1.5. In most cases these sidebands are often unfavorable, as they may cover and hide some signals and complicate the analysis of spectra. However, some additional information about the sample under study may be extracted from them.[3]

1.1.4 Basic 1D NMR experiments

1.1.4.1 One pulse *vs* CP

The one pulse experiment is perhaps the most fundamental experiment in NMR while the CP[5] technique is much the routine solid-state NMR experiment for low-γ nuclei such as ^{13}C and ^{15}N. In one pulse NMR experiments (sequence shown in Figure 1.6(a)), a rf pulse (typical a 90° pulse) is applied directly to the nuclear spins of interest and rotates the bulk magnetization away from its equilibrium position along the z-axis (direction of the external magnetic filed B_0) towards the xy-plane. The precession of the magnetization vector in the xy-plane induces current in the coil aligned in the xy-plane and surrounding the sample. This current is recorded as the free induction decay (FID) signal which is then Fourier transformed into the familiar NMR spectrum.[1] Since one pulse experiments detect the polarization of nuclear spins directly, the signal intensities can be used to quantify the corresponding nuclei if enough delay is applied for the spins to relax to the ground states for the next cycle of acquisition. For low-γ nuclei such as ^{13}C

and ^{15}N, their one pulse experiments often suffer from drawbacks of low spin polarization and typically low isotopic abundance, thus signal intensities are often quite low.

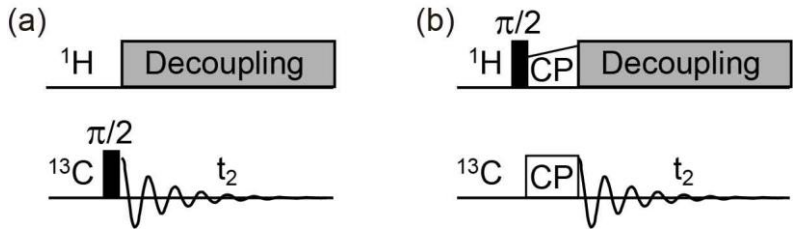

Figure 1.6 (a) One pulse and (b) CP sequences.

To enhance the NMR signals of low-*γ* nuclei, nowadays many solid-state NMR experiments routinely use the CP technique (Figure 1.6(b)) which takes advantage of transferring the polarization from abundant and highly polarized nuclei (usually ^{1}H) to the target nuclei. The polarization transfer occurs by applying continuous rf fields simultaneously on both the more sensitive nuclei and the nuclei of lower polarization. The theoretically maximum enhancement is γ_I/γ_S (*I* and *S* correspond to the highly polarized spins and low sensitive spins, respectively). For ^{1}H to ^{13}C CP, the theoretical enhancement in ^{13}C signal intensity is about 4 times. Figure 1.7 shows a ^{13}C CP signal improvement by a factor of about 10. This additional improvement benefits from the rapid relaxation rate of the ^{1}H spins which enables enough spins to recover back to the ground states within short delays for the next acquisition cycle.

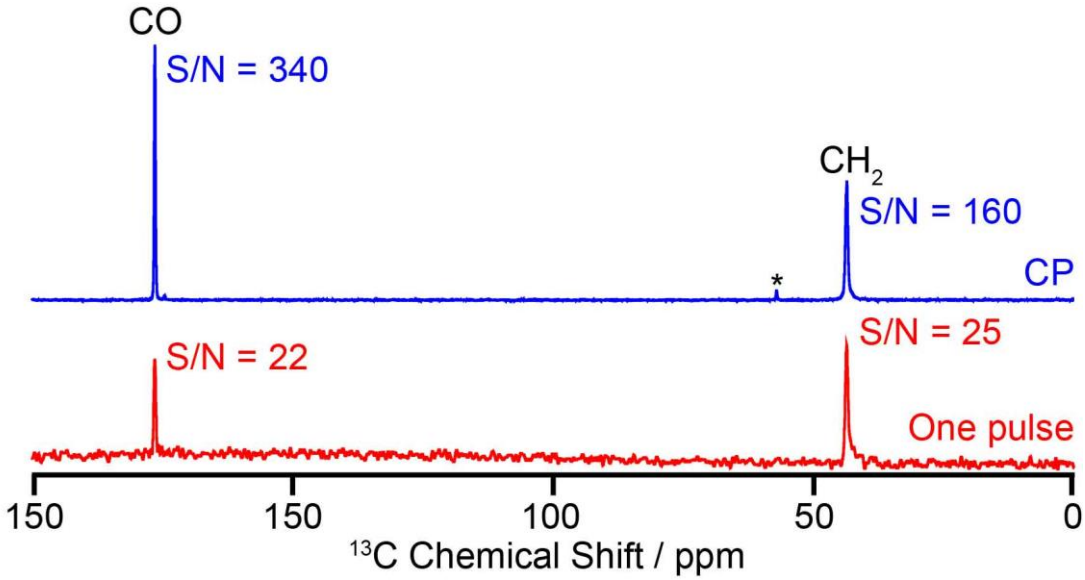

Figure 1.7 ^{13}C CP and one pulse NMR spectra of glycine. Both spectra were recorded with the same number of scans accumulated and recycle delay between scans. S/N refers to signal-to-noise ratio. Asterisks (*) denote spinning sidebands. Spectra were recorded at 9.4 T on a Bruker Avance III HD solid-state NMR spectrometer.

1.1.4.2 Dipolar decoupling

As it is discussed in section 1.1.3 the effects of anisotropic interactions such as dipolar couplings cannot be completely eliminated by MAS if their strength is much stronger than the spinning rate. For instance, the dipolar coupling strength between directly bonded ^{1}H-^{13}C is about 22 kHz.[6] The commonly used MAS rate of 12 kHz is not enough to average out this strong dipolar coupling interaction. The residual ^{1}H-^{13}C dipolar coupling will broaden and weaken the signals of the involved C nuclei, as the broad and weak signal of CH_2 group shown in Figure 1.8 (spectrum in black). Further elimination of the dipolar coupling interactions can be reached by manipulating the ^{1}H spins. This can be achieved by applying rf pulses on ^{1}H spins to keep their continuous

transitions between the two spin states, averaging out their interactions to the coupled ^{13}C spins.[3] The most original decoupling technique is the use of a continuous high-power rf irradiation on the ^{1}H spins, while more efficient decoupling sequences such as TPPM[7] and SPINAL64[8] are available nowadays. Their significant contribution to the spectra resolution an intensities is clearly demonstrated in Figure 1.8. The combination of those dipolar decoupling techniques with MAS and CP leads to the modern high-resolution solid-state NMR spectroscopy.

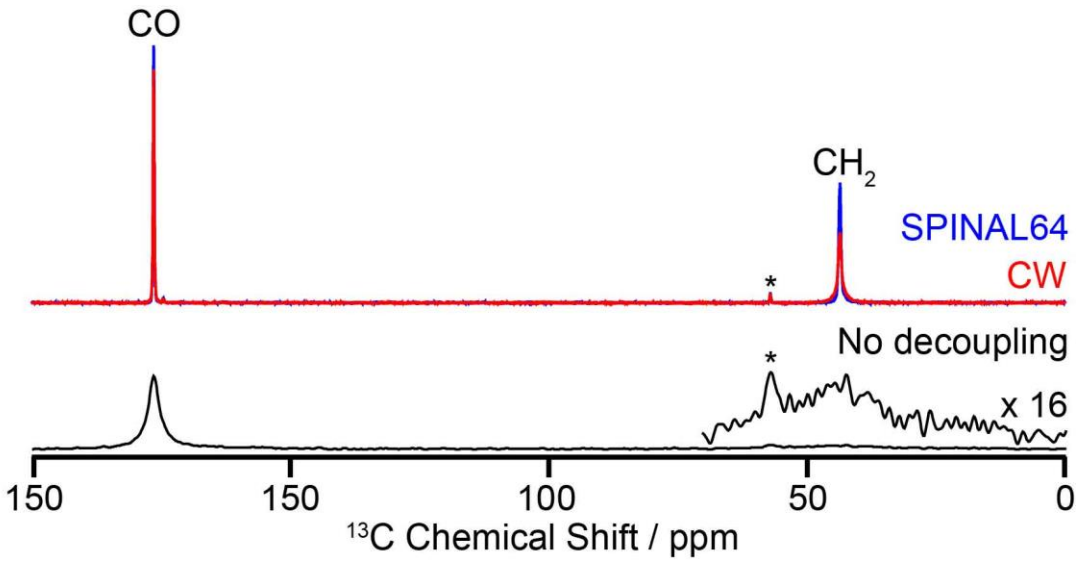

Figure 1.8 ^{13}C CP NMR spectra of glycine without ^{1}H decoupling (black), with SPINAL64 (blue) and continuous-wave (CW) ^{1}H decoupling during signal acquisition. Spectra were recorded at 9.4 T on a Bruker Avance III HD solid-state NMR spectrometer.

1.1.5 Multidimensional and multinuclear NMR experiments

Although in 1D solid-state NMR spectroscopy, CSA, dipolar coupling, *J* coupling and quadrupolar coupling are often unfavourable. Because these interactions will significantly broaden the lineshapes of NMR signals,

decreasing spectral resolution and complicating the interpretation of NMR signals. However, on the other hand, these interactions contain much additional structural or dynamics information about the sample. CSA and quadrupolar coupling are sensitive probes for the symmetry of the local electronic structure, while dipolar and *J* couplings are very suitable probes to indicate nuclear connections. These interactions are bases for many multidimensional and multinuclear NMR methods which aim at revealing connections between nuclei and structures or dynamics of the studied samples.[9]

A general scheme for two-dimensional (2D) NMR spectroscopy is shown in Figure 1.9. The experiments start with a preparation period during which the samples are excited by some pulses such as a 90° pulse or a CP sequence, the resulting magnetization is then allowed to evolve under certain spin interactions for a time t_1. Following the t_1 time, a mixing period consisting of further pulses is used to prepare the magnetization for final detection. After Fourier transformation, signals detected during t_2 period are just like normal 1D spectra. By recording the spectra at increasing times t_1, the acquired spectra will show specific modulation based on the spin interactions chose to evolve during the t_1 period. Further transforming the modulated spectra in the t_1 dimension will produce a 2D spectrum showing correlations between nuclei that are connected by spin interactions.[1,2]

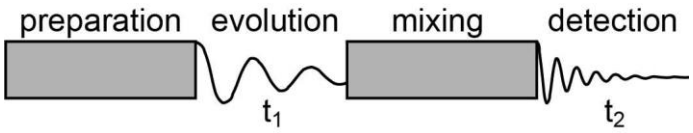

Figure 1.9 A general scheme for 2D NMR experiments.

1.1.5.1 Dipolar and *J* coupling based multidimensional and multinuclear NMR experiments for structural determination

Multidimensional and multinuclear NMR methods on the basis of dipolar and *J* coupling are perhaps the most commonly used NMR approaches to determine nuclear proximities and bonding connections. Under MAS condition, most dipolar coupling interactions will be averaged to zero by spinning. Therefore, special dipolar recoupling sequences are often required for experiments utilizing dipolar coupling. Since *J* coupling is not affected by MAS, no recoupling sequences are needed.[3,9]

Since *J* coupling only exists between bonded nuclei, the *J* coupling based multidimensional experiments give only bonding correlations and therefore yield molecular structures much directly. The correlations given by the dipolar coupling based NMR experiments are not limited to bonded nuclei as dipolar coupling transfers through space and also exists amongst non-bonded nuclei. Figure 1.10(d) and 1.11(c) show the ^{13}C-^{13}C Incredible Natural Abundance DoublE QUAntum Transfer Experiment (INADEQUATE)[10,11] and $^{13}C\{^{15}N\}$ *J*-coupling based heteronuclear multiple quantum correlation (*J*-HMQC)[12] spectra of a solid sample of ^{13}C and ^{15}N fully labelled L-histidine. Both experiments rely on *J* coupling. It is clear that only through-bond ^{13}C-^{13}C and ^{13}C-^{15}N correlations (coded in blue) have been obtained from these 2D spectra. In the dipolar coupling based ^{13}C-^{13}C proton driven spin diffusion (PDSD) dipolar assisted rotational resonance (DARR)[13,14] experiment (Figure 1.10(e)) and $^{13}C\{^{15}N\}$ dipolar coupling based HMQC (*D*-HMQC)[15] experiment (Figure 1.11(d)), non-bonded ^{13}C-^{13}C and ^{13}C-^{15}N pairs even those of several bonds away also display correlations (coded in red). Clearly structural information

from the *J* coupling based experiments are more direct and unambiguous while those from experiments utilizing dipolar coupling are more abundant. These techniques can be used simultaneously to provide complementary information about the systems under study.

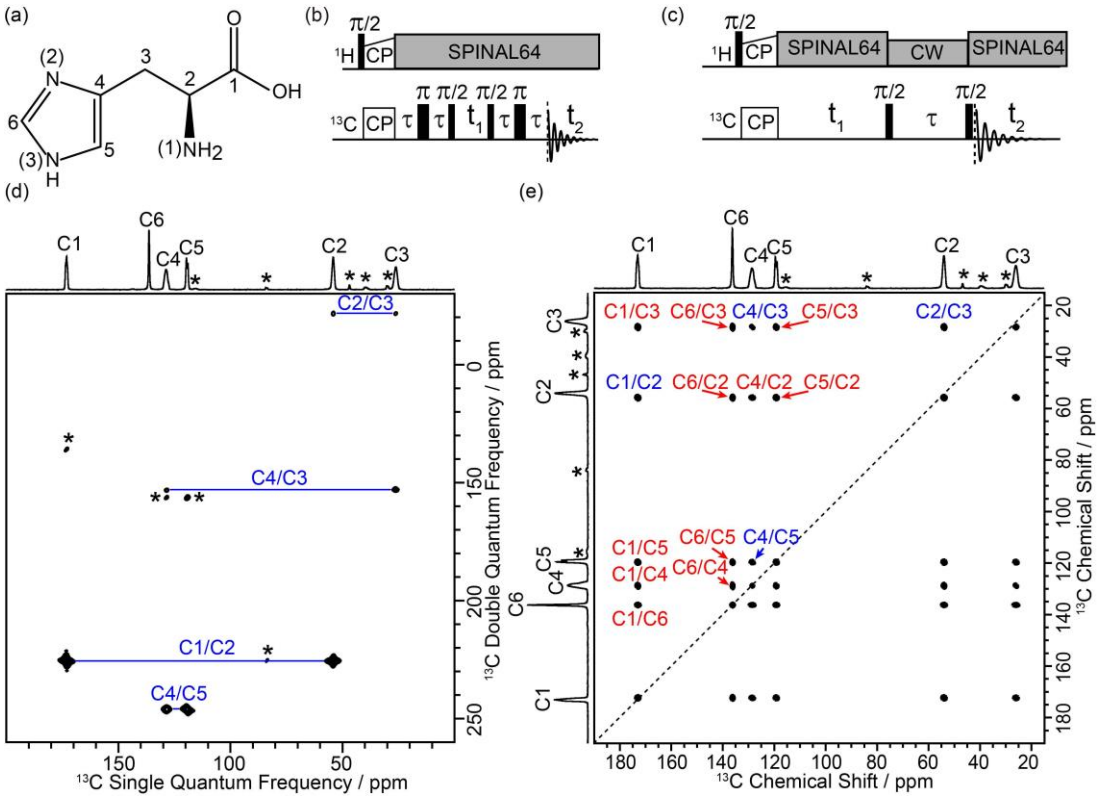

Figure 1.10 (a) Molecular structure of ^{13}C and ^{15}N fully labelled L-histidine. (b) ^{13}C-^{13}C refocused INADEQUATE sequence[10,11] and (c) ^{13}C-^{13}C PDSD DARR sequence.[13,14] (d) ^{13}C-^{13}C 2D refocused INADEQUATE spectrum and (e) ^{13}C-^{13}C 2D PDSD DARR spectrum of ^{13}C and ^{15}N fully labelled L-histidine. Asterisks (*) denote spinning sidebands. Spectra were recorded at 9.4 T on a Bruker Avance III HD solid-state NMR spectrometer.

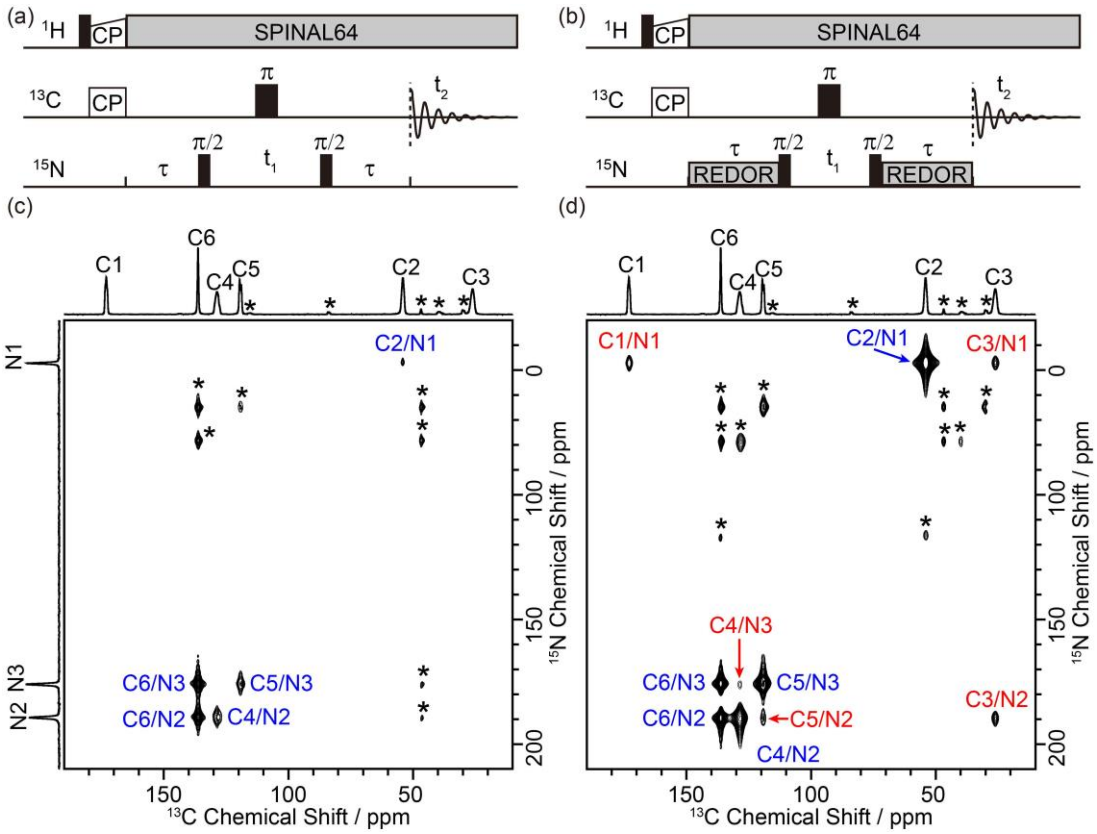

Figure 1.11 (a) $^{13}C\{^{15}N\}$ *J*-HMQC sequence[12] and (b) *D*-HMQC (incorporated with rotational echo double resonance (REDOR) for dipolar recoupling) sequences.[15] (c) $^{13}C\{^{15}N\}$ *J*-HMQC and (d) *D*-HMQC spectra of ^{13}C and ^{15}N fully labelled L-histidine. Asterisks (*) denote spinning sidebands. Spectra were recorded at 9.4 T on a Bruker Avance III HD solid-state NMR spectrometer.

1.1.5.2 Measurement of dipolar coupling strength

The dependence of dipolar coupling interaction on internuclear distance offers great opportunities to quantify internuclear proximity. These are very important quantitative information to determine the local structures. A general way to measure the dipolar coupling strength is to record the NMR signals from nuclei of interest while their dipolar coupling interaction with other nuclei is selectively re-introduced under MAS by some recoupling sequences. The

introduction of dipolar coupling interactions will cause an observable phenomenon, that is, signals from nuclei suffering from dipolar coupling will be weakened. The degree of signal reduction depends on both the dipolar coupling strength and the interaction duration. It can be seen in Figure 1.12 that those ^{13}C (C2, C4, C5, C6) bonded with ^{15}N show significant reduction in signal intensity while those not directly bonded with ^{15}N are rarely affected. The influences of dipolar coupling on ^{13}C signals increase with increasing recoupling time, as shown by Figure 1.12(c) and (d). The degree of signal reduction is the result we measure in the experiments while the recoupling time is the parameter we can manipulate. The dipolar coupling strength can thus be obtained by simulating the experimental curves of signal reduction *vs* recoupling time. The internuclear distance is then calculated according to equation 1.12.

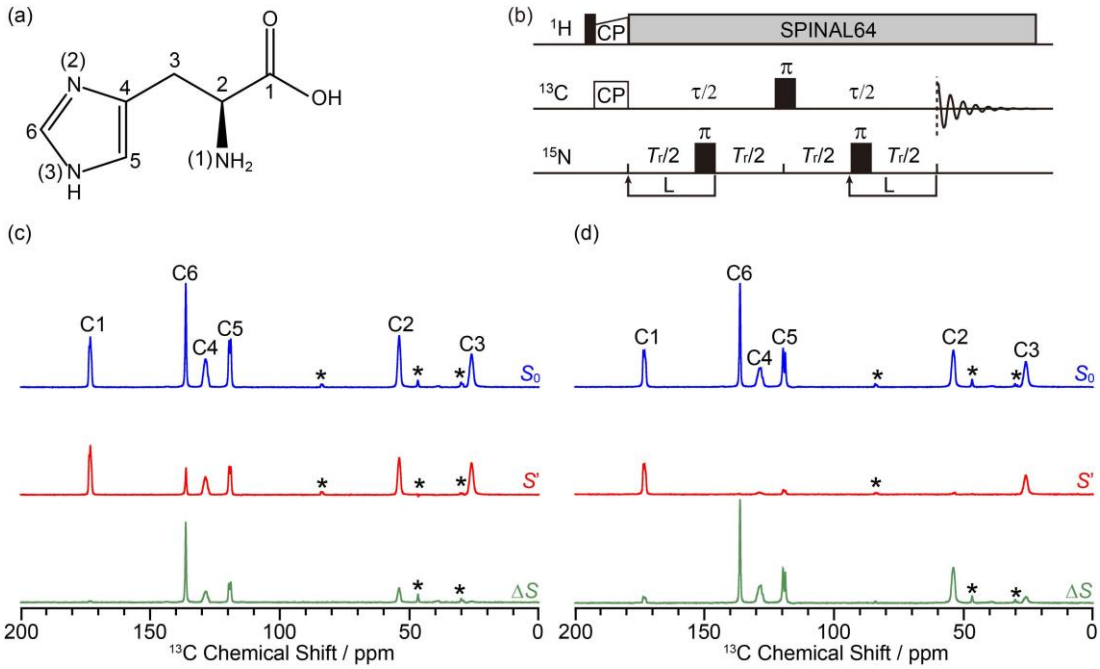

Figure 1.12 (a) Molecular structure of ^{13}C and ^{15}N fully labelled L-histidine. (b) $^{13}C\{^{15}N\}$ REDOR sequences.[16] $^{13}C\{^{15}N\}$ REDOR spectra at recoupling time of 0.7 ms (c) and 2 ms (d). S_0 and S' corresponding to ^{13}C spectra without the introduction of dipolar couplings and with, respectively. ΔS is the difference spectrum between S_0 and S'. Spectra were recorded at 9.4 T on a Bruker Avance III HD solid-state NMR spectrometer.

Solid-state NMR, especially multidimensional and multinuclear NMR experiments are very informative. However, the intrinsically low sensitivity of NMR spectroscopy poses fundamental challenges for its applications. Spin polarization in NMR is intrinsically weak and many NMR active nuclei have low natural abundance *e.g.*, ^{29}Si (4.67%), ^{13}C (1.11%). It means that for a natural abundance sample, there are only 4.67% components contributing to ^{29}Si NMR signals and 1.11% components contributing to ^{13}C NMR signals. This makes one-dimensional NMR experiments on such natural abundance samples time-consuming, let alone more complex multidimensional NMR

experiments. To address this challenge, isotope enrichment can be applied. However, isotope enrichment is difficult and poses great challenges for sample synthesis. In addition, many isotope enriched reactants are usually quite expensive, which makes this technique uneconomical and non-universal.

Fortunately, a newly accessible strategy for increasing the polarization of nuclear spins, DNP,[17–20] provides a promising way to enhance weak NMR signals.

1.2 DNP enhanced solid-state NMR

1.2.1 Development of DNP

DNP is a technique that can enhance the sensitivity of solid-state NMR signals by several orders of magnitude by taking advantage of transferring the large polarization of electrons to nearby nuclei via microwave (μw) irradiation. The DNP effect was first predicted in 1953 by Overhauser who theoretically proposed the possibilities of polarizing the nuclei in metals by irradiating the conduction electrons with microwave at the electron resonance frequency.[21] In the same year this theory was experimentally confirmed by Slichter on lithium metal.[22,23] Despite the great potential of DNP for producing large nuclear spin polarization, the development of DNP for practical applications was not straightforward. For several decades, this technique remained dormant due to the lack of a suitable technology to continuously produce high power and compatibly high frequency microwave for high-field NMR spectrometers. In the very initial exploration of DNP NMR experiments, the magnetic field was limited to < 3.5 T.[19,24] The breakthrough was made in the early 1990s by Griffin and his co-workers who successfully combined the

advanced high power gyrotron technology which can continuously generate microwave at frequencies higher than 140 GHz with high-field solid-state NMR (> 5 T).[17,25,26] Together with the development of low-temperature MAS probes that can operate at temperature of 100 K or even lower, and improved polarizing radicals, high-field DNP solid-state NMR has been well developed, and commercial instruments are available nowadays.[17–20,24,27,28] High-field MAS DNP NMR was initially used to characterize biomolecules.[19] However, the availability of commercial DNP NMR spectrometers since 2009 has spurred a rapid development of their application to characterizing a much broader range of materials.

1.2.2 Theoretical enhancement of DNP

The DNP enhancement is determined by the relative sizes of spin polarization of electrons to that of nuclei. As shown in the equation 1.1 and 1.2, spins with higher gyromagnetic ratios (γ) have larger energy gaps between spin states, resulting in larger spin polarization. Thus, the theoretical DNP enhancement is based on the relative value of the gyromagnetic ratios of spins, which is $\varepsilon = \gamma_e/\gamma_n$. For ^{1}H and ^{13}C, $\gamma_e/\gamma_{1H} \approx 660$, $\gamma_e/\gamma_{13C} \approx 2640$, it means that the potential enhancements of DNP on ^{1}H and ^{13}C NMR signals are 660, 2460, respectively, which translates to time savings of $(660)^2 = 435600$ and $(2640)^2 = 6969600$, respectively.

1.2.3 Transfer of polarization in DNP

1.2.3.1 Transfer of polarization from electrons to nearby nuclei

In DNP NMR experiments, there must be paramagnetic centers carrying unpaired electrons in the studied samples. These paramagnetic centers can

be intrinsic to the sample, such as those free electrons in the metal or some paramagnetic metal ions. Nevertheless, most materials under study are intrinsically free of paramagnetic centers. It is necessary to introduce paramagnetic centers to the samples, and the most commonly introduced paramagnetic agents are stable radicals containing unpaired electrons. The direct polarization transfer from those electrons to the nearby nuclei at magnetic field higher than 5 T involves three main mechanisms: the solid effect, the cross effect and the Overhauser effect.[19,24]

The solid effect mechanism can be understood using a two-spin system involving one electron and one nucleus that are coupled with each other. By irradiating the coupled spin system with microwaves at frequencies of $\nu_e \pm \nu_n$, where ν_e and ν_n represent the Larmor frequency of the unpaired electron and the nucleus, respectively, the forbidden zero-quantum and double-quantum transitions are stimulated. These transitions will lead to either positive (double-quantum) or negative (zero-quantum) enhancements of the nuclear polarization which is much larger than the nuclear polarization stimulated by irradiating the nuclei alone with the rf wave of much lower energy at frequency of ν_n. The solid effect dominates when the EPR line width of polarizing agents is much narrower than the nuclear Larmor frequency ν_n. Radicals with symmetrical molecular structures such as 1,3-bisdi-phenylene-2-phenylallyl (BDPA), or paramagnetic metal ions such as Mn(II) and Cr(III) satisfy this condition and exhibit mainly solid effect. It should be noted that the efficiency of the solid effect decreases rapidly with increasing magnetic field strength, which limits the popularity of this effect for polarization transfer at high field.[19]

Similar to the solid effect, the Overhauser effect is also based on a two-

spin system involving coupled electron and nucleus, and relies on the presence of zero-quantum and double-quantum relaxation pathways.[29] However, unlike the solid effect, in the Overhauser effect the microwave irradiation is near the single quantum transition at frequency of ν_e. In the subsequent relaxation processes, to generate nuclear polarization the relaxation rates of the zero-quantum and double-quantum relaxation pathways must be different. One advantage of the Overhauser effect is that its efficiency increases with increasing magnetic field, and it has been shown promising for high-field DNP with up to 80 times enhancement at 18.8 T.[30]

The cross effect perhaps is the most efficient and popular polarization transfer mechanism. It involves a three-spin system including two unpaired electrons coupled via *J*-exchange or dipolar interactions and a coupled nucleus. To generate the cross effect, the two coupled electrons must have different Larmor frequencies with their difference equal to the Larmor frequency of the nucleus, as shown in equation 1.13. In this case, the central energy levels are degenerate (as shown in Figure 1.13(a)), and the polarization transfer from the electrons to nuclei is maximized. When the system is irradiated with microwave of frequencies of ν_{e1} and ν_{e2}, the stimulated transitions between energy levels with different nuclear spin states lead to enhanced nuclear polarization, either positive or negative, as indicated by the solid arrowed lines in Figure 1.13(b) and (c).[19]

$$|\nu_{e1} - \nu_{e2}| = \nu_n \qquad \text{Equation 1.13}$$

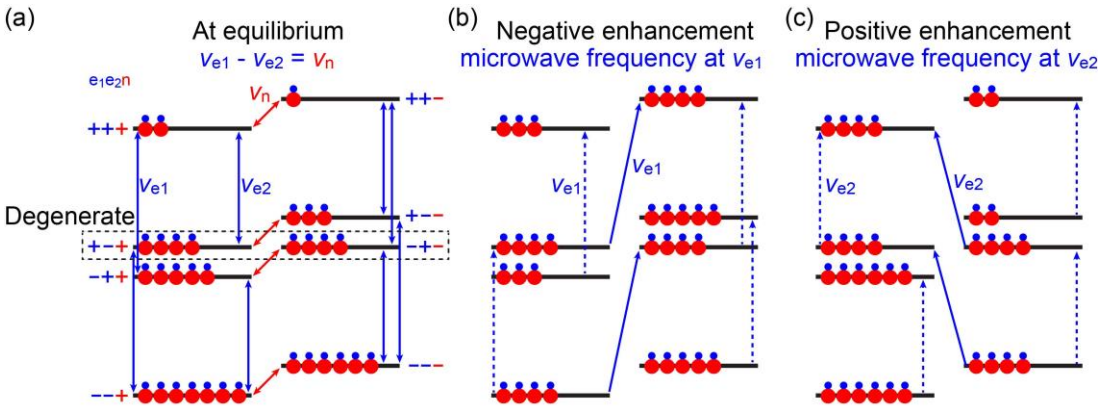

Figure 1.13 Energy diagram illustrating the cross effect in DNP. (a) Nuclear spin polarization at equilibrium, (b) negative nuclear spin polarization by irradiating the first EPR frequency ν_{e1} and (c) positive nuclear spin polarization by irradiating the second EPR frequency ν_{e2}. The red and blue balls represent nuclei and electrons, respectively.

The initial high-field DNP experiments utilizing the cross effect were performed with the monoradical TEMPO.[17,19] In this case, the condition of frequency matching (equation 1.13) is fulfilled only for those radicals that present the proper relative orientation of their g-tensors. To improve the fraction of radicals matching this condition and improve the efficiency of cross effect, Griffin *et al*. in 2006 pioneered introducing the nitroxide biradical to high-field MAS DNP.[31] The first biradical that was used was TOTAPOL which consists of two TEMPO moieties tethered by organic chain and showed large enhancements. However, the organic chain in TOTAPOL is relatively flexible, and the two TEMPO moieties are not constrained to the desired relative orientation to fulfill the frequency matching conditions for the cross effect mechanism. A rigid tether was used later, which produced bTbk biradical.[32] In bTbk the two TEMPO rings are approximately perpendicular to each other, which conformation is constrained by the rigid tether. This favorable orientation

largely increases the cross effect efficiency, and bTbk generally showed larger enhancements than TOTAPOL under identical experimental conditions.[32] Beyond the geometry, it was found that the electronic relaxation properties of radicals are another key factor that decide the radicals' DNP enhancements.[33,34] Radicals with longer electron spin-lattice relaxation time T_{1e} enable more effective saturation of the electron resonance and offer more efficient polarization transfer from electrons of these radicals to nearby nuclei. The radicals' T_{1e} can be increased by increasing radicals' molecular weight, in another word, making the radicals bulkier. It was shown that bCTbk, the bulky derivative of bTbk, has a T_{1e} value that is about twice as long as that of bTbk, and showed 2.5 to 4 times larger enhancements than bTbk.[33] Based on the idea of tethering two monoradicals and increasing radicals' T_{1e}, many efficient biradicals have been synthesized such as AMUPol,[35] TEKPol[34], etc., which have been commercially available and are routinely used in many DNP facilities.

1.2.3.2 Spin diffusion

Only nuclei in proximity to the unpaired electrons, typically within a few nanometers, can get polarized directly based on the three polarization transfer mechanisms described in the above section. In most cases the target nuclei are often remote from the radicals, especially those bulk materials or porous materials with small pores excluding the radicals from the interior. In these cases, the polarization can still be relayed via spin diffusion which can transfer the enhanced polarization of nuclei in proximity to the radicals to the remote nuclei.[36,37] The spin diffusion process is based on homonuclear dipolar interactions, and is therefore between identical nuclei. The distance (d) of spin

diffusion can be described as:[38]

$$d = \sqrt{DT_1} \qquad \text{Equation 1.14}$$

where D is the spin diffusion coefficient which is dependent on the strength of homonuclear dipolar coupling, and T_1 is the nuclear longitudinal relaxation time. According to equation 1.14, it is clear that spin diffusion distance increases with stronger homonuclear dipolar coupling interactions and slower nuclear longitudinal relaxation. The strong ^{1}H-^{1}H homonuclear dipolar coupling and the almost 100% natural abundance of ^{1}H makes ^{1}H-^{1}H spin diffusion a vital part in DNP NMR experiments. For organic material, the ^{1}H-^{1}H spin diffusion distance can reach from 10 nm to 1 μm at 100 K, as well as the range of polarization transfer.[36]

For samples that are intrinsically abundant in ^{1}H such as organic crystals, their ^{1}H provide the matrices for ^{1}H-^{1}H spin diffusion. While for materials lacking ^{1}H, the matrices can be set up by the ^{1}H of solvents introduced along with the radicals.

1.2.3.3 Transfer of polarization to low-γ nuclei

For low-γ nuclei, the polarization of electrons can transfer to them directly, which is called direct DNP. In the direct DNP, nuclei in proximity to the radicals get polarized. Since many low-γ nuclei are with low natural abundance, spin diffusion is hindered. Therefore, for materials that are not dissolved in the radical solutions, generally only the signals from surfaces that can reach by radicals can get enhanced. Nevertheless, if the studied materials have been properly isotope enriched, spin diffusion will recover and can transfer the polarization to the material interior, which has been shown in ^{29}Si DNP

experiments on ^{29}Si enriched silica nanoparticles[39] and ^{17}O DNP experiments on ^{17}O enriched ceria nanoparticles.[40] In practice, direct DNP often requires complicated adjustments to the spectrometer parameters once the observed nuclei are switched. Therefore, direct DNP is normally not favourable in practice. Another more commonly used way for polarization transfer to the target low-γ nuclei is the indirect DNP in which polarization transfer is mediated by ^{1}H: electron → ^{1}H → low-γ nuclei. This method takes advantages of the easy to meet matching conditions for electron → ^{1}H polarization transfer, the efficient ^{1}H-^{1}H spin diffusion and the generally used cross polarization transfer technique for low-γ nuclei. In practice, indirect DNP often yields more sensitivity enhancements than direct DNP. The indirect DNP also simplifies optimization of the experimental parameters, as the spectrometer only needs to be adjusted to yield the best ^{1}H enhancements regardless of the observed nuclei.

1.2.4 DNP in practical use

1.2.4.1 DNP NMR spectrometer

The MAS DNP NMR spectrometer is commercially available from Bruker BioSpin company.[28] The microwave source is a gyrotron that generates high frequency microwave irradiation by cyclotron resonances of electrons in a dedicated magnetic field. The microwave frequency needed is proportional to the strength of the corresponding NMR magnetic field. For 9.4 T NMR spectrometer, the corresponding frequency of the microwave is at 263 GHz. The microwaves from the gyrotron are transmitted to the probe through a corrugated waveguide and applied on the samples in the probe. The probes

are low-temperature ones and usually operate at a temperature of 100 K or even lower. The reason for operating DNP at low temperature is that both polarization transfer from electrons to nuclei and spin diffusion are more efficient at lower temperature, leading to better enhancements.[24] The most commonly used probes are 3.2 mm probes whose maximum spinning rate can reach 15 kHz at 100 K, while probes for smaller rotors such as 1.3 mm probes are available recently and reach MAS frequencies up to 40 kHz. Compared with conventional NMR magnets, the one used in the DNP system is equipped with an additional superconducting sweep coil that can tune the magnetic field where the sample locates and match the condition for best DNP efficiency.[24]

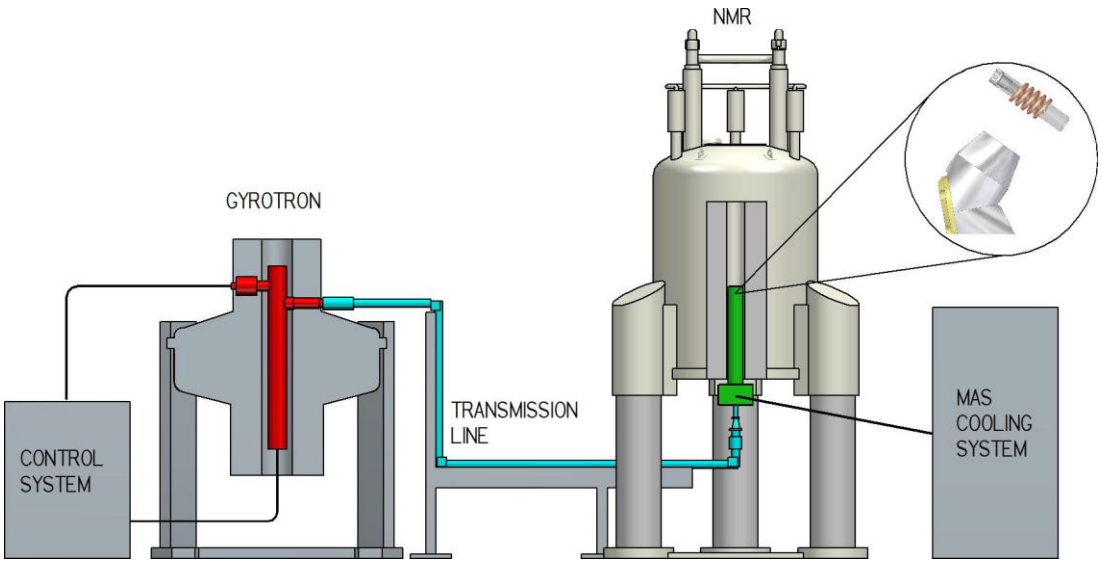

Figure 1.14 Schematics of a commercial solid-state DNP NMR system. The left parts are the gyrotron (microwave source) and its control system with the gyrotron tube shown in red. The right parts are NMR spectrometer equipped with a low-temperature NMR probe (green) and a MAS cooling system. The gyrotron is connected with the NMR spectrometer by the microwave transmission line (cyan). Figure is reproduced with permission from[41].

1.2.4.2 Pulse programs used for DNP.

The pulse programs for DNP NMR experiments are basically the same as those used in conventional NMR experiments. The only significant difference is the additional electron channel for microwave irradiation for DNP NMR (as shown in Figure 1.15 with a typical CP sequence for DNP). A pre-saturation sequence is often added in DNP NMR. This sequence allows nuclear magnetization to be saturated prior the recycle delay, and ensures the magnetization relaxing to the same status prior next scan, which can reduce variations between scans.

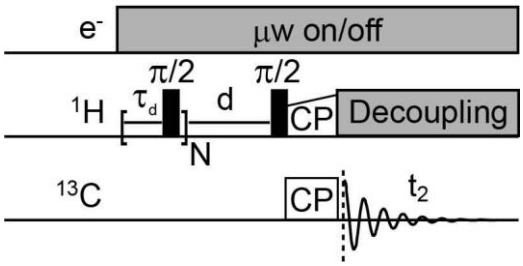

Figure 1.15 Pre-saturated CP pulse sequence for DNP experiments. w is the recycle delay which is equal to 1.3 × τ_{DNP}(^{1}H). N = 100 is the number of ^{1}H saturation pulses with 1 ms delay τ_d between pulses.

1.2.4.3 Commonly used radical polarizing agents and solvents.

Currently, the most commonly employed radicals for MAS DNP NMR experiments are nitroxide biradicals, as shown in Figure 1.16 with some commonly used ones. Those nitroxide biradicals are derived from the monoradical TEMPO and are designed to match the cross effect better. The first nitroxide biradical for high field DNP was developed by Griffin *et al.* and is TOTAPOL[31] which is a water soluble radical. For the study of water sensitive

materials such as dehydrated alumina or zeolites, non-aqueous solvents are required, as well as radicals that can dissolve in these solvents. The first such nitroxide biradical is bTbk which is soluble in many organic solvents especially those halogenated ones.[33,42]

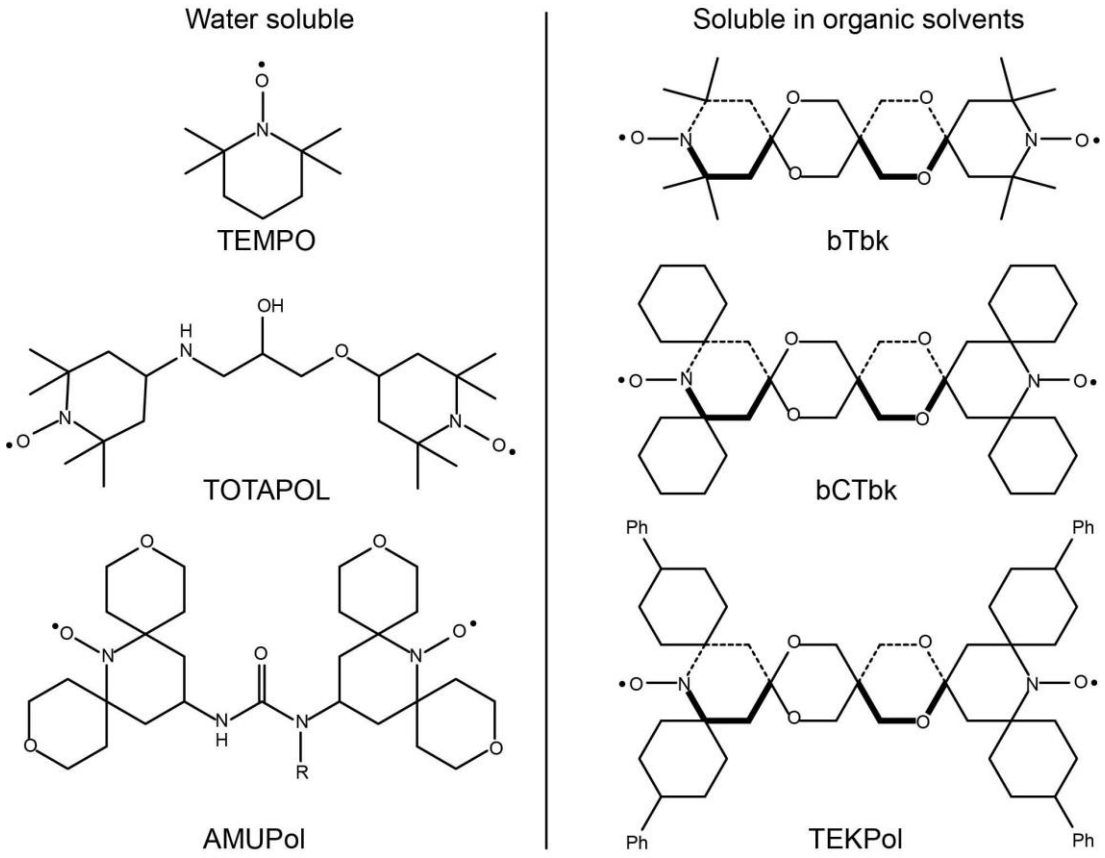

Figure 1.16 Structures of some commonly used water soluble and organic solvents soluble radicals for MAS DNP NMR experiments.

The choice of solvents is also a key factor that can influence DNP performances. In practice, the solvents should be glass-forming. This is because crystallization of the solvents will exclude both radicals and samples, decreasing DNP enhancements, therefore, solvent crystallization should be avoided.[24] For aqueous solvents, the addition of glycerol or DMSO can form glass matrices at low temperature, and water/glycerol and water/dimethyl

sulfoxide (DMSO) mixtures are commonly used for water soluble radicals. For radicals that can dissolve in organic solvents such as bTbk and TEKPol, 1,1,2,2-Tetrachloroethane (TCE) was shown as an ideal choice for optimal DNP enhancement and has been the most widely used organic solvent.[42] The high performance of TCE solvent comes from its reliable glass forming and appropriate ^{1}H concentration. The optimal concentration for these biradicals were suggested to be 10-20 mM.[20,43] Low concentration may lead to an insufficient number of radicals generating polarization in the samples. High concentration of radicals will dramatically broaden NMR lineshapes and reduce signal intensity by paramagnetic effects,[43,44] but more importantly reduce the nuclear T_1 and therefore the DNP buildup time, which will lead to lower enhancement factors.[36]

1.2.4.4 Sample preparation for DNP

Most materials studied by DNP NMR are absent of paramagnetic centers and therefore require the introduction of exogenous radicals and the corresponding solvents used to dissolve the radicals. In previous DNP studies of biomolecules or organic species, it is quite typical that the samples were uniformly dispersed in the radical solutions or swollen in the solutions if they are soluble.[19] For samples that are insoluble in the radical solutions, such as inorganic framework materials, incipient wetness impregnation is the most commonly used technique to prepare the DNP samples. This technique is first introduced to high field DNP experiments by Emsley *et al*. for studying mesoporous silica.[18,20] In this technique, the amount of radical solution is just enough to uniformly wet the surface of materials or fill the pores of porous materials, reaching a well balance between excessive paramagnetic effects

caused by an excess of radicals and insufficient radicals for polarization transfer. Another advantage of incipient wetness impregnation is that it minimizes the addition of radical solution, therefore maximizes the effective volume of the studied samples. All of these advantages of incipient wetness impregnation help to yield an optimal overall DNP efficiency, making this technique very popular in nowadays DNP experiments.

1.2.5 DNP in heterogeneous catalysis research

DNP NMR has been successfully applied to the characterization of a broad range of materials, including biomolecules, organic polymers, inorganic materials, hybrid materials, etc.[19,20,24,27,45] The significant sensitivity improvement provided by DNP enables detecting insensitive nuclei in these materials, such as ^{13}C, ^{15}N,[46] ^{17}O,[47] ^{119}Sn,[37,48], ^{89}Y[49,50] etc., whose detection by conventional NMR is challenging due to their low gyromagnetic ratio or low natural abundance. Notably, many multidimensional and multinuclear NMR experiments can be performed, providing more in-depth knowledge about structures or dynamics of these materials. This section will focus on the application of DNP to heterogeneous catalysis research.

Due to the unique sensitivity of NMR to the local electronic environment, NMR has long been a vital analytical method for structural characterization and fundamental investigation of catalytic processes at atomic precision. Nevertheless, the catalytic sites of heterogeneous catalysts are often located on the surface and typically account for a small fraction of the whole catalysts, while the reactive reaction intermediates along the reaction processes usually exist with low concentration. These characteristics of the catalytic systems sometimes pose significant challenges for NMR studies. Fortunately, the

development of modern high field MAS DNP significantly reduces the sensitivity limits of NMR and opens new opportunities for structural and dynamic studies of heterogeneous catalysis systems.

Many of early research of modern high field DNP using homemade instruments predominantly focused on biomaterials or organic species. It was until 2009 when commercialized DNP spectrometers were available[28] that the application of DNP has been extended to a much broader range of materials, including inorganic and hybrid materials of which many are important heterogeneous catalysts.[24,27,34,45] Therefore, almost all the publications relating to high field DNP NMR experiments on heterogeneous catalysis systems have appeared in the last decade.[24]

1.2.5.1 Structural characterization of heterogenous catalysts

A series of inorganic and hybrid materials have been studied by DNP, including silica,[18,39,47,51,52] alumina,[53–57] silica–alumina,[58–60] zeolites[37,48,61] and metal-organic frame works (MOFs).[62,63] These materials can either function as catalysts themselves or can be used as supports loaded with functionalized organometallic moieties and metal nanoparticles. The catalytic sites of these materials are often located on the surface. Of importance to the catalytic properties are the distribution, the local structures of the active sites and the interactions between them, which are often challenging to be characterized due to their non-periodic, disordered and typically low concentration characteristics. DNP, especially the so-called DNP surface enhanced NMR spectroscopy (DNP-SENS) technique developed by Emsley *et al* has shown great potential in addressing these challenges.[18,20]

For silica materials, those of catalytic interests are mesoporous or

nanoparticles presenting large surface area. The first silica material studied by DNP-SENS is mesoporous silica with its surface functionalized with phenol and imidazolium units.[18] An enhancement of at least 50-fold (using 25 mM TOTAPOL in D_2O/H_2O 90:10 at 9.4 T) was obtained and enabled recording ^{13}C signals from the functionalized surface species of natural abundance within one hour (see Figure 1.17), which would otherwise take at least 70 days without DNP. An enhancement of 21-fold was later obtained on the ^{29}Si signals of the same kind of material, and enabled the determination of the incorporation patterns of functional groups on silica surfaces in a few minutes, as shown in Figure 1.18.[51] By further combining with selective isotope enrichment on both organic moieties and silica surface sites, ^{13}C-^{15}N, ^{13}C-^{29}Si, ^{15}N-^{29}Si multidimensional and multinuclear NMR experiments were able to perform within hours, enabling obtaining multiple structural constraints and elucidation of the three-dimensional structure of the surface sites.[64]

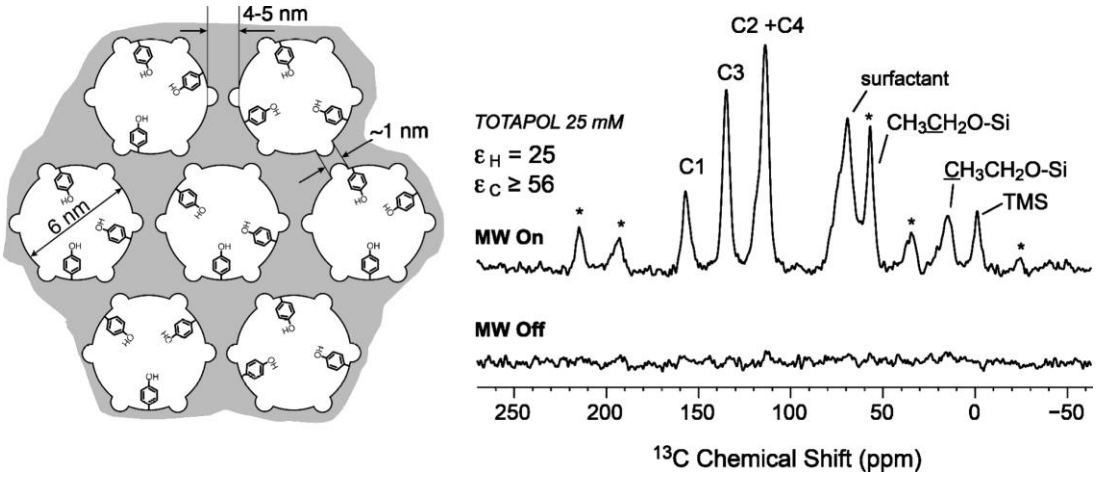

Figure 1.17 Mesoporous silica grafted with phenol groups and the corresponding ^{13}C CP MAS DNP NMR spectra with μw irradiation and without. Figure adapted with permission from[18]. Copyright 2010 American Chemical Society.

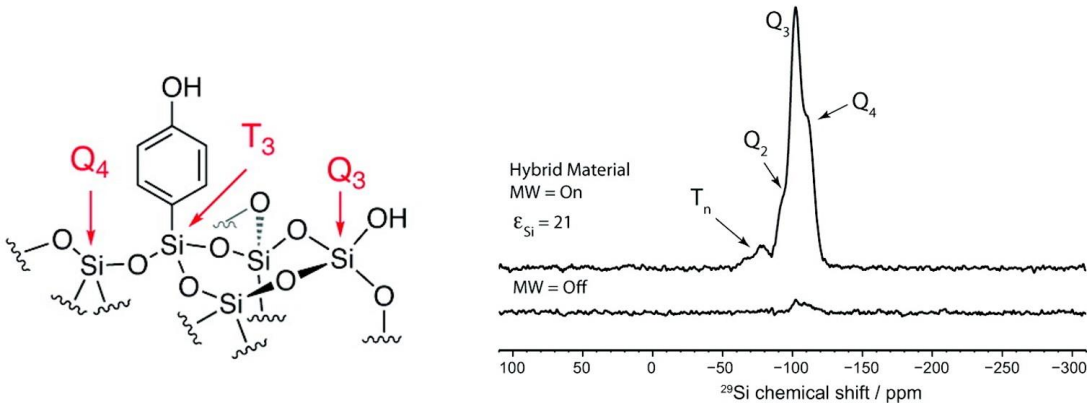

Figure 1.18 Local binding structures of phenol groups grafted on mesoporous silica and the corresponding ^{29}Si CP MAS DNP NMR spectra with μw irradiation and without. Figure adapted with permission from[51]. Copyright 2011 American Chemical Society.

The properties of the non-modified silica are also of great interests, especially their surface silanol (Si-OH) groups and the dynamic motions of these silanol groups. Previously, the structures and dynamics of the surface properties of silica were mainly studied using ^{1}H and ^{29}Si NMR. Recently, with the help of DNP, these surface silanol species were investigated using ^{17}O NMR.[47,65] ^{17}O signals from different silanol species of natural abundant samples were observed within hours.[47] The great sensitivity enhancements also made it possible to acquire 2D ^{17}O{^{1}H} correlation experiments as well as accurately measure the ^{17}O-^{1}H distances at natural abundance.[65] These detailed information enabled identification of hydrogen-bonded and non-hydrogen-bonded silanol groups and determination of dynamic motions of these groups.

Due to the Brønsted and Lewis acid sites on the surface, alumina and silica–alumina are widely used both as catalysts and as catalyst supports for single catalytic sites or metal nanoparticles. Their surface acid properties have

been topics of great interest in NMR. The DNP surface-enhanced ^{27}Al NMR in combination with cross-polarization and MQ-MAS enabled the determination of local symmetries of ^{27}Al sites at alumina surface.[55] The previous challenging ^{27}Al-^{27}Al 2D dipolar correlation spectra could also be successfully recorded in only 4 h, revealing the presence of pentacoordinated Al and its role in bridging interfacial tetra- and hexacoordinated Al.[54] For silica–alumina, DNP enhanced 2D scalar and dipolar ^{29}Si–^{27}Al INEPT experiments allowed for an atomic level determination of the Interface between silica and alumina and structural insights into the nature of Brønsted acid sites.[58] Natural abundance ^{17}O DNP was also used to probe the surface acid sites on silica–alumina and accurately measure the O-H bond length of different surface hydroxyls with an unprecedented, sub-pm precision.[60]

Zeolites are another class of solid acid catalysts and porous materials. Most zeolites are microporous with pore diameter less than 1 nm which is smaller than most commonly used bulky biradicals.[66] The micropores exclude the radicals from entering the interior of zeolites. Hence, DNP experiments on zeolites are challenging, and there have been only a few DNP reports on zeolites published in recent years,[37,48,61] including the work reported in this thesis.[67] One of the first example of DNP in zeolites was to characterize the Sn sites in Sn-beta zeolite containing only 2 wt % of natural abundance Sn. The 2 orders enhancement allowed ^{119}Sn signals being recorded within hours, revealing tetrahedrally coordinated framework Sn sites in closed and open configurations, while without DNP, no ^{119}Sn signals were detected after 10 days experimental time.[37] The enhancements provided by DNP made high throughput analysis possible. ^{119}Sn spectra of Sn-beta with Sn-loadings

varying between 0 and 10 wt% and prepared via different synthetic protocols were obtained within hours. The rich structural information provided by NMR data in combination with the corresponding catalytic activity tests on these materials led to the identification of catalytic active sites of octahedrally coordinated Sn^{IV} involving the tetrahedral Sn-sites and two water molecules, while without DNP, no ^{119}Sn signals could be observed.[48] In earlier research, the enhancements were evaluated on ^{1}H signals which may not reflect DNP enhancements on zeolites well.[37,48] ^{29}Si signals were later used as a more direct indicator to evaluate DNP performances on zeolites.[61] The micropores of these Sn-beta zeolites have a maximum diameter of 0.7 Å which allows diffusion of solvents to the pores and ensure polarization transfer to the interior sites via ^{1}H-^{1}H spin diffusion.[48] It should be pointed out that no clear correlation between zeolite particle size and DNP enhancement was found.[61]

1.2.5.2 Detection of reactive species

Determining the molecular structures of reaction intermediates is a vital step towards a deeper understanding of the reaction mechanisms but remains a key challenge. This challenge is associated with the generally low concentration of those reactive intermediates distributed on the surface of solid catalysts. DNP has demonstrated great potential to detect reactive intermediates. By combining isotope labeling and DNP-SENS, Copéret *et al.* successfully indentified the trigonal bipyramidal (TBP) isomer as cycloaddition intermediates in the alkene metathesis catalytic cycle.[52] The 112 fold sensitivity improvement allowed observation of major surface species within seconds which would take hours or even days without DNP. ^{13}C-^{13}C 2D NMR experiments were performed within hours and directly determined the bond

connectivity and the carbon–carbon bond distances of the intermediate structure, as shown in Figure 1.19.

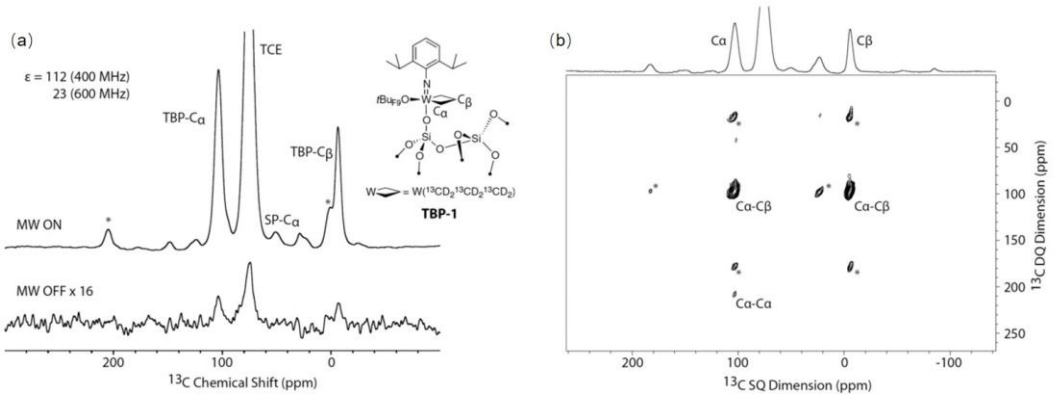

Figure 1.19 (a) ^{13}C DNP-SENS CP MAS spectra of tungsten TBP metallacycle. (b) 2D DNP-SENS refocused INADEQUATE of TBP. Figure adapted with permission from[52].

Since DNP exepriments need to introduce radical solutions to the samples under study, the chemical compatibility between radical, solvents and the rective species is a major issue that should be considered first when applying DNP to the detection of reactive species. As there are many aqueous and organic solvents available nowadays, choosing an appropriate one compatible with the studied samples is not hard. It is possible that some highly reactive intermediates *e.g.* cationic species could have secondary reaction with the radical polarization agents, which will not only quench the radicals and lead to no enhancement but will also alter the intermediates.[68] The are several ways to avoid the possible interactions between radicals and surface species.[66,68,69] All these methods are based on a simple principle, that is, separating the radicals from the species under study. It was shown that incorporating carbosilane dendrimers containing SiC_4 linkages at all the branching points[70] into the radicals to form much bulkier dendritic polarizing agents could

separate the paramagnetic centres from the surface species.[68] For reactive species on silica nanoparticles, their contact with the radicals could also be avoided by appropriately modifying the hydrophilicity of the silica support to facilitate aggregation of the nanoparticles. The aggregation of these particles occurs in non-polar solvents and allows the solvent to enter the interparticle space, but hinders the entry of the bulky radicals.[69] Confining the reactive species inside pores with pore windows smaller than the bulky radicals is also an effective way to avoid direct contact between radicals and reactive species. It was shown that MCM-41 with pore size of 2.5–3.0 nm could effectively block the TEKPol radical and protect the reactive organometallic surface species immobilized inside the pores.[66]

1.3 Carbocations in heterogeneous catalysis

1.3.1 Definition of carbocation

Carbocations are the positive ions of carbon compounds.[71] According to the number of coordination bonds of the charged carbon, the carbocations can be classified into two catagories which are carbenium ions and carbonium ions. The charged carbon in carbenium ions is trivalent and sp^2 hybridized. This kind of ions is considered as a classific form of carbocations, and the simpliest carbenium ion is methenium ion (CH_3^+). Carbonium ions are nonclassical carbocations with charged carbon being pentacoordinated, the simplist carbonium ion is methanium ion (CH_5^+). These classifications were proposed by George A. Olah and have been generally accepted and used.[71,72]

The carbocations are very reactive species and involved in many homogeneous and heterogeneous reactions as important reaction

intermediates.[71,73–81] The carbocations can form through protonation of the corresponding netural hydrocarbons, for instance, the protonation of alkenes generates carbenium ions while pronation of alkanes will give carbonium ions. The protonation undoubtedly needs strong acids, therefore, it is those acid-catalyzed electrophilic reactions or transformations such as elimination, cracking, isomerization, alkylation, etc. that involve carbocations as intermediates. The discovery of carbocations can be traced back to the 1900s, however, identification of carbocations as well as recognition of their roles as reaction intermediates are not straightforward.[71] Even the existence of carbocations as real intermediates had been doubted for decades, as in the early time carbocations could not be directly observed due to their reactive, unstable, transient (short-lived) and difficult to capture characteristics, and absence of modern characterization techniques at that time as well. It was until the 1960s when Olah *et al*., developed a univerial way to stablize carbocations in solution by using superacids that stable and long-lived carbocations were successfully prepared for thorough investigation. To test the obtained carbocation solution, Olah *et al*., successfully utilized the emerging spectroscopic techniques Infrared spectroscopy (IR) and NMR which provided direct and convincing evidence for the existence of carbocations.[71] The pioneering work of Olah *et al*., greatly catalyzed the renaissance of carbocation chemistry.

1.3.2 Carbocations in solution state

As mentioned in 1.3.1, carbocations were initially prepared in solution state using liquid superacids. Since carbocations are electron-deficient compounds and are strong electrophiles, their generation requires more

strongly electron-demanding electrophiles, while comparably weak nucleophilic counterions are needed to stabilize them. The superacids are acids with stronger acidity than that of 100% sulfuric acid.[82] Some commonly used superacids are CF_3SO_3H, FSO_3H, and conjugate acids such as FSO_3H-SbF_5 (Magic Acid),[83] HF-SbF_5, CF_3SO_3H-SbF_5, etc. The corresponding anions of these superacids such as BF_4^- have a very low nucleophilicity. These properties well match the conditions needed to generate and stabilize carbocations. The unitlization of superacids enables direct observation of very reactive carbocations, especially those alkyl cations such as *sec*-isopropyl and *tert*-butyl cations.[71]

Spectroscopic techniques such as NMR, IR, or ultra-violet–visible (UV-vis) spectroscopies play key roles in the investigation of carbocations.[71] A common feature of these analytical techniques is that they all are non-invasive, therefore, they are suitable to characterize the reactive carbocation intermediates, both in the solution and the solid states. In particular, NMR plays an important role in identifying carbocations due to the distinctively deshielded ^{13}C signals of positively charged carbon species. For instance, the ^{13}C chemical shifts of the charged carbons in *sec*-isopropyl and *tert*-butyl cations are about 320 ppm which is more than $\Delta\delta > 300$ ppm deshielded from that of their neutral counterparts.[71] Such significant differences facilitate distinctions of carbocations from any other compounds. Therefore, liquid-state NMR was used very early on to provide convincing evidences for the existence of long-lived carbocations in solution and determine their structures. Some carbocations identified by liquid-state NMR are shown in Figure 1.20 and show large ^{13}C chemical shifts for the charged carbons.

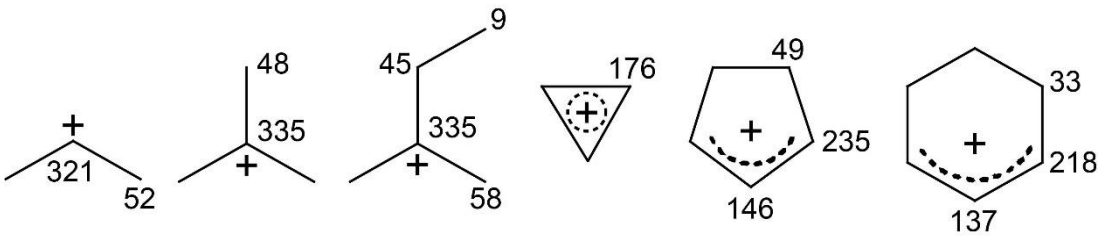

Figure 1.20 Some carbocation structures and the corresponding ^{13}C chemical shifts identified by liquid-state NMR.[84,85]

1.3.3 Carbocations in solid acid catalysts

1.3.3.1 Prediction of persistent carbocations in solid acid catalysts

Inorganic solid acids such as sulfated zirconia, alumina and zeolites are commonly used catalysts for hydrocarbon conversion especially those in oil refining and chemical industry. The carbocations can form from the corresponding hydrocarbon reagents through protonation by the acidic protons of the acid sites. Once formed, those reactive carbocation intermediates take part in a range of processes such as cracking, isomerization, alkylation, etc., which account for the conversion of hydrocarbons to a range of products.[71,74,77]

Whether a carbocation can persist in a solid acid can be predicted by comparing their acid strength.[75] The positively charged carbocations are also proton donors, and are therefore can be treated as a kind of acid. Haw *et al*., reported that the acid strength of zeolites is just below that of 80% sulfuric acid which is strong enough to stabilize some carbocations.[75] Figure 1.21 shows that alkyl cations have much stronger acid strength than zeolites, therefore, can not persist in zeolites. This is consistent with previous experimental observation[86] that the adsorption of propene on zeolite HY did not produce isopropyl cation, but it was alkyl-substituted cyclopentenyl cations that were

produced. These cations were formed from oligomerization of propene. The acid strength of cyclopentenyl cations is equivalent to ca. 35% sulfuric acid which is well below that of zeolites (as shown in Figure 1.21). Therefore, these cyclopentenyl cations can be stabilized by zeolites.[75] Haw *et al*., also proposed another index to predict whether a given carbocation would persist in zeolite, that is the proton affinity of the parent hydrocarbons of carbocations.[87] It was shown that the stabilization of a persistent carbocation in an unmodified zeolite normally requires the parent compounds have proton affinity more than 209 kcal·mol^{-1}.[87,88]

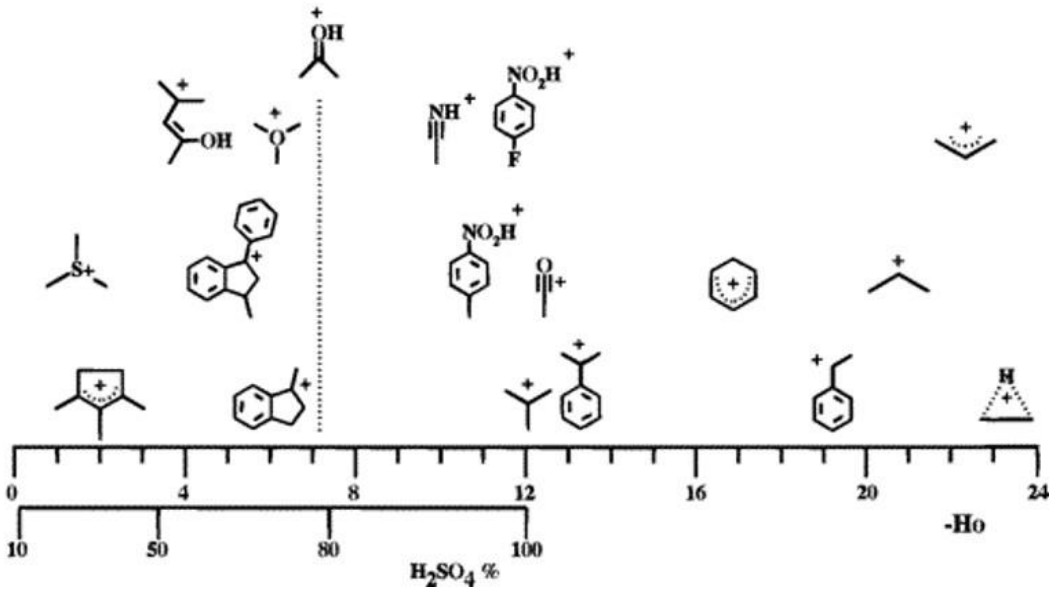

Figure 1.21 Acid strength of some carbocations. The dashed line corresponds to the limit of acid strength of Brønsted sites in zeolites. Figure adapted with permission from[75]. Copyright 1996 American Chemical Society.

1.3.3.2 Roles of carbocations in heterogeneous catalysis

Carbocations take part in a range of industrial reaction processes, particularly acid-catalyzed reactions. For example, the *tert*-butyl cation is proposed as an important intermediate in the butene-isobutene

isomerization,[89–91] and cyclic carbocations are suggested to involve in the hydrocarbon pool mechanism for the conversion of methanol to hydrocarbons (MTH).[81,88,92–96]

The MTH reactions are catalyzed by acidic microporous zeolites such as ZSM-5,[96,97] SAPO-34,[96,98] etc. The hydrocarbon pool (cyclic carbocations and neutral aromatic counterparts)[92] mechanism has been proposed for the formation of hydrocarbons from methanol, and suggests that the carbocations formed in situ and confined in the pores of the zeolites act as co-catalysts with the inorganic framework.[99] Two reaction pathways have been proposed, namely the side-chain and paring routes (as shown in Figure 1.22);[88,100,101] in the former, the olefins are released through the methylation of six-membered ring cations (alkylbenzenium cations) and the subsequent elimination of the side chain groups; the later route involves the participation of both six- and five-membered ring cations (alkylcyclopentenyl cations) with the olefins being produced via subsequent reactions relying on the expansion of the five-membered ring cations and contraction of the formed six-membered ring cations. For these carbocation involved reaction routes, the identification of carbocations is an important step needed to the understanding of the mechanism.

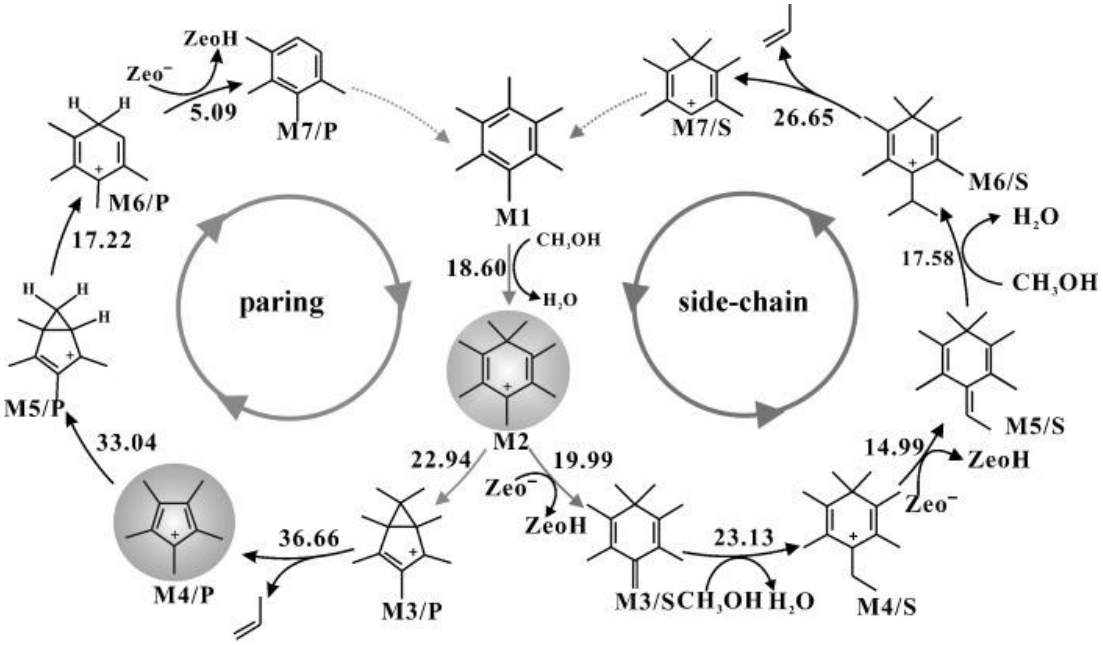

Figure 1.22 The paring and side-chain catalytic cycles for the MTH conversion. Numbers are calculated energy barriers given in kcal·mol^{-1}. Figure adapted with permission from[88].

1.3.3.3 Capturing carbocations in solid acid catalysts

To investigate the structures and roles of carbocations in heterogeneous reactions, it is essential to capture them in situ for further characterization. Haw *et al*., developed both batch-like and continuous-flow in situ devices and combined them with solid-state NMR spectroscopy[75,102] to capture and study the reactive carbocations (see Figure 1.23). In the batch-like device, parent hydrocarbons for producing carbocations are introduced to the solid catalysts which are loaded into NMR rotors surrounded by cryogenic liquid N_2. Then the samples are sealed and transferred to NMR detecting probes without warming. The probe temperature will be incrementally raised while NMR signals are detected. In this way, the formation and transformation of carbocations can be tracked in situ. The continuous-flow device is a pulse-quench reactor in which

the reagents are introduced continuously. After reacting at reaction temperature for a controlled time, the reaction is quenched by rapidly switching the reagent gas stream to cryogenically cooled N_2. In this way the temperature of the catalysts bed can therefore decrease very rapidly. It was shown that it only needed 170 ms for the catalyst being cooled by 150 K and less than 1 s to room temperature or lower.[102] Such rapid decrease in temperature can reduce the reactivity of the carbocation intermediates immediately, hindering their further transformation. As a consequence, those carbocations that are formed in situ are trapped and the samples are ready to study at ambient temperature. Since most heterogeneous reaction processes are under continuous conditions, and standard reaction conditions can be applied in the continuous-flow device, this in situ technique is a very good choice for the investigation of heterogeneous reaction mechanisms.

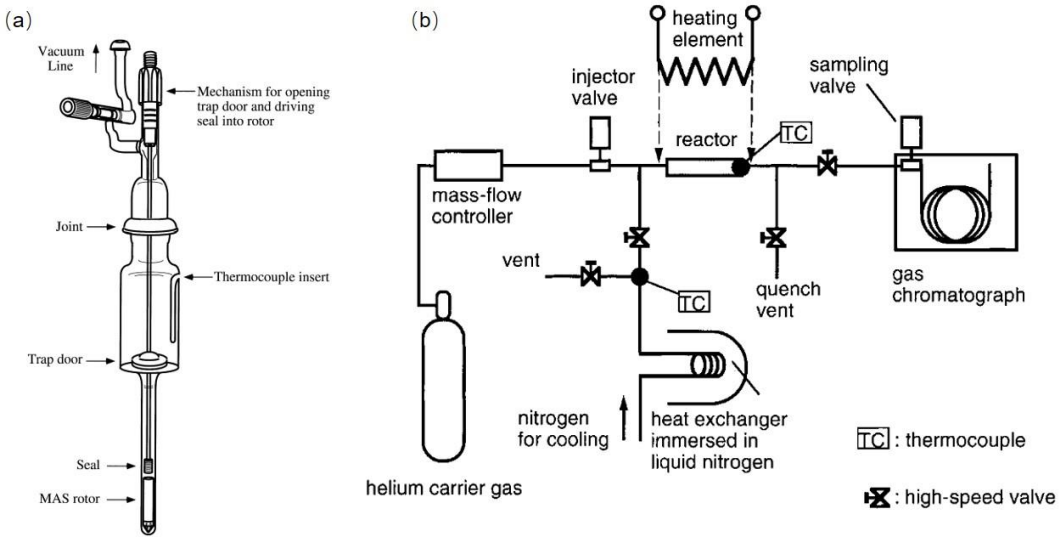

Figure 1.23 Batch-like (a) and continuous-flow (b) in situ solid-state NMR devices. Figures adapted with permission from[75,102]. Copyright 1996 American Chemical Society.

Although some reactive carbocations cannot persist in zeolites, they can

still be formed at reaction conditions normally including much higher temperature than room temperature, and act as intermediates. Capturing these cations simply by quenching them and the zeolite catalysts to low temperature is almost impossible, as they cannot be stabilized by zeolites alone at room temperature. Alternatively, these cations can be trapped using some nucleophilic molecules with lone electron pairs such as ammonia and acetonitrile.[89,91,103] These molecules can form stable onium ions with carbocations. The formed onium ions can then be characterized and reveal the molecular structures of the corresponding carbocations. This way, the existence of the *tert*-butyl cation in H-ZSM-5 zeolite has recently been experimentally identified.[89,91]

1.3.3.4 Structural identification of carbocations by solid-state NMR

Solid-state NMR, especially ^{13}C NMR, plays an important role in detecting reactive carbocations on solid catalysts. The rather distinct ^{13}C signals of carbocations are unquestionable to confirm the existence of carbocations via 1D ^{13}C spectra whose information alone however would not be enough to determine the detailed molecular structures of carbocations. In section 1.1.5, we demonstrated the great power of multidimensional and multinuclear NMR experiments for structural identification and host-guest interaction determination. Extending the use of these experiments to the study of carbocations is currently hindered by both the challenges associated with capturing enough highly reactive carbocations formed on solids and the intrinsically low sensitivity of ^{13}C NMR. Although ^{13}C isotopically enriched reagents are generally used to overcome this inherently poor sensitivity,[88,95,102,104] the small amount of carbocations that can be captured in

successful cases (typically 0.01 mmol·g^{-1} in the MTH activated β-zeolite[104]) usually only permits the acquisition of one dimensional ^{13}C NMR spectra.

Previously, the assignments of the ^{13}C solid-state NMR spectra of carbocations relied on indirect methods. Combination of 1D ^{13}C NMR spectra with gas chromatography-mass spectrometry (GC-MS) and density functional theory (DFT) calculations is commonly used to derive the structures of adsorbed carbocations.[88,95] Zeolites with carbocations formed inside the pores are quenched using in situ NMR techniques. The catalysts are then treated with HF solution which will dilute the zeolite framework and release the trapped organic species. These organic species are then extracted with CH_2Cl_2 from the HF solution and are ready for GC-MS experiments for structural characterization. It should be pointed out that during these treatments the carbocations will deprotonate to their neutral counterparts due to losing stabilization from zeolite framework. The species identified by GC-MS are therefore those neutral ones, not carbocations. The structures of those species are then used to set up the possible carbocation structures for DFT calculations which will predict the chemical shifts of these possible carbocations. Those carbocations that have ^{13}C chemical shifts matching well with the obtained 1D ^{13}C NMR spectra are then recognized as reactive intermediate species. Although these combinatorial methods are recognized as robust approaches for NMR spectral interpretation, they are still inaccurate for assignments due to the errors coming from the differences between the predicted models and the real molecular structures, and errors of DFT calculations on chemical shifts (typically around several ppm). In addition, the identified neutral carbon species are usually very complex, and not all of them

come from carbocations (as shown in Figure 1.24).[104] Therefore, this may lead to possible misinterpretation of the carbocations produced.

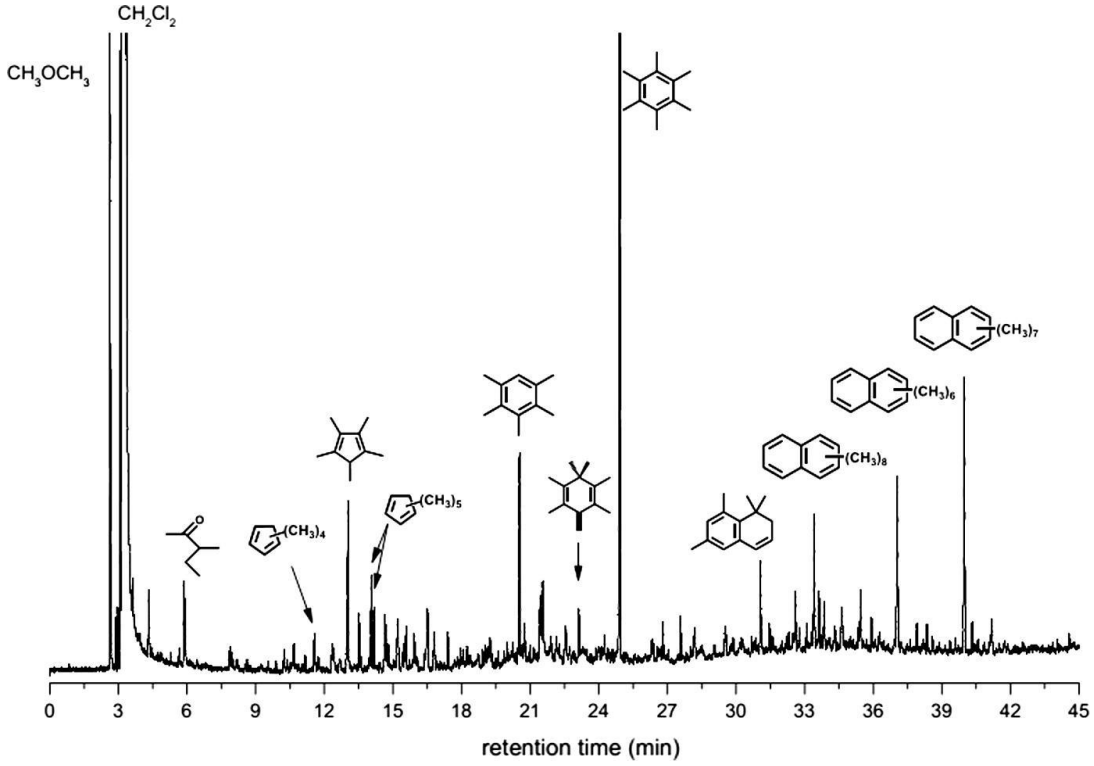

Figure 1.24 GC–MS chromatogram of the organic species retained in β-zeolite after MTH reaction. Figure adapted with permission from[104].

Additionally, the identification of the carbocations is indirectly obtained by separately digesting the deprotonated counterparts of the carbocations with concentrated sulfuric acid and analyzing the obtained solutions by liquid-state NMR which has much better resolution.[105] Using this way, a database of ^{13}C chemical shifts of possible cations is created and used to assign the solid-state ^{13}C NMR spectra. This procedure assumes that the states of the carbocations in the solutions are the same as those confined in the solid zeolite pores, which ignores the effects such as solvation on chemical shifts and is therefore not very accurate. Additionally, independent synthesis of the neutral species is required such as dienes for some cyclic carbocations, and therefore entails

prior knowledge of the possible structures.

Although the above indirect methods can give preliminary assignments of the solid-state ^{13}C NMR spectra, accurate determination of the carbocation structures is still very challenging and misinterpretation of the reaction intermediates as well as the corresponding mechanisms proposed based on these intermediates could happen. Figure 1.25 shows that carbocations sharing similar framework structures, five-membered cations with varied alkyl substitutes and different numbers and substituting positions of alkyl groups for instance, have very close chemicals shifts for their characteristic signals and the resolution of their 1D solid-state ^{13}C NMR spectra is definitely not enough to distinguish them from each other.[105] Therefore, multidimensional and multinuclear NMR experiments for more directly structural identification are needed for future research on the carbocations intermediates in heterogeneous catalysis.

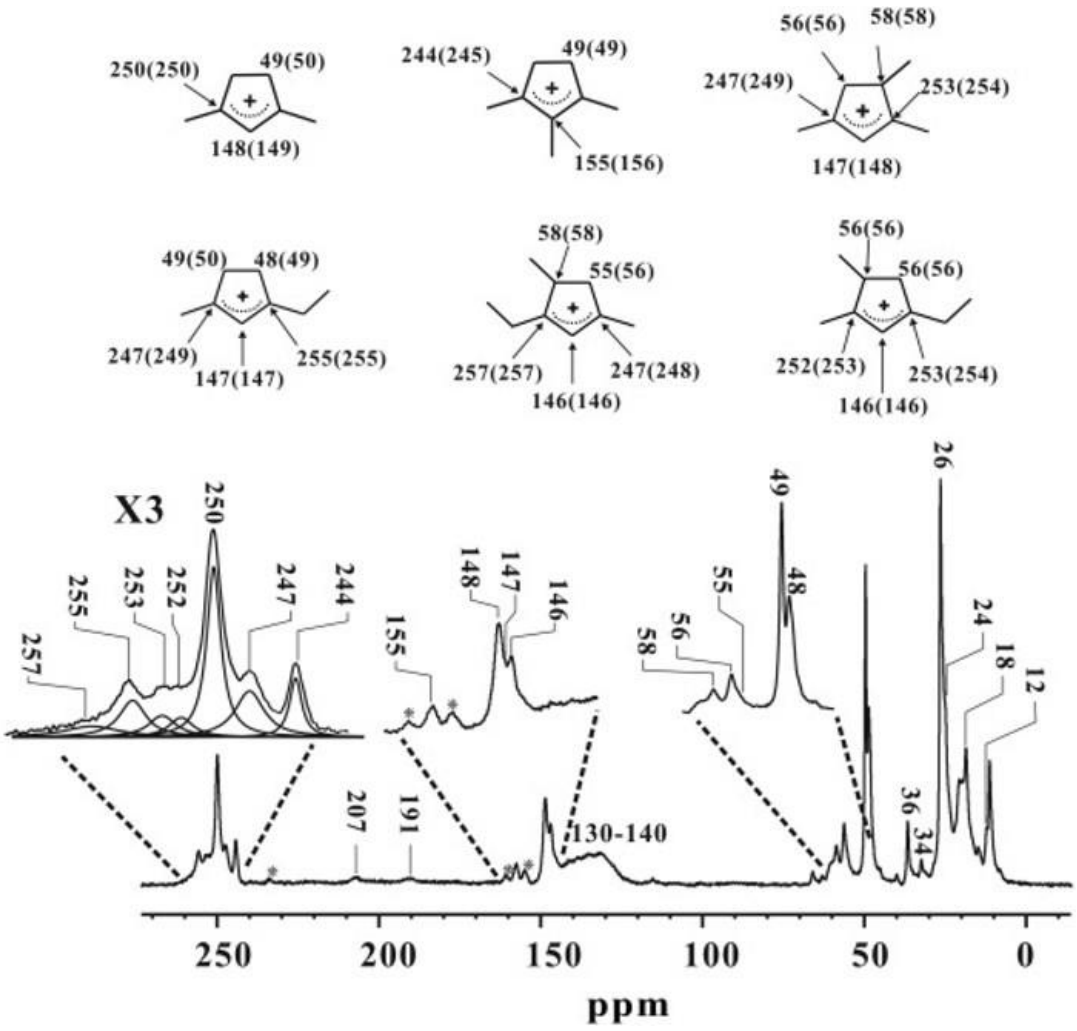

Figure 1.25 Solid-state ^{13}C MAS NMR spectrum (acquired at 18.8 T) of H-ZSM-5 after MTH reaction and the structures of some possible carbocations. Figure adapted with permission from[105].

1.4 Aims of this Project

This introduction is intended to give a brief background of the principles of solid-state NMR techniques, especially the application of multidimensional and multinuclear NMR methods for structural determination and investigation of host-guest interaction. The advanced DNP NMR technique for NMR sensitivity enhancement is also briefly introduced, including its application to heterogenous catalysis. This introduction also provides a brief description of

carbocation intermediates in heterogeneous catalysis. The stabilization of these carbocations in solid acid catalysts and techniques that are commonly used to capture and study these reactive cations are briefly introduced.

This introduction shows that the application of multidimensional and multinuclear NMR methods for the investigation of carbocation intermediates is challenging due to the intrinsically low sensitivity of NMR and difficulties associated with the high reactivity of carbocations. This PhD, therefore, is centered on demonstrating the great power of multidimensional and multinuclear NMR methods to determine the molecular structures of reactive carbocation intermediates with atomic precision. This work also aims to extend the application of DNP to heterogenous catalysis and combine it with those multidimensional and multinuclear NMR techniques to investigate those reactive carbocation intermediates.

Most previous solid-state NMR investigation on the reactive carbocation intermediates in MTH reaction proposed those ion structures via indirect methods that are typically based on a combination of 1D NMR spectra, GC-MS and DFT calculations, which may give misinterpretation of the possible carbocation structures. Chapter two and three aim at addressing the uncertainty of previous assignments of carbocations in zeolites by using a range of complimentary multinuclear and multidimensional NMR experiments. To address the challenges of utilizing multidimensional and multinuclear NMR methods to the investigation on reactive carbocations, which challenges are mainly associated with NMR's low sensitivity, this work of chapter four, therefore, also explores combining the DNP technique with those multidimensional and multinuclear NMR methods for more detailed studies on

carbocations.

The overall target of this thesis is to widen the application of multidimensional, multinuclear NMR methods and DNP to heterogeneous catalysis. Investigation of important carbocation intermediates, which is a vital topic in heterogeneous catalysis, is chosen to demonstrate the power of these NMR techniques and their great potential to become regular analytical tools in catalysis.

Chapter 2: Direct Structural Identification of Carbenium Ions and Investigation of Host-guest Interaction in the Methanol to Olefins Reaction Obtained by Multinuclear NMR Correlations

This chapter is adapted from a paper titled of the same name that was published in *Chemical Science* in 2017,[106] for which the authors contribution are as follow: D. X. prepared all the samples, conducted all NMR experiments with assistance from F. B. when required, made all the figures and wrote the initial draft of the manuscript which was enhanced with guidance from F. B.; all authors discussed the results.

2.1 Abstract

Probing and determining the intermediates formed during catalytic reactions in heterogeneous catalysis are strong challenges. Using ^{13}C labelling and two-dimensional ^{13}C-^{13}C through-bond NMR correlations, we directly reveal the structures of a range of carbenium ions species formed during the conversion of methanol to olefins on acidic H-ZSM-5 zeolite by mapping the carbon-carbon bond connectivities. Additionally, we use ^{13}C-^{27}Al and ^{29}Si-^{13}C through-space NMR experiments to probe the interactions between the confined carbon species (including carbenium ions) and the framework of the zeolite, which quantitatively provide an estimate for the carbon-aluminium and carbon-silicon distances, respectively.

2.2 Introduction

The MTO reaction is an important process for the production of light olefins (mainly ethylene and propene) from non-petrochemical

resources such as coal and natural gas.[96] The reaction is catalysed by microporous solid acids, in particular a wide range of zeolite (*e.g.* H-ZSM-5, H-SAPO-34), and has been successfully commercialised since the 1990's.[96–98] Nevertheless, there is a need for a deeper understanding of the catalytic active sites and reaction mechanism in order to identify catalyst deactivation pathways and further optimise the catalytic performance.[99,107–113]

Solid-state NMR is a well-developed technique for structural determination and host-guest investigation studies, and has played an important role in increasing our understanding of heterogeneous catalytic process.[114–117] In particular, solid-state NMR has enabled the detection of the intermediates formed during the MTO reaction and their interactions with zeolite, which are both important in unravelling the mechanism of the reaction. The intermediates that have been observed previously by NMR are cyclic carbenium ions such as polymethylcyclopentenyl cations and polymethylbenzenium cations on H-SAPO-34,[88] H-SSZ-13,[88] DNL-6[118] and β-zeolite,[104] and polymethylcyclopentenyl cations and ethylated cyclopentenyl cations on H-ZSM-5 zeolite.[95,105] These cyclic carbenium ions are crucial intermediates involved in the hydrocarbon pool mechanism[92] in which the cyclic organic species in the zeolite pores act as co-catalysts for the conversion of methanol to olefins.[99] More specifically, two reaction routes have been proposed namely the side-chain methylation route in which the olefins are produced through the methylation of polymethylbenzenium ions and the subsequent elimination of the side

chain groups, and the paring route in which the olefins are released *via* the expansion of polymethylcyclopentenyl cations and the subsequent contraction of polymethylbenzenium ions.[88,100,101,119] The structural identification of carbenium ions is crucial for the determination of the dominant route and specific reaction path in different zeolites.

Previous work relied on computational methods for the assignments of the ^{13}C solid-state NMR spectra of the carbenium ions.[88,95] Although these computational methods are recognised robust approaches for NMR spectral interpretation,[120,121] there is still a direct lack of experimental data supporting these assignments and therefore this may lead to possible misinterpretation of the carbenium ions produced. Additionally, the identification of the carbenium ions was indirectly obtained by digesting the dienes (the deprotonated counterparts of the cyclic carbenium ions) with concentrated sulfuric acid and analysing the obtained solutions by liquid-state NMR.[88,105] This procedure assumes that the states of the carbenium ions in the solutions are the same as those confined in the solid zeolite pores, and also requires independent synthesis of the dienes, and therefore entails prior knowledge of the possible carbenium ions' structures.

Recently, the interactions between the carbon species and the Al sites of the H-ZSM-5 zeolite were qualitatively investigated by using spatially encoded ^{13}C-^{27}Al dipolar coupling NMR experiments (employing a symmetry-based resonance-echo saturation-pulse double-resonance sequence (S-RESPDOR) sequence[122]). The work demonstrated the formation of supramolecular reaction centres

composed of confined carbon species and the inorganic framework of zeolite which possesses higher reactivity toward methanol in the H-ZSM-5 zeolite.[109]

Here, we unambiguously experimentally identified several cyclic carbenium ions on MTO activated H-ZSM-5 zeolite, including a previously undetected 1,5-dimethyl-3-*sec*-butyl cyclopentenyl cation, using a refocused INADEQUATE[11] NMR sequence. This experiment relies on scalar J couplings and yields through-bond correlations, providing a straightforward pathway for ^{13}C spectral assignments. Moreover, the interactions between the confined carbon species and H-ZSM-5 zeolite framework are quantitatively probed *via* through space $^{13}C\{^{27}Al\}$ S-RESPDOR[122,123] and $^{29}Si\{^{13}C\}$ REDOR experiments.[16] The framework of H-ZSM-5 zeolite and its micropore size are shown in Figure 2.1.

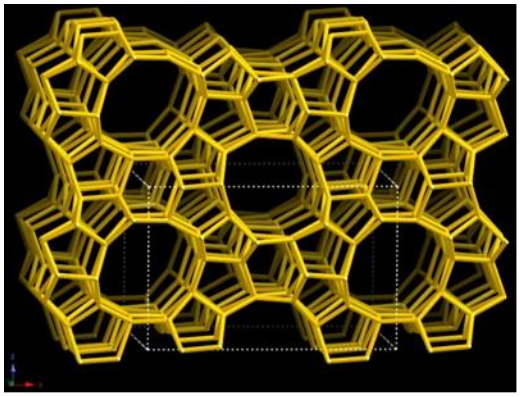

Framework viewed along [010]

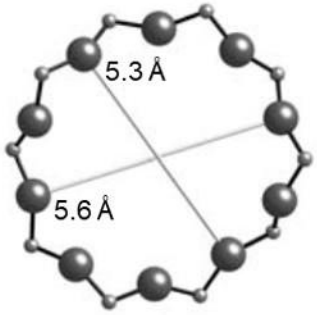

10-ring viewed along [010]

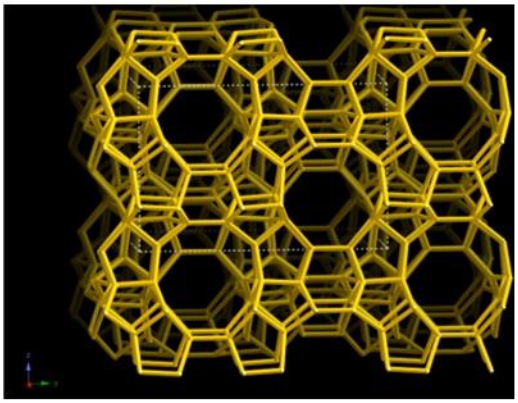

Framework viewed along [100]

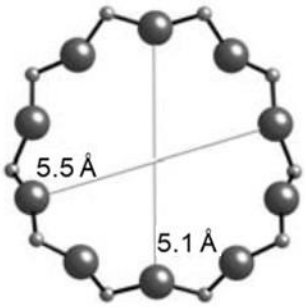

10-ring viewed along [100]

Figure 2.1 Framework of H-ZSM-5 zeolite and its micropore size.[124,125] [010] and [100] denote crystallographic directions.

2.3 Experimental Procedures

2.3.1 Preparation of the MTO activated H-ZSM-5 zeolite

H-ZSM-5 (SiO_2/Al_2O_3 = 50, from Nankai University Catalyst Co., Ltd) of 40 ~ 60 mesh particles was placed at a fixed-bed quartz tubular reactor, and was dehydrated prior to reaction by heating at 550 ^oC under a continuous flow of pure helium flow for 2h. After dehydration, the temperature was gradually decreased to the reaction temperature of 285 ^oC. The ^{13}C enriched methanol (99 atom % ^{13}C, Sigma-Aldrich) was then fed by passing the carrier gas (He)

through a methanol saturator maintained at 14 ^{o}C with the WHSV of methanol to be 2.0 h^{-1}. After running at 285 ^{o}C for 20 minutes, the reaction was quenched by immersing the reactor into liquid N_2. It was measured that the temperature of the catalyst bed decreased from the reaction temperature to room temperature in about 10 seconds. At the same time, the reacting gas was switched to pure helium gas. Once back to room temperature, the reactor was transferred to the N_2 glove box, and the activated zeolite was collected and stored. Samples were vacuumized and sealed in plastic bags using a vacuum packer in the N_2 glove box for storage and transportation. Samples were packed into NMR rotors in air at room temperature.

It should be noted that the industrial MTO process is operated at temperature of 400 to 500 ^{o}C and pressure close to atmospheric pressure.[96,108] However, at such high temperature, the carbenium ion intermediates are very reactive and can hardly be captured.[88] To capture the carbenium ions, the reaction temperature was reduced to about 285 ^{o}C in this work.

2.3.2 NMR experimental details

Experimental details are given in Table 2.1, Table 2.2 and Table 2.3. All NMR data were processed using TopSpin3.2 NMR software.

Table 2.1 Acquisition parameters for ^{13}C solid-state NMR experiments

Experiment	^{13}C CP		^{13}C CP refocused INADEQUATE	^{13}C CP Hahn echo
Magnetic field / T	9.4[a]	20[b]	9.4[a]	9.4[a]
Number of scans	2560	2048	512	1280
Recycle delay / s	2.5	3	3	3
MAS rate / kHz	14	18	14	14
^{1}H rf[c] field for 90° pulse / kHz	70	83	70	70
CP contact time / ms	2	4	2	2
^{1}H rf amplitude ramp for contact pulse / kHz	ramp70 100.100[d]	ramp.10 0[e]	ramp70100. 100[d]	ramp701 00.100[d]
^{1}H rf field during contact pulse / kHz	60	70	60	60
^{13}C rf field during contact pulse / kHz	56	54	56	60
^{1}H rf field for SPINAL64[8] decoupling pulses / kHz	70	83	70	70
^{13}C rf field for 90° and 180° pulses / kHz	-	-	70	60
Rotor synchronized delays for both echoes (τ_1 and τ_2) / ms	-	-	2.1(τ_1), 1.4(τ_2)	-
Δt_1 / us	-	-	14.3	-
Number of t_1 increments	-	-	442	-
Rotor synchronized echo time	-	-	-	66 µs to 9.3 ms
Number of data points	-	-		18

[a] Recorded on a Bruker Avance III HD solid-state NMR spectrometer, using a

4 mm HXY probe in double resonance mode with the resonance frequencies of ^{1}H and ^{13}C to be 400.1 MHz and 100.6 MHz, respectively. [b] Recorded on a Bruker Avance III NMR spectrometer, using a 3.2 mm HXY probe in double resonance mode with the resonance frequencies of ^{1}H and ^{13}C to be 850.2 MHz and 213.8 MHz, respectively. [c] "rf" refers to radio-frequency. [d] 1H contact rf field is swept from 70 to 100% of the set ^{1}H rf field linearly with 100 steps during contact pulse. [e] ^{1}H contact rf field is swept from 50 to 100% of the set ^{1}H rf field linearly with 100 steps during contact pulse.

Table 2.2 Acquisition parameters for ^{13}C and ^{27}Al solid-state NMR experiments

Experiment	$^{13}C\{^{27}Al\}$ CP S-RESPDOR	^{27}Al Hahn echo
Magnetic field / T	9.4[a]	20[b]
Number of scans	768 to 9216	1024
Recycle delay / s	3	0.7
MAS rate / kHz	8	22
^{1}H rf field for 90° pulse / kHz	83	-
CP contact time / ms	2	-
^{1}H rf amplitude ramp for contact pulse / kHz	ramp70100.100	-
^{1}H rf field during contact pulse / kHz	60	-
^{13}C rf field during contact pulse / kHz	40	-
^{1}H rf field for CW decoupling pulses / kHz	83	-
^{1}H rf field for SPINAL64 decoupling pulses / kHz	83	-
^{27}Al rf field for saturation pulse / kHz	40	-
^{13}C rf field for 90° and 180° pulses / kHz	31	-
^{13}C rf field for $SR4_1^2$ recoupling sequences / kHz	16	-
^{27}Al rf field for 90° and 180° pulses / kHz	-	70
Rotor synchronized echo time	-	45 μs

[a] Recorded on a Bruker Avance III HD solid-state NMR spectrometer, using a 4 mm HXY probe in double resonance mode with a frequency splitter (REDOR-BOX)[123] attached to X channel, which enabled tuning and matching to both ^{13}C, ^{27}Al Larmor frequencies at 100.6 MHz and 104.3 MHz, repectively, on X channel. [b] Recorded on a Bruker Avance III NMR spectrometer, using a 3.2 mm HXY probe in single resonance mode with the resonance frequencies of ^{27}Al to be 221.6 MHz.

Table 2.3 Acquisition parameters for ^{29}Si solid-state NMR experiments

Experiment	^{29}Si CP	^{29}Si{^{13}C} CP REDOR	
Magnetic field / T	9.4[a]	9.4[a]	20[b]
Number of scans	10240	10240	2048
Recycle delay / s	3	3	3
MAS rate / kHz	5	5	10
^{1}H rf field for 90° pulse / kHz	83	83	83
CP contact time / ms	3	3	9
^{1}H rf amplitude ramp for contact pulse / kHz	ramp.100	ramp.100	ramp.100
^{1}H rf field during contact pulse / kHz	60	60	70
^{1}H rf field for SPINAL64 decoupling pulses / kHz	83	83	83
^{29}Si rf field during contact pulse / kHz	47	47	50
^{29}Si rf field for 180° pulses / kHz	-	48	50
^{13}C rf field for 180° pulses / kHz	-	60	50
Number of data point	-	5	4
Recoupling time of first data point / ms	-	1.2	1.6
Recoupling time increment / ms	-	1.2	1.0

[a] Recorded on a Bruker Avance III HD solid-state NMR spectrometer, using a 4 mm HXY probe in triple resonance mode with the resonance frequency of ^{1}H to be 400.1 MHz, X channel tuned to ^{13}C at 100.6 MHz, Y channel tuned to ^{29}Si at 79.5 MHz, respectively. [b] Recorded on a Bruker Avance III NMR spectrometer, using a 3.2 mm HXY probe in triple resonance mode with the resonance frequency of ^{1}H to be 850.2 MHz, X channel tuned to ^{13}C at 213.8 MHz, Y channel tuned to ^{29}Si at 168.9 MHz, respectively.

2.3.3 NMR pulse programs

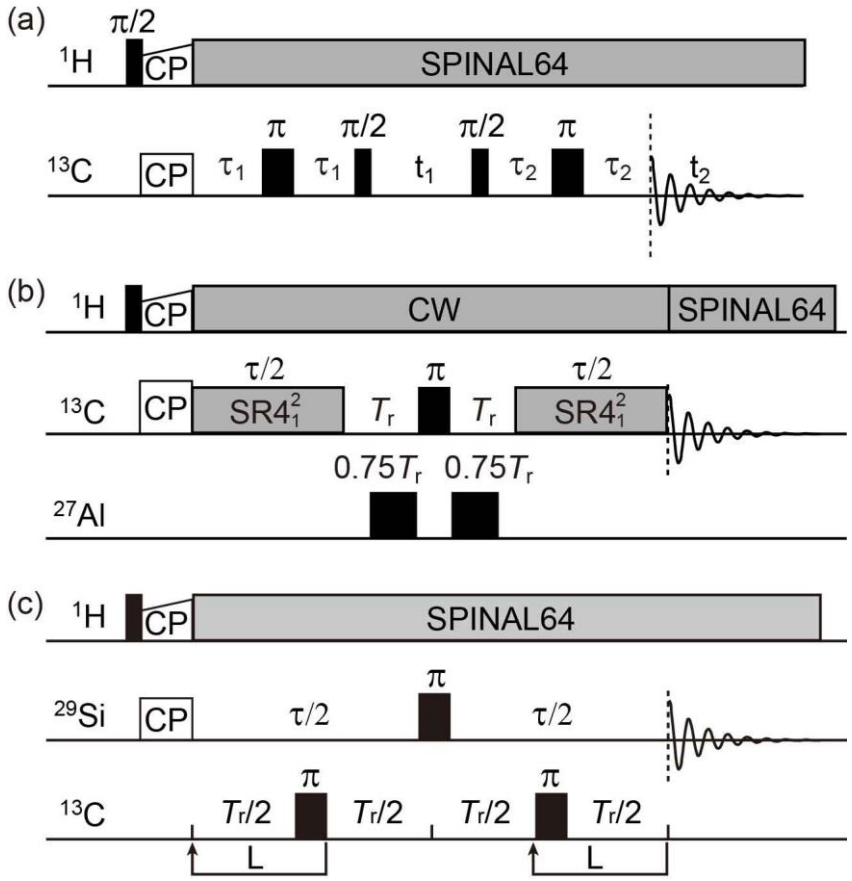

Figure 2.2 (a) ^{13}C CP refocused INADEQUATE pulse sequence.[11] τ_1 and τ_2 are synchronized to be an integer number of rotor periods. (b) ^{13}C{^{27}Al} CP S-RESPDOR pulse sequence.[122,123] $SR4_1^2$ is the recoupling sequence.[126] T_r = $1/\nu_r$ is the rotor period. (c) ^{29}Si{^{13}C} CP REDOR pulse sequence. L is number of rotor periods.[16,127] τ in (b) and (c) represents the recoupling time.

2.3.4 ^{13}C{^{27}Al} S-RESPDOR and ^{29}Si{^{13}C} REDOR data processing

2.3.4.1 Analytical formulas for ^{13}C{^{27}Al} S-RESPDOR

The S-RESPDOR dephasing curve for a spin-1/2 nucleus coupled to any spin-*I* nucleus follows the general formula below:[122,123]

$$\frac{\Delta S}{S_0} = \frac{f}{2I+1}\left\{2I - \frac{\pi\sqrt{2}}{4(2I+1)}\sum_{k=1}^{2I}[4I - 2(k-1)]J_{1/4}\left(\frac{k\pi D\tau}{4}\right)J_{-1/4}\left(\frac{k\pi D\tau}{4}\right)\right\}$$

Equation 2.1

where I is the spin quantum number, I = 5/2 for ^{27}Al nucleus. f is the pre-factor that represents the fraction of crystallites in which the spin states of the quadrupolar nuclei have been saturated by the saturation pulses. This pre-factor is equal to 1 only for 100% abundant nucleus I completely saturated by the saturation pulses. D represents the dipolar coupling constant (unit in "Hz") of ^{13}C-^{27}Al spin pair, and τ is the total duration of $SR4_1^2$ recoupling sequences. $J_{\pm1/4}$ denotes the ±1/4-order Bessel function of the first kind.

2.3.4.2 Analytical formulas for ^{29}Si{^{13}C} REDOR

For short dipolar recoupling times ($\Delta S/S_0 < 0.3$), the REDOR curve is geometry-independent, and a first-order approximation can be applied, which gives the following formula:[128]

$$\frac{\Delta S}{S_0} = \frac{16}{15}\tau^2\sum_{i=1}^{n} D_i^2$$

Equation 2.2

where τ and D_i are the dipolar recoupling time and the dipolar coupling constants (unit in "Hz") of different ^{29}Si-^{13}C spin pairs, respectively.

Both the ^{13}C{^{27}Al} S-RESPDOR and ^{29}Si{^{13}C} REDOR data were fitted using MatLab R2016a software.

The internuclear distance can then be calculated from the obtained dipolar coupling constants D_i according to equation 1.12.

2.3.4.3 Determination of errors

The errors of S' and S_0 are determined from the signal to noise ratios

S/N of S' and S_0 spectra as measured by the TopSpin3.2 NMR software. The noise intensities which are calculated from the intensities of signals and S/N values, are taken as the absolute errors of the signals. The values are $S'/(S/N)_{S'}$) for S' and $S_0/(S/N)_{S0}$ for S_0. Since $\Delta S = S_0 - S'$, the absolute errors of ΔS will be $\{S'/(S/N)_{S'} + S_0/(S/N)_{S0}\}$, which give the absolute errors of $\Delta S/S_0$ that is $\{(S'/S_0)/(S/N)_{S'} + 1/(S/N)_{S0}\}$ and are shown as error bars in Figure 2.9(b) and Figure 2.14.

The $\Delta S/S_0$ data set including the errors were fitted with MatLab and gave a dipolar coupling constant D with associated error at 95 % confidence bounds. The largest and smallest D values are taken as the boundaries, as shown as dashed curves in Figure 2.9(b) and Figure 2.14 while the solid curves correspond to the best-fit of $\Delta S/S_0$ data set without considering the errors.

2.4 Results and discussion

2.4.1 Structural identification of the confined carbon species in MTO activated H-ZSM-5

2.4.1.1 1D ^{13}C CP spectra of MTO activated H-ZSM-5

In this work, the MTO activated H-ZSM-5 materials were prepared by passing ^{13}C enriched CH_3OH over H-ZSM-5 at 285 °C for 20 minutes following by quenching the reaction mixture with liquid N_2 (see section 2.3.1). The ^{13}C CP MAS NMR spectra of the ^{13}C enriched MTO activated H-ZSM-5 are given in Figure 2.3 (at 9.4 T and 20 T) and show multiple signals ranging from 0 to 260 ppm, highlighting the complexity of the confined carbon species. It is worth pointing out that the unusual downfield ^{13}C resonances (235-260 ppm) are characteristic signals of

protonated carbenium ions and these have previously been assigned to several methylated and ethylated cyclopentenyl cations[95,105] whose overlapping resonances prevent their unequivocal assignments.

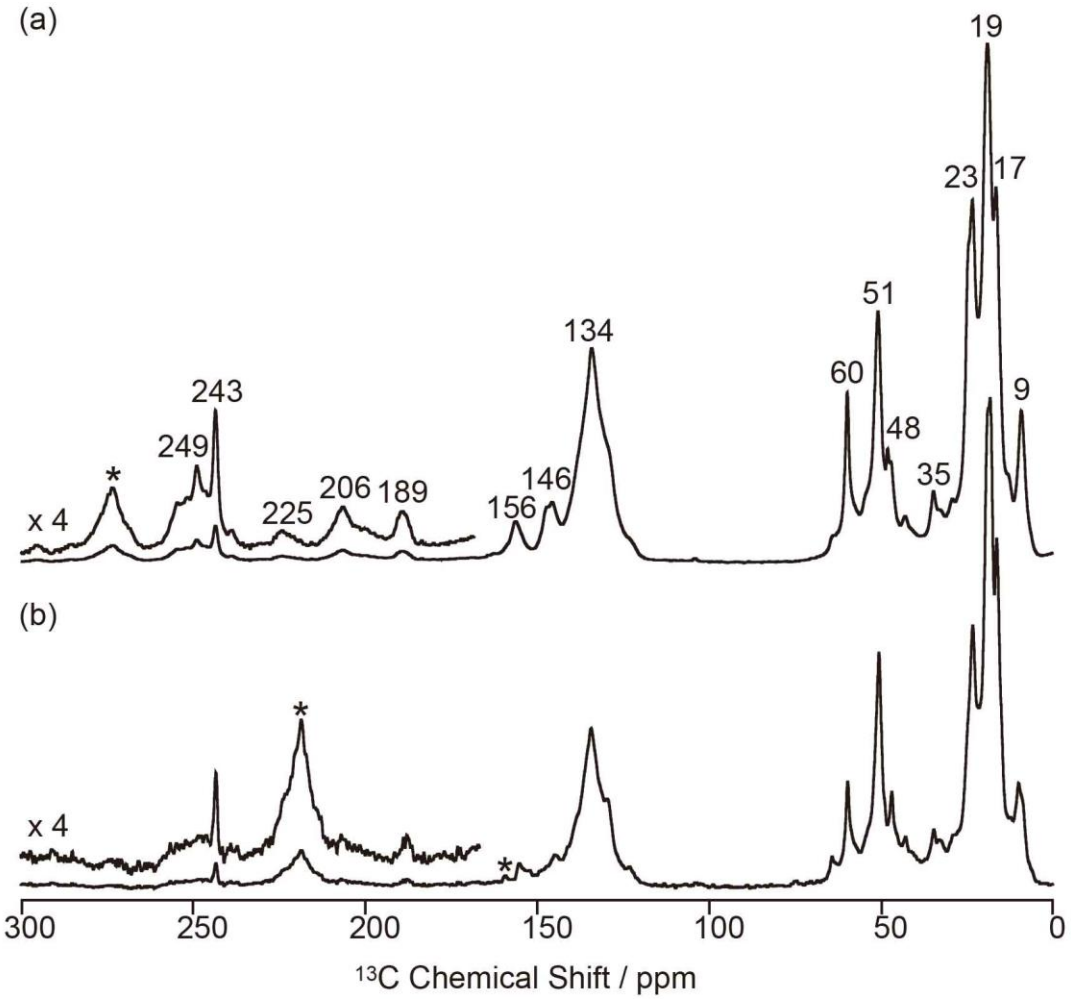

Figure 2.3 ^{13}C CP MAS NMR spectra of ^{13}C enriched MTO activated H-ZSM-5 obtained at (a) an external magnetic field B_0 = 9.4 T, MAS = 14 kHz and (b) B_0 = 20 T, MAS = 18 kHz. Asterisks (*) denote spinning sidebands.

2.4.1.2 Identification of carbenium ions by 2D ^{13}C-^{13}C INADEQUATE

A 2D ^{13}C-^{13}C refocused INADEQUATE spectrum is displayed in Figure 2.4(a) and gives correlations mapping out the carbon skeleton of each carbenium ions. In this J-based experiment, two directly bonded

^{13}C nuclei share a common frequency in the double quantum (vertical) dimension at the sum of their ^{13}C individual frequencies in the single quantum (horizontal) dimension.[11] The peaks observed in the INADEQUATE spectrum notably allowed us to explicitly identify the three methylated carbenium ions, namely the dimethylcyclopentenyl cation **I**, trimethylcyclopentenyl cation **II** and pentamethylbenzenium cation **III** (see Figure 2.4(b)) which have been previously proposed but were identified based on a combination of 1D ^{13}C CP NMR spectra, GC-MS and DFTcalculations.[95] More explicitly, the dimethylcyclopentenyl cation **I** can be identified through correlations C1(**I**) (249 ppm) – C2(**I**) (147 ppm), C1(**I**) (249 ppm) – C3(**I**) (48 ppm) and C1(**I**) (249 ppm) – C4(**I**) (25 ppm) as identified in purple in Figure 2.4(a) (and in Figure 2.4(c) for all horizontal traces). A similar approach is used to directly establish the carbon connectivities in cations **II** (Figure 2.5) and **III** (Figure 2.6).

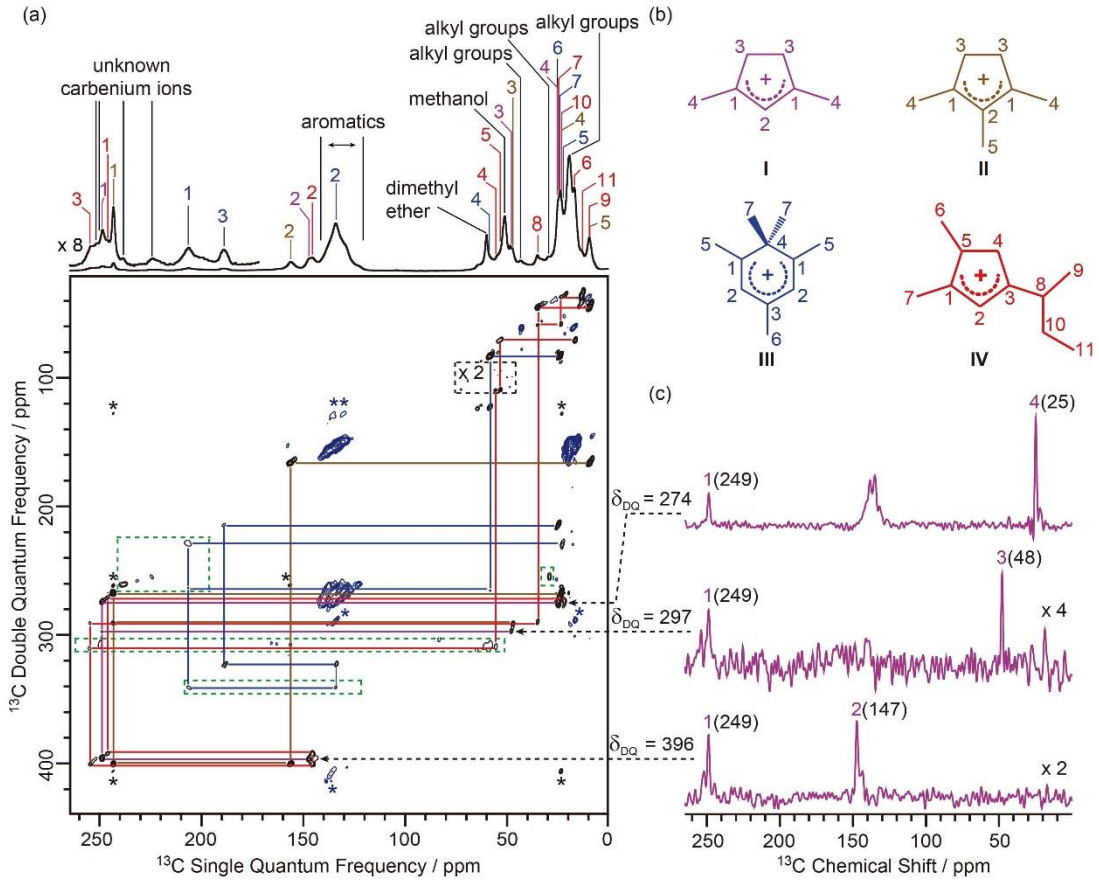

Figure 2.4 (a) 2D ^{13}C-^{13}C refocused INADEQUATE spectrum of ^{13}C enriched MTO activated H-ZSM-5 at B_0 = 9.4 T and a MAS frequency of ν_r = 14 kHz. Signals in the black dashed box have been magnified by a factor of 2, while signals of the green dashed boxes have been processed with a fewer number of t_1 points and larger line broadening to account for the shorter T_2' values (see Table 2.4 for details) and weak intensities of these ^{13}C signals to make them more easily visible. Signals corresponding to carbenium ions (black) and of other neutral carbon species (blue). The assignments of the different carbenium species are given in different colors. Asterisks (*) denote spinning sidebands. (b) Molecular structure of the carbenium ions identified, color-coded according to their assignments. (c) Extracted horizontal traces of carbenium ion **I** with arrows in dashed lines indicating their positions in the 2D map. The corresponding double quantum frequency δ_{DQ} of each slice is also

given in the figure. The chemical shifts of different ^{13}C sites are given in the parenthesis. Unlabeled peaks are from other carbenium ions or aromatic species.

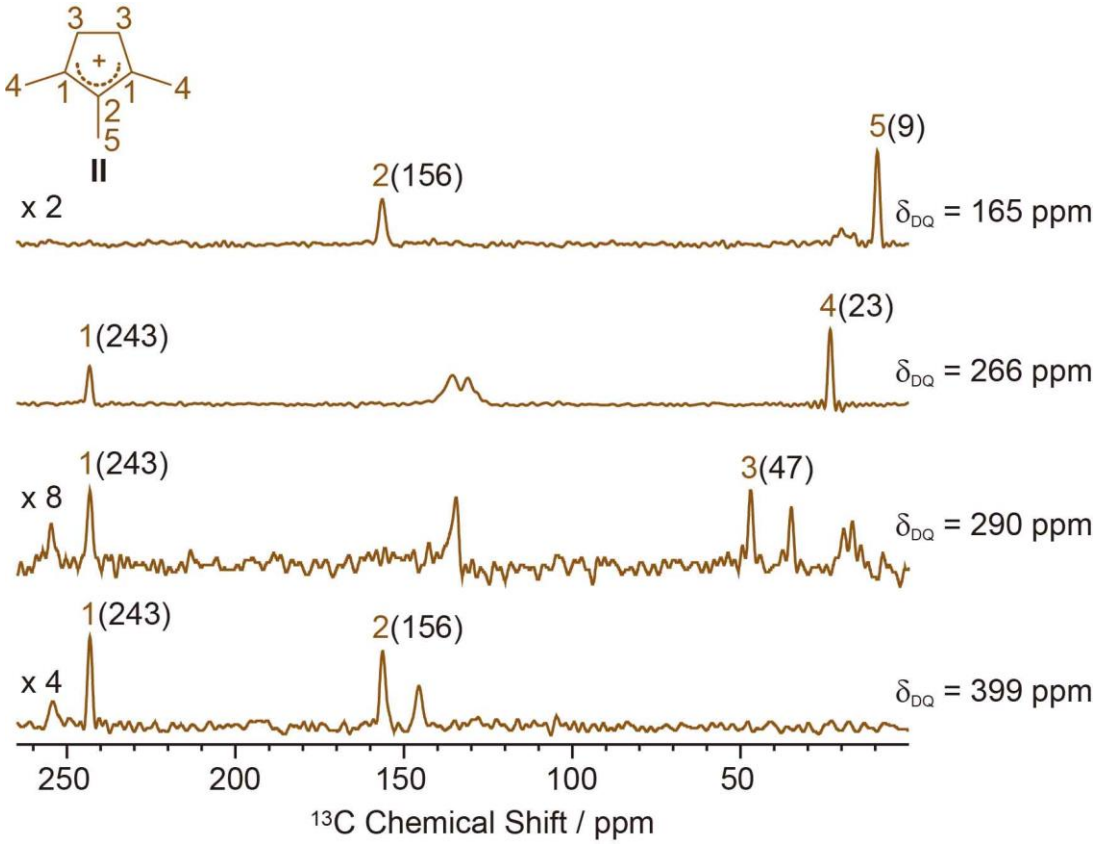

Figure 2.5 Extracted horizontal slices of the 2D ^{13}C INADEQUATE spectrum (Figure 2.4(a)) for carbenium ion **II**. The corresponding double quantum frequency δ_{DQ} of each slice is given in the figure. The chemical shifts of different ^{13}C sites are given in the parenthesis. Unlabeled peaks are from other carbenium ions or aromatic species.

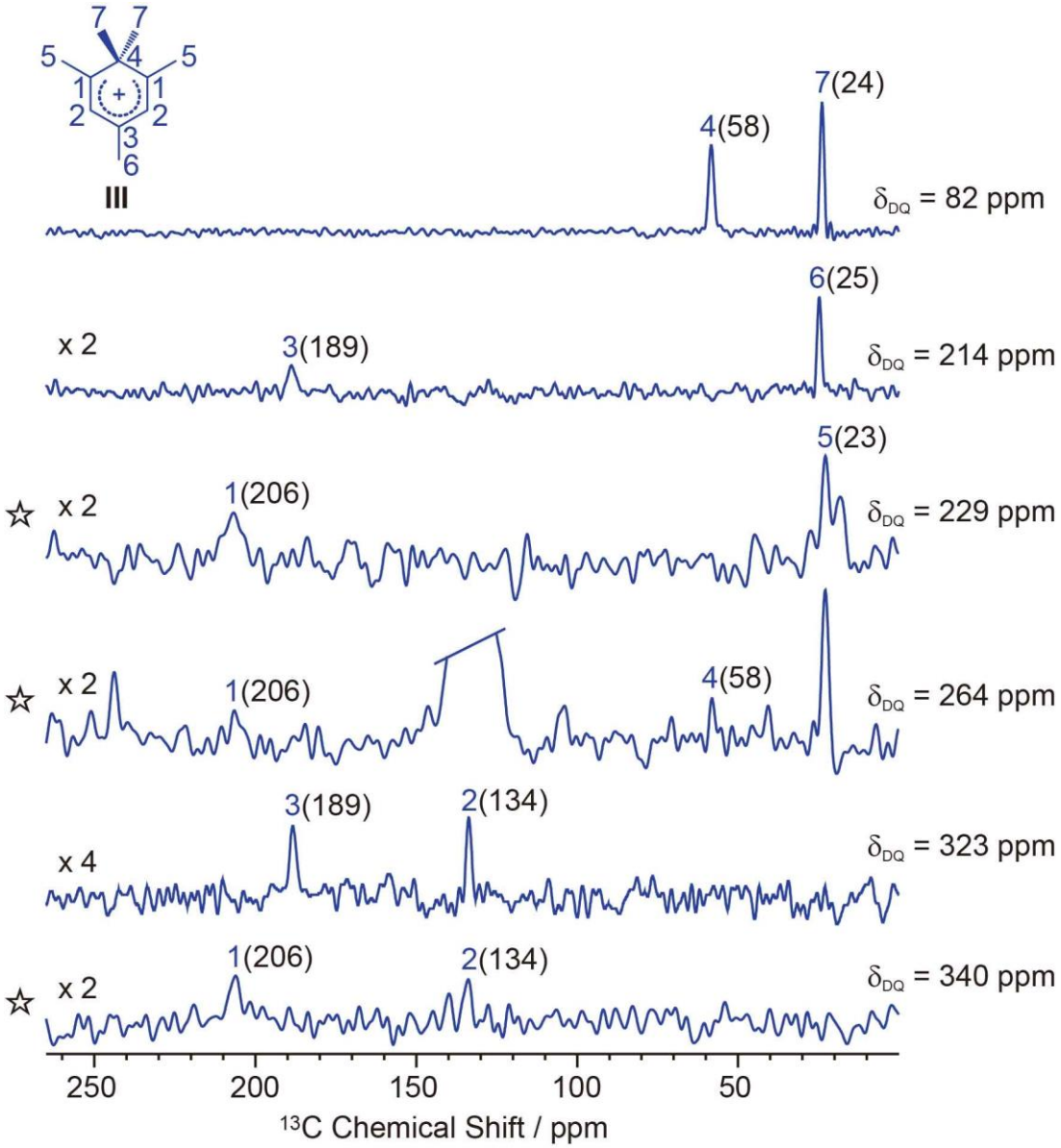

Figure 2.6 Extracted horizontal slices of the 2D ^{13}C INADEQUATE spectrum (Figure 2.4(a)) for carbenium ion **III**. The corresponding double quantum frequency δ_{DQ} of each slice is given in the figure. The chemical shifts of different ^{13}C sites are given in the parenthesis. Slices with "☆" on the left have been processed with a fewer number of t_1 points and larger line broadening. Unlabeled peaks are from other carbenium ions or aromatic species.

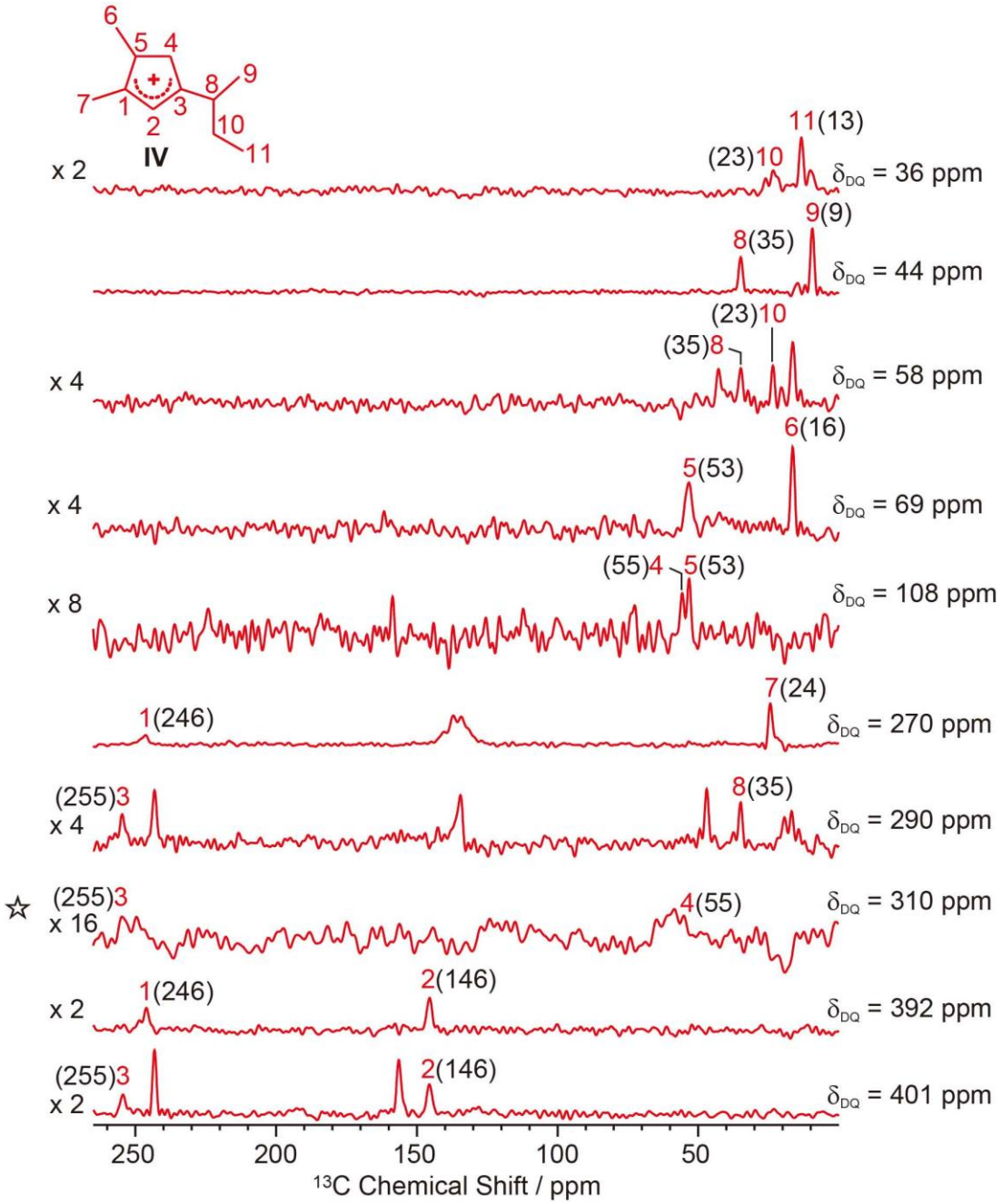

Figure 2.7 Extracted horizontal slices of the 2D ^{13}C INADEQUATE spectrum (Figure 2.4(a)) for carbenium ion **IV**. The corresponding double quantum frequency δ_{DQ} of each slice is given in the figure. The chemical shifts of different ^{13}C sites are given in the parenthesis. Slice with "☆" on the left has been processed with a fewer number of t_1 points and larger line broadening. Unlabeled peaks are from other carbenium ions or aromatic species.

A previously unprecedentedly observed 1,5-dimethyl-3-*sec*-butyl cyclopentenyl cation **IV**, is also identified on H-ZSM-5 as revealed by the C3(**IV**) (255 ppm) - C8(**IV**) (35 ppm), C8(**IV**) (35 ppm) - C9(**IV**) (9 ppm), C8(**IV**) (35 ppm) - C10(**IV**) (23 ppm), C10(**IV**) (23 ppm) - C11(**IV**) (13 ppm) correlations and correlations amongst C1(**IV**) to C8 (**IV**) observed in the 2D ^{13}C-^{13}C refocused INADEQUATE spectra (red lines in Figure 2.4(a) and Figure 2.7). A cyclopentenyl cation with a *tert*-butyl group has previously been reported to be involved as a key intermediate in the aromatic-based paring route proposed by theoretical modelling for the formation of isobutene in the MTO reaction, however, it was not experimentally observed.[101] In contrast, some work proposed that butene is formed through an alkene-based cycle involving the methylation/cracking of alkenes.[129,130] Hence, the experimental identification of cation **IV** provides direct support for the aromatic-based paring route for butene formation in H-ZSM-5. The elimination of the *sec*-butyl group of cation **IV** is likely to produce but-1-ene and but-2-ene which are also the products of the MTO reaction.[131]

Several correlations relating ^{13}C signals in the 235 ppm to 260 ppm region (black lines in Figure 2.8) are also obtained and can be assigned to some additional carbenium ions, most likely cyclopentenyl cations.[95,105] The correlation involving the weak signal at 225 ppm may arise from the polymethylcyclohexenyl cations.[132] However, the lack of correlations relating these signals with the aliphatic region of the ^{13}C NMR spectrum limits the complete assignments of these signals and is probably due to the low concentration of these carbenium ions as

evidenced by their weak signal intensities in the 1D ^{13}C CP MAS spectrum. The low concentration may also account for the apparent absence of ethylated cyclopentenyl cations[105] in our MTO activated H-ZSM-5.

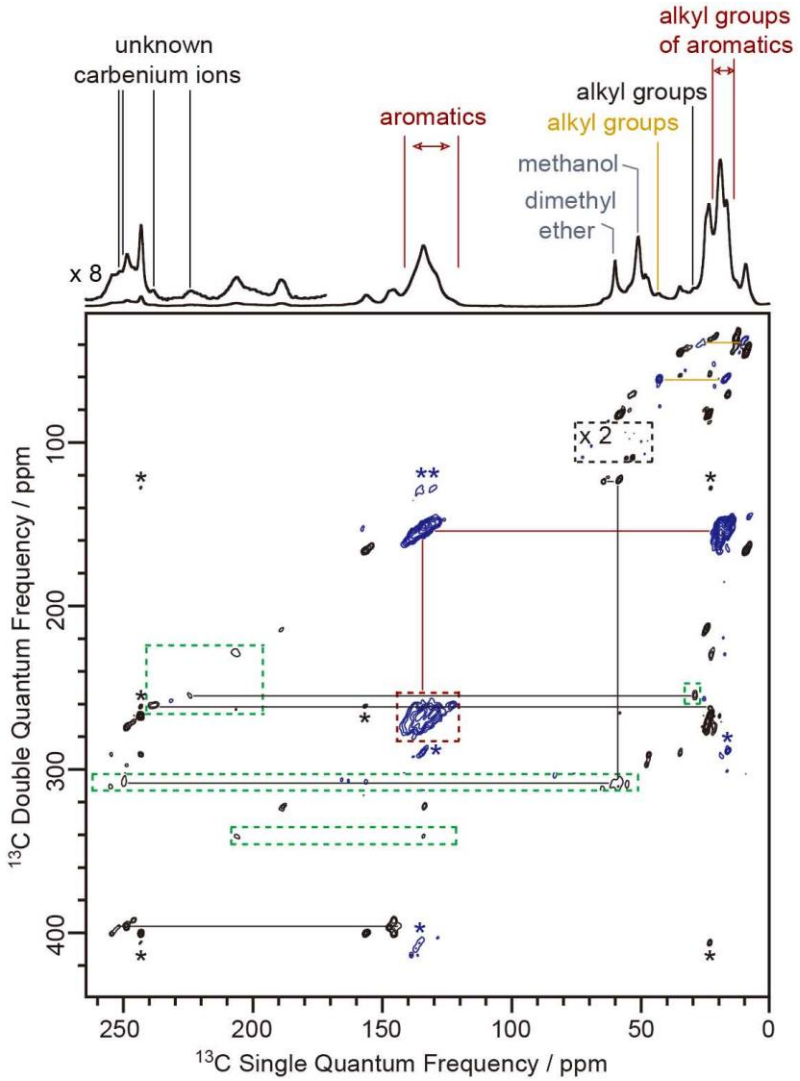

Figure 2.8 2D ^{13}C-^{13}C refocused INADEQUATE spectrum of ^{13}C enriched MTO activated H-ZSM-5 at B_0 = 9.4 T and a MAS frequency of ν_r = 14 kHz. Signals in the black dashed box have been magnified by factor of 2, while signals of the green dashed boxes have been processed with a fewer number of t_1 points and larger line broadening to account for the shorter T_2' values (see Table 2.4 for details) and weak intensities of these ^{13}C signals and make them more easily visible. Signals corresponding to carbenium ions were labelled in black to distinguish them from signals (blue) of other neutral carbon species. Signals in maroon dashed box correspond to correlations amongst carbons of the benzene rings.[95] Asterisks (*) denote spinning sidebands.

Table 2.4 ^{13}C Chemical shift of carbenium ions

Carbenium ions	Carbon number	Chemical shift / ppm	T_2' / ms[a]
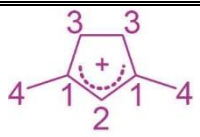 I	1	249	-
	2	147	-
	3	48	-
	4	25	-
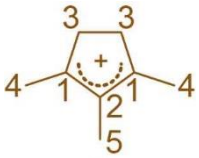 II	1	243	1.6
	2	156	1.6
	3	47	1.9
	4	23	2.9
	5	9	2.8
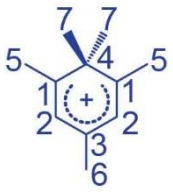 III	1	206	1.6
	2	134	1.2
	3	189	1.9
	4	58	-
	5	23	2.9
	6	25	-
	7	24	-
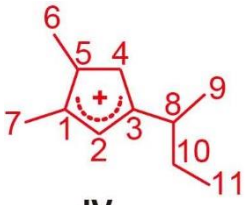 IV	1	246	-
	2	146	1.7
	3	255	-
	4	55	-
	5	53	-
	6	16	-
	7	24	-
	8	35	-
	9	9	2.8
	10	23	2.9
	11	13	-

[a] Measured ^{13}C transverse relaxation time (T_2') under ^{1}H decoupling (Table 2.1) obtained at 9.4 T. T_2' were derived by fitting the data to $I(\tau) = I(0)\exp[-\tau/T_2']$ where $I(\tau)$ and $I(0)$ are the signal intensities at time τ and τ.

The increase of resolution offered in the vertical dimension of the 2D spectrum enables a more accurate determination of the ^{13}C chemical shift values of the different carbon sites from these carbenium ions

(Table 2.4). Those signals are usually poorly resolved in the 1D CP MAS NMR spectrum (Figure 2.3(a) and Figure 2.4(a) for data at 9.4 T) even at a high magnetic field (see Figure 2.3(b)).

2.4.1.3 Neutral carbon species in MTO activated H-ZSM-5

In the 2D ^{13}C-^{13}C refocused INADEQUATE spectrum, signals ranging from 120 to 140 ppm show strong correlations with each other and with signals in the 13 - 22 ppm region (maroon lines in Figure 2.8). These correlations are attributed to correlations amongst carbons of the benzene rings and between benzene rings carbons and alkyl group carbons of neutral aromatic species, respectively. Aromatics with various types and numbers of substituted alkyl groups have very close chemical shifts,[133] which makes individual assignments of signals from these aromatics challenging due to a lack of resolution.

Signals at 60 and 51 ppm have strong intensities in the 1D CP MAS spectrum and show no correlations with any other signals in the 2D spectrum (Figure 2.4(a)). This observation is consistent with their assignments to dimethyl ether and residual adsorbed methanol, respectively.[105] Correlations among peaks between 10 and 45 ppm (orange lines in Figure 2.8) can be assigned to alkyl groups of aromatics or carbenium ions.[105]

2.4.2 Quantitative investigation of the interactions between the confined carbon species and the H-ZSM-5 framework

2.4.2.1 ^{13}C-^{27}Al distance measured by $^{13}C\{^{27}Al\}$ S-RESPDOR

The interactions between the confined carbon species and zeolite are initially investigated by recording $^{13}C\{^{27}Al\}$ S-RESPDOR data, in which the ^{13}C-^{27}Al dipolar couplings are reintroduced by the $SR4_1^2$ recoupling sequences[126] on the ^{13}C spins, and provide access to the intramolecular distance. With ^{27}Al irradiation and at a recoupling time of 15 ms, the S-RESPDOR dephasing $\Delta S/S_0$ obtained at 9.4 T can be clearly observed, indicating spatial proximities between the ^{13}C and ^{27}Al spins. More specifically, signals from 0 to 40 ppm, corresponding to the alkyl groups of both carbenium ions and aromatics, all have similar signal reduction $\Delta S/S_0$ due to being coupled to the ^{27}Al spins (Figure 2.9(a)) and are integrated against the recoupling time in Figure 2.9(b). Due to the small concentration of ^{27}Al atoms in ZSM-5 ($SiO_2/Al_2O_3 = 50$), the ^{13}C spins are unlikely to be coupled with multiple ^{27}Al spins and a single spin pair model is used to fit the S-RESPDOR data[122] (see section 2.3.4 for further details). A ^{13}C-^{27}Al dipolar coupling constant D of 74 ± 12 Hz is extracted and corresponds to an average ^{13}C-^{27}Al distance of 4.7 ± 0.3 Å between the alkyl groups of confined carbon species and the ^{27}Al sites, and the ^{27}Al NMR spectrum in Figure 2.10 shows mainly the framework tetrahedral Al.

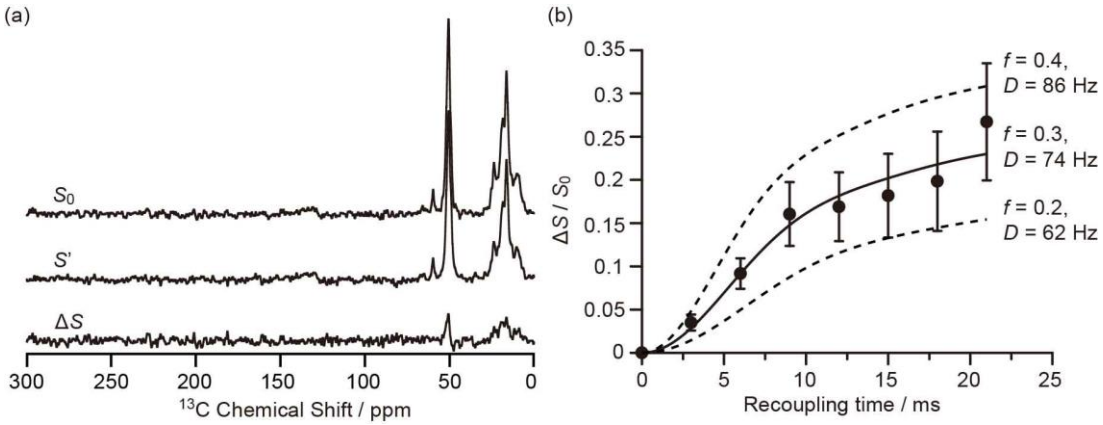

Figure 2.9 (a) $^{13}C\{^{27}Al\}$ S-RESPDOR signals with (S') and without (S_0) ^{27}Al irradiation at external magnetic field B_0 = 9.4 T and with recoupling time of 15 ms. ΔS is the difference spectrum between S_0 and S'. (b) $^{13}C\{^{27}Al\}$ S-RESPDOR fraction $\Delta S/S_0$ as a function of recoupling time with the corresponding best-fit curve (black line) and fit boundaries (dashed lines). f is the pre-factor and D is the dipolar coupling constant (see section 2.3.4). The error bars are determined from the signal to noise ratios of S_0 and S' spectra as measured by the TopSpin3.2 NMR software.

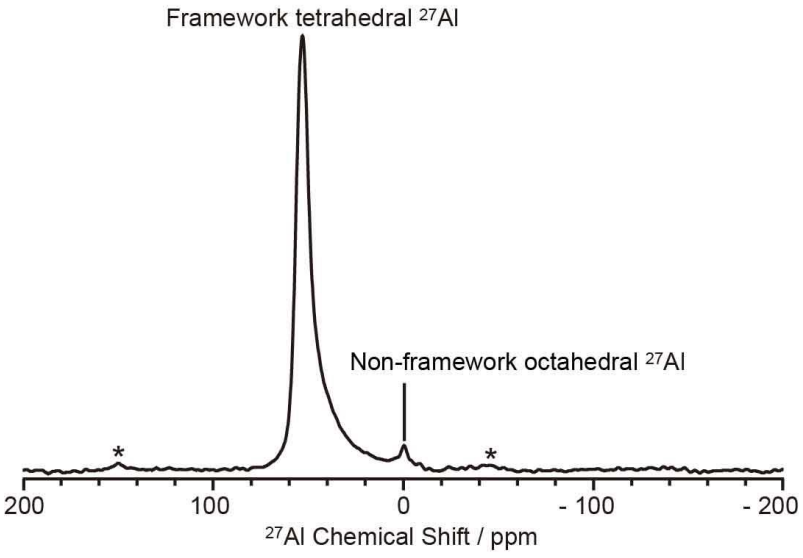

Figure 2.10 ^{27}Al Hahn echo MAS NMR spectrum of ^{13}C enriched MTO activated H-ZSM-5 at B_0 = 20 T. Signal are assigned according to reference[134]. Asterisks (*) denote spinning sidebands.

2.4.2.2 ^{29}Si-^{13}C distance measured by ^{29}Si{^{13}C} REDOR

The 9.4 T ^{29}Si CP MAS NMR spectra of the MTO activated H-ZSM-5 (Figure 2.11) show multiple broad signals at -102, -106, -112 and -117 ppm which are characteristics of the $(SiO)_3SiOH$ (Q^3), $Si(OSi)_3(OAl)$, $Si(OSi)_4$ (Q^4) and the crystallographically inequivalent $Si(OSi)_4$ ($Q^{4'}$) sites, respectively, of which the $Si(OSi)_3(OAl)$ sites contribute to the Brønsted acid sites.[135] Note that no ^{29}Si signal for T_n sites of the type $R\text{-}Si(OSGi)_n(OH)_{3-n}$ (typically observed around -60 ppm[136]) (Figure 2.12(a)) could be detected on H-ZSM-5, indicating that the confined carbon species are not directly covalently bonded to the ^{29}Si nuclei.

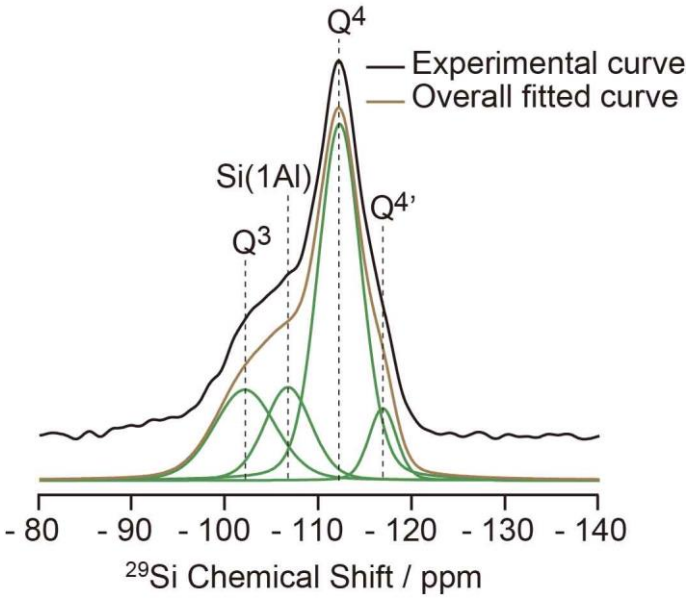

Figure 2.11 Fitting of ^{29}Si CP spectrum at 9.4 T.

Spatial interactions between the confined carbon species and the H-ZSM-5 zeolite framework are further probed by ^{29}Si detected ^{29}Si{^{13}C} REDOR experiments (Figure 2.12(a)) which reintroduce the ^{29}Si-^{13}C dipolar couplings under MAS.[16] At an recoupling time of 6 ms, the

intensity of the dephased ^{29}Si NMR signal *S*' is significantly reduced *vs*. the spin echo signal S_0 indicating spatial proximities between ^{29}Si and ^{13}C spins. Figure 2.12(b) shows that the different ^{29}Si signals have a similar degree of intensity reduction and these signals cannot be well resolved even at a high field of 20 T (Figure 2.13). Therefore, integration of the whole ^{29}Si NMR signals from -90 to -125 ppm was used to determine the REDOR fraction $\Delta S/S_0$ as a function of the recoupling time (Figure 2.14). The number of retained carbon species and their unknown geometries with respect to the zeolite impose the use of a geometrically-independent REDOR curve model in which only data for a short dipolar recoupling time ($\Delta S/S_0 < 0.3$) are needed.[128]

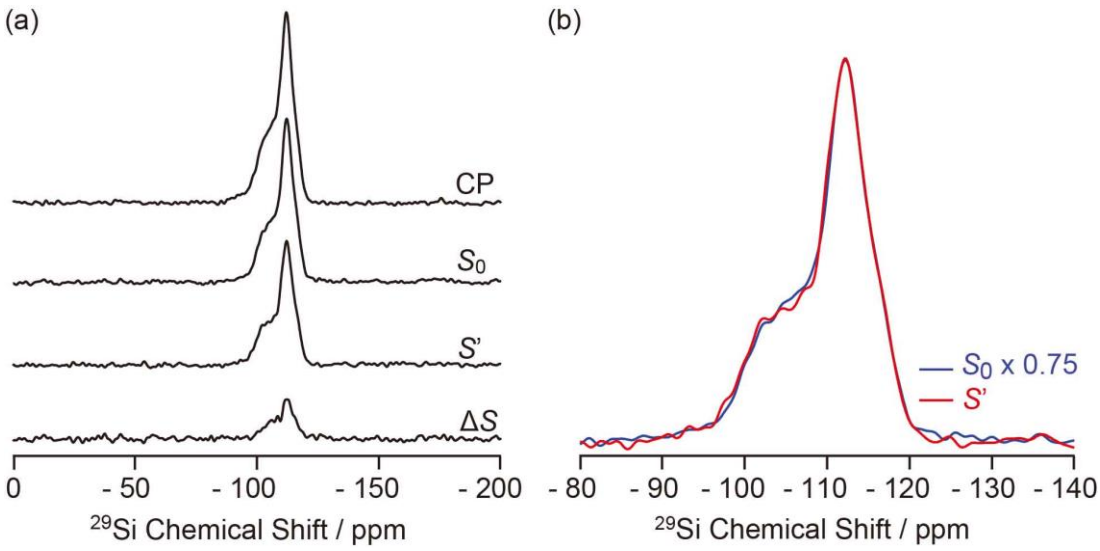

Figure 2.12 (a) ^{29}Si CP, ^{29}Si CP spin echo signal (S_0), ^{29}Si{^{13}C} REDOR signal with reintroduction of dipolar couplings (*S*') at an external magnetic field B_0 = 9.4 T and with a recoupling time of 6 ms. $\Delta S = S_0 - S'$. (b) Comparison of S_0 and *S*' spectra.

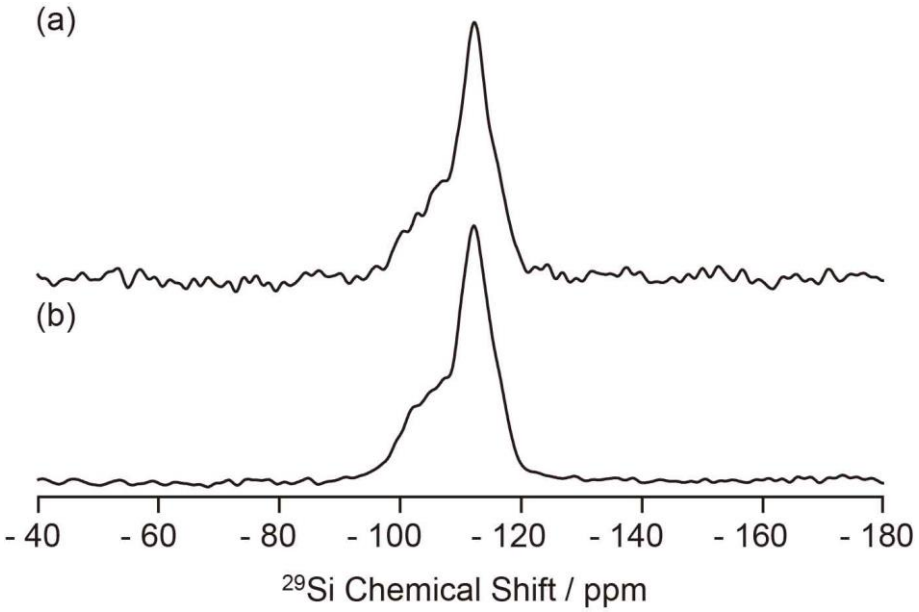

Figure 2.13 Comparison of $^{29}Si\{^{13}C\}$ REDOR signals (a) S_0 at 20 T, MAS = 10 kHz, recoupling time of 1.6 ms and (b) S_0 at 9.4 T, MAS = 5 kHz, recoupling time of 1.2 ms.

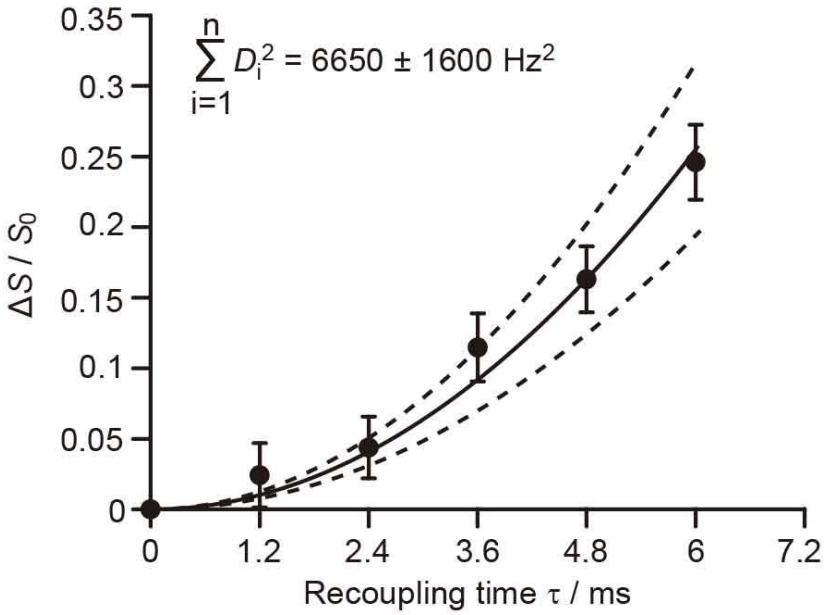

Figure 2.14 Plot of the REDOR fraction $\Delta S/S_0$ as a function of the recoupling time τ with the corresponding best-fit curve (black line) and fit boundaries (dashed lines). Vertical error bars are estimated as for the $^{13}C\{^{27}Al\}$ S-RESPDOR data.

Fitting the $^{29}Si\{^{13}C\}$ REDOR data (see Figure 2.14 and section 2.3.4) yields $\sum D_i^2$ of 6650 ± 1600 Hz^2 which gives an estimated ^{29}Si-^{13}C dipolar coupling constant D of 82 ± 10 Hz (assuming a simplified single spin pair model) and a ^{29}Si to ^{13}C internuclear distance of 4.2 ± 0.2 Å. This distance is comparable to the one obtained above for ^{13}C to ^{27}Al from the $^{13}C\{^{27}Al\}$ S-RESPDOR experiments, showing strong interactions between the confined hydrocarbon species and zeolite framework and providing quantitative information for the proposed supramolecular reaction centres in H-ZSM-5.[109,137]

2.4.2.3 Analysis of the host-guest interactions

The interactions between the neutral aromatics, carbenium ions and H-ZSM-5 have previously been investigated computationally;[138–142] it was found that it is the confinement of pores *via* long-range van der Waals interactions between the neutral aromatics and zeolite framework that contributes considerably more to the aromatics' adsorption in H-ZSM-5 than the short-range interactions between the acid OH group of the zeolite and the electrons of the aromatic ring. These previous works proposed that the aromatics prefer to adsorb in the intersection region between the straight and sinusoidal channels in which polycyclic aromatics grow and block the channels, leading to the catalysts' deactivation.[138–140] The $^{29}Si\{^{13}C\}$ REDOR spectra (Figure 2.12(b)) show that different ^{29}Si sites, including the $Si(OSi)_3(OAl)$ sites corresponding to the Brønsted acid sites, have apparent similar interactions with ^{13}C nuclei, which indicates that the confinement effects dominate the adsorption of the main hydrocarbon species (neutral aromatics), and that

the short-range interactions between the main hydrocarbon species and the Brønsted acid sites may not be strong enough to make a significant difference between these acid sites (and others). These observations suggest that the deactivation of zeolite may not result from the direct poisoning of acid sites, but from blockage of the channels due to the accumulation of aromatics, which is consistent with previous calculations.[138] The adsorption model in previous studies showed that the acid O-H bond axis faces the aromatic ring in a nearly perpendicular orientation with the distance between the acidic H and the aromatic ring falling in the 2.2–2.9 Å range.[138] Considering an Al-H distance of about 2.4 Å[140] and the size of aromatics, both ^{27}Al-^{13}C and ^{29}Si-^{13}C distances around 4–5 Å can be expected, matching the values measured above.

Carbenium ions were previously proposed to form ion-pair complex with the Brønsted acid sites. In the DFT optimised geometry of this complexes, the ^{13}C nucleus directly involved in the ionic bonding interaction is around 3.1 Å away from the O of the Brønsted acid sites. Considering the Al-O and Si-O bond distances (1.7 and 1.6 Å respectively)[141,142] and the local geometry of the complex, distances between this ^{13}C nucleus and ^{27}Al/^{29}Si can be estimated to be around 4 Å. This ^{13}C nucleus is on the carbenium ring in the optimised geometry and should be the closest one to the Al sites. Hence, we can expect a longer distance between the dangling alkyl groups of the carbenium ions and the Al sites, satisfying the experimental value of 4.7 ± 0.3 Å distance as measured by the ^{13}C{^{27}Al} S-RESPDOR experiments.

2.5 Conclusions

In conclusion, we have shown here that a ^{13}C-^{13}C refocused INADEQUATE experiment on a MTO activated H-ZSM-5 leads to the unambiguous assignment of the ^{13}C NMR spectrum and the direct spectroscopic determination of the molecular structures of the retained carbon species inside the zeolite framework. The spatial proximities between these carbon species and the zeolite framework were probed by $^{13}C\{^{27}Al\}$ S-RESPDOR and $^{29}Si\{^{13}C\}$ REDOR experiments for which quantitative analysis reveals carbon-aluminium and carbon-silicon host-guest distances in the range of 4.2–4.7 Å, supporting pore confinement interactions (Figure 2.15).

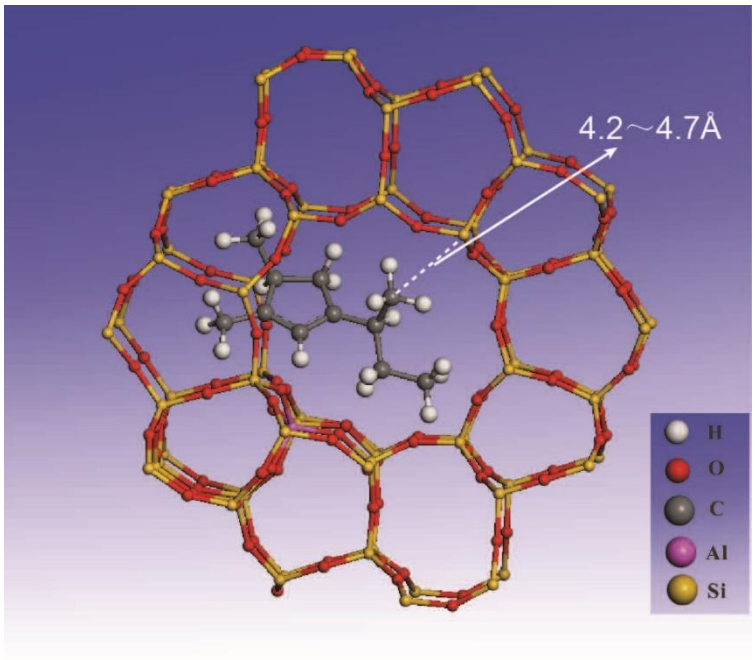

Figure 2.15 Representative of carbenium ion **IV** confined in the pores of H-ZSM-5 and its distance to the zeolite framework.

Chapter 3: Identification of different carbenium ion intermediates in zeolites with identical chabazite topology *via* ^{13}C-^{13}C through-bond NMR correlations

This chapter is adapted from a paper titled of the same name that was published in *RSC Advances* in 2019,[143] for which the authors contribution are as follow: D. X. prepared all the samples, conducted all NMR experiments with assistance from F. B. when required, made all the figures and wrote the initial draft of the manuscript which was enhanced with guidance from F. B.; all authors discussed the results.

3.1 Abstract

^{13}C-^{13}C through-bond NMR correlation experiments reveal the stabilization of different carbenium ion intermediates in two zeolites possessing identical CHA topology (H-SAPO-34 and H-SSZ-13) during the methanol to olefins reaction.

3.2 Introduction

The production of light olefins *via* the methanol-to-olefins (MTO) reaction is an important chemical process that links non-oil resources such as coal and natural gas with olefin-based petrochemicals.[96–98,144,145] The catalysts used for the MTO reaction are mainly microporous acidic zeolites amongst which H-SAPO-34, a silicoaluminophosphate zeolite with the CHA topology, is of particular importance due to its high selectivity to ethylene and propene, and is of commercial use.[96,97] H-

SSZ-13 is a CHA silicoaluminate analogue of H-SAPO-34 which has been shown to be a potential alternative in the MTO process.[146]

Despite the successful industrialization of this process with methanol conversion higher than 99%,[96] further improving of the catalysts performances in terms of selectivity has been an important scientific endeavour. For example, the selectivity to ethylene and propene has increased from 79.2% in the first generation industrial DMTO process ("D" refers to Dalian Institute of Chemical Physics) to 85.7% in the second generation DMTO-II process in China.[96] However, there is still significant room to improve catalysts performances which can be informed by providing a deeper understanding of the catalytic reaction intermediates and reaction mechanism.

We and others have previously investigated the MTO mechanism on H-ZSM-5,[95,106,111,147] H-SAPO-34[88,92,93,137] and β zeolite[67,119] using a range of experimental and computational approaches including solid-state NMR. The hydrocarbon pool (HCP) mechanism has been generally accepted for the formation of hydrocarbons from methanol[81,92,93,99,145] and suggests that for the aromatic cycle routes the organic species (mainly cyclic carbenium ions and neutral aromatic species) confined in the pores of zeolites act as co-catalysts with the inorganic framework. Based on the species observed, a side-chain and a paring reaction pathways have been proposed. While the former involves olefins released through methylation of six-membered ring cations (alkylbenzenium) and elimination of the side chain groups, the later route produces the olefins *via* expansion of alkylcyclopentenyl cations

followed by contraction of the formed six-membered ring cations.[88,100,119] These cyclic carbenium ions are key nodes along the reaction routes and their identification plays an important role in determining the mechanism acting for a given zeolite.

Solid-state NMR has played a critical role in achieving this understanding[88,95,102,148] and our works[67,106] deploying a range of multidimensional and multinuclear NMR approaches have enabled the unequivocal structural identification of a range of five- and six-membered ring cations (as well as neutral compounds) in H-ZSM-5 and β-zeolites (MFI and BEA topologies, respectively), without the need for previous knowledge or assumption of the carbenium ions structures. In particular, this approach permits to distinguish carbenium ions with closely related structures (*e.g.*, cyclopentenyl cations with various methyl groups) and previously unidentified carbenium ions (*e.g.*, 1,5-dimethyl-3-*sec*-butyl cyclopentenyl cation and methylnaphthalenium cations), all offering a complete understanding of the reaction routes.

Here, we probe the carbenium ions formed during the MTO reaction on two different CHA zeolites (H-SSZ-13 and H-SAPO-34) by utilizing the 2D ^{13}C-^{13}C refocused INADEQUATE[11] NMR experiment (pulse program can be found in section 2.3.3 of chapter 2). We experimentally identified 1,2,3,4-tetramethylcyclopentenyl (**I**) and 1,2,3-trimethylcyclopentenyl (**II**) cations as the major retained cation species on H-SSZ-13 and H-SAPO-34 CHA zeolites, respectively. The framework of H-SSZ-13 and H-SAPO-34 zeolites and their micropore size are shown in Figure 3.1.

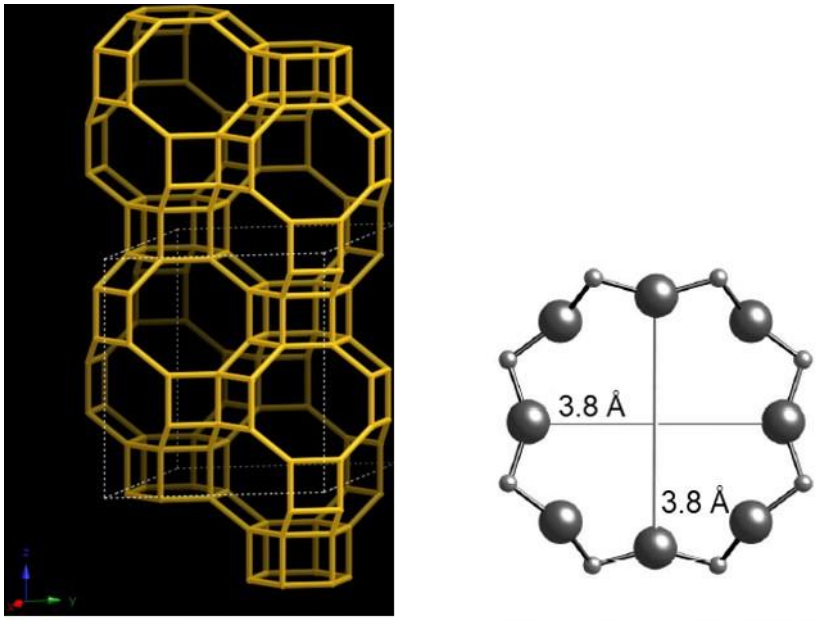

Figure 3.1 CHA framework of H-SSZ-13 and H-SAPO-34 zeolites and their micropore size.[124,125] [001] denotes crystallographic direction.

3.3 Experimental Procedures

3.3.1 Preparation of the MTO activated CHA zeolites

Templated SAPO-34 (Al + P)/Si ≈ 7) with triethylamine was purchased from Nankai University Catalyst Co., Ltd and H-SSZ-13 (Si/Al = 15) was provided by BASF.[88] The templated SAPO-34 zeolite was calcined in air at 550 °C for 6 h to remove the organic template and generate the H-type zeolite. Both H-SAPO-34 and H-SSZ-13 zeolites with particles in the 40 ~ 60 mesh range were placed in a fixed-bed quartz tubular reactor and dehydrated first at 500 ^{o}C under a continuous helium (99.999%, Dalian Special Gases Co., Ltd.) flow for 2 h. The temperature was then gradually decreased to the reaction temperature as follow. H-SAPO-34 and H-SSZ-13 were then reacted with $^{13}CH_3OH$ (99 atoms % ^{13}C, Sigma-Aldrich) with a WHSV of 2 h^{-1} at 300 °C for

20 minutes and at 275 °C for 25 minutes, respectively. Liquid N_2 was then used to quench the reaction by immersing the reactor into it, the input gas switched to helium and once cooled to room temperature, the reactor was transferred to a glove box protected by N_2 for storage. The activated zeolites were packed into NMR rotors quickly in air at room temperature.

3.3.2 NMR experimental details

The NMR experimental details for activated H-SSZ-13 and H-SAPO-34 are shown in Table 3.1 and 3.2, respectively. The data were processed using the TopSpin3.2 NMR software.

Table 3.1 NMR spectra acquisition parameters for activated H-SSZ-13

Experiment	^{13}C CP[a]			^{13}C CP refocused INADEQUATE[a]
MAS rate / kHz	8	12.5	14	14
Number of scans	2048	2048	4096	192
Recycle delay / s	3	3	3	3
^{1}H rf[b] field for 90° pulse / kHz	70	70	70	70
CP contact time / ms	2	2	2	2
^{1}H rf amplitude ramp for contact pulse / kHz	ramp70100.100[c]	ramp70100.100	ramp70100.100	ramp70100.100
^{1}H rf field during contact pulse / kHz	60	60	60	60
^{13}C rf field during contact pulse / kHz	60	60	64	46
^{1}H rf field for SPINAL64[149] decoupling pulses / kHz	70	70	70	70
^{13}C rf field for 90° and 180° pulses / kHz	-	-	-	70
Rotor synchronized delays for both echoes (τ_1 and τ_2) / ms	-	-	-	2.1(τ_1) 2.1(τ_2)
Δt_1 / us	-	-	-	14.3
Number of t_1 increments	-	-	-	962

[a] All recorded on a 9.4 T Bruker Avance III HD solid-state NMR spectrometer, using a 4 mm HXY probe in double resonance mode. The corresponding resonance frequencies of ^{1}H and ^{13}C are 400.1 MHz and 100.6 MHz, respectively. [b] "rf" stands for rf. [c] ^{1}H contact rf field is swept from 70 to 100% of the set ^{1}H rf field linearly with 100 steps during contact pulse.[150]

Table 3.2 NMR spectra acquisition parameters for activated H-SAPO-34

Experiment	^{13}C CP[a]			^{13}C CP refocused INADEQUATE[a]
MAS rate / kHz	10	13.5	14	14
Number of scans	4096	15024	25056	384
Recycle delay / s	3	3	3	3
^{1}H rf field for 90° pulse / kHz	70	83	70	70
CP contact time / ms	2	2	2	2
^{1}H rf amplitude ramp for contact pulse / kHz	ramp70100.100	ramp70100.100	ramp70100.100	ramp70100.100
^{1}H rf field during contact pulse / kHz	60	60	60	60
^{13}C rf field during contact pulse / kHz	56	56	58	46
^{1}H rf field for SPINAL64[149] decoupling pulses / kHz	70	83	70	70
^{13}C rf field for 90° and 180° pulses / kHz	-	-	-	70
Rotor synchronized delays for both echoes (τ_1 and τ_2) / ms	-	-	-	2.1(τ_1) 1.4(τ_2)
Δt_1 / us	-	-	-	14.3
Number of t_1 increments	-	-	-	655

[a] All recorded on a 9.4 T Bruker Avance III HD solid-state NMR spectrometer, using a 4 mm HXY probe in double resonance mode. The corresponding resonance frequencies of ^{1}H and ^{13}C are 400.1 MHz and 100.6 MHz, respectively.

3.4 Results and discussion

3.4.1 Comparison of the 1D ^{13}C CP spectra of MTO activated H-SSZ-13 and H-SAPO-34

Activated zeolites were prepared by flowing ^{13}C enriched CH_3OH on H-SSZ-13 and H-SAPO-34 catalyst beds at 275 °C for 25 min and 300 °C for 20 min, respectively, followed by quenching into liquid N_2 to capture the carbenium ion intermediates (full experimental details are given in section 3.3.1). The ^{13}C CP MAS NMR spectra of these two activated catalysts are given in Figure 3.2 and Figure 3.3, 3.4 for spectra at different MAS rates, and show multiple signals in the 0 - 260 ppm region, highlighting the complexity of the retained carbon species. Three general type of species (carbenium ions, aromatics/dienes, adamantane derivatives) are present, the downfield signals above 150 ppm being characteristic of carbenium ions.[67,88,95,106,148] It is worth pointing out that the ^{13}C spectra of activated H-SSZ-13 and H-SAPO-34 are very similar in this high frequency region; the two main peaks at about 153 and 243 ppm are representative signals for polymethylcyclopentenyl cations.[88,95,102,148] These 1D NMR spectra would suggest that the same cations are retained on these two zeolites with identical CHA topology, however the more informative 2D through-bond ^{13}C-^{13}C correlation NMR experiment[11] reveals that this is not the case (see below).

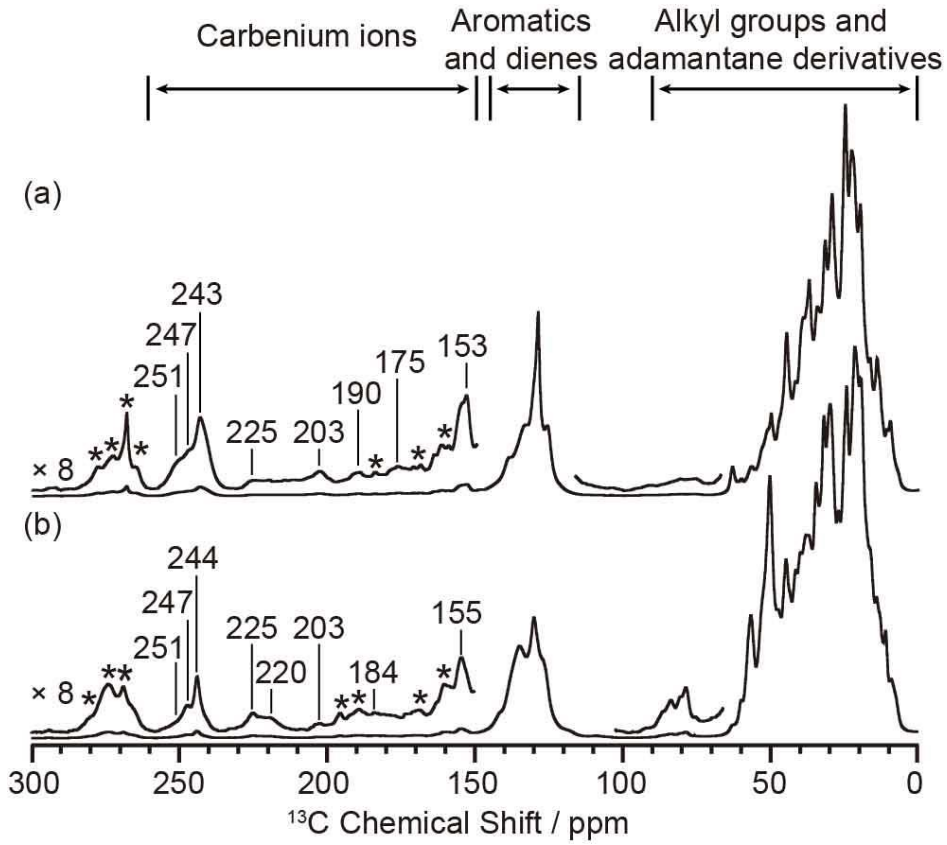

Figure 3.2 ^{13}C CP MAS spectra of activated (a) H-SSZ-13 and (b) H-SAPO-34. Spectra were recorded at 9.4 T and at a MAS of 14 kHz. Only characteristic signals for carbenium ions are labelled with chemical shifts. Asterisks (*) denote spinning sidebands.

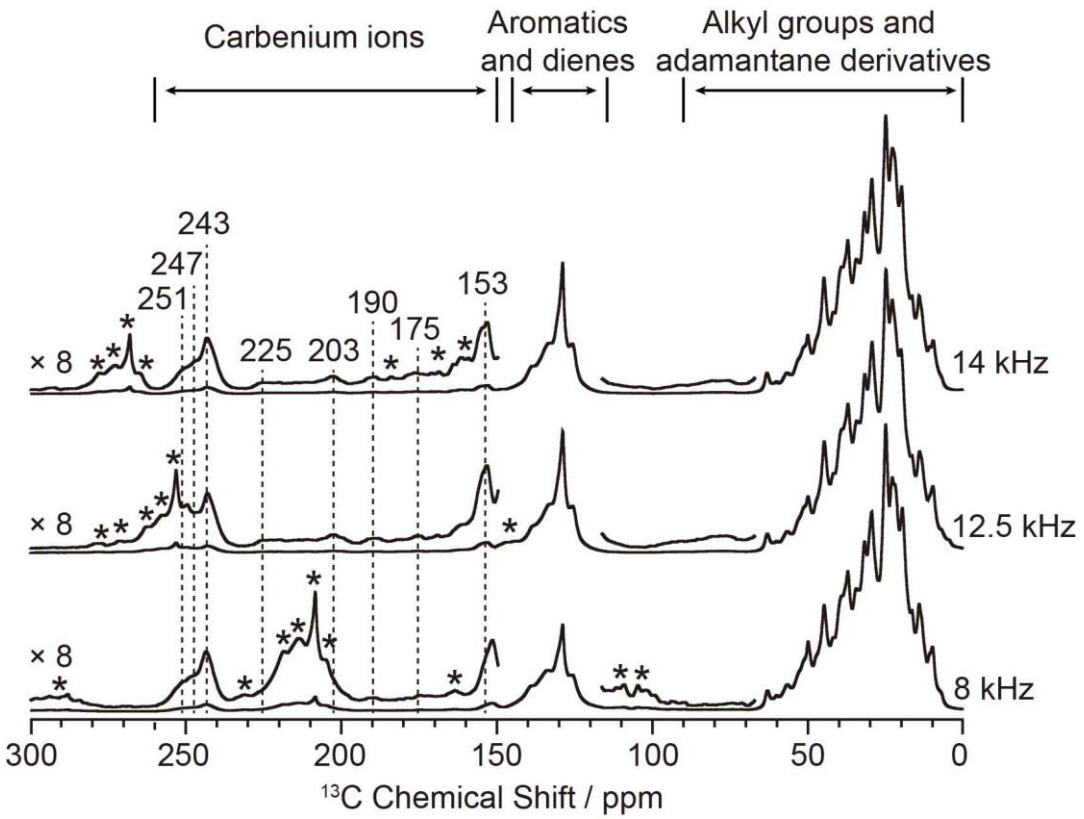

Figure 3.3 ^{13}C CP spectra of activated H-SSZ-13. Spectra were recorded at 9.4 T and at varied MAS rates of 8 kHz, 12.5 kHz and 14 kHz, respectively. Asterisks (*) denote spinning sidebands.

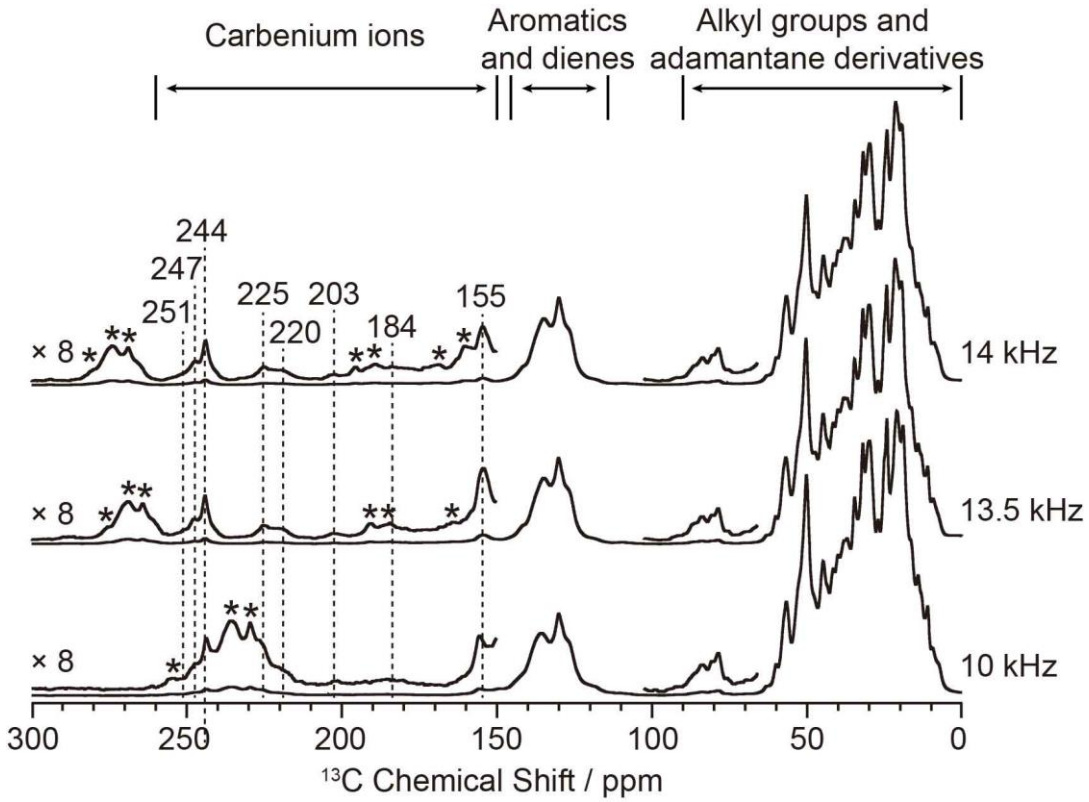

Figure 3.4 ^{13}C CP spectra of activated H-SAPO-34. Spectra were recorded at 9.4 T and at varied MAS rates of 10 kHz, 13.5 kHz and 14 kHz, respectively. Asterisks (*) denote spinning sidebands.

3.4.2 Structural identification of the confined carbon species in MTO activated H-SSZ-13 and H-SAPO-34

3.4.2.1 Different carbenium ions in H-SSZ-13 and H-SAPO-34 revealed by 2D ^{13}C-^{13}C INADEQUATE

The corresponding 2D ^{13}C-^{13}C refocused INADEQUATE spectra of both activated zeolites are shown in Figure 3.5 and 3.6. These experiments are based on through-bond scalar J coupling[11] (rather than through-space dipolar-based experiments)[13,14] and the correlation maps directly yield C-C bonds information, unambiguously enabling assignment of the carbon resonances. In this experiment, two peaks

resonating at the same frequency in the double quantum (vertical) dimension arise from the sum frequency of the two individual ^{13}C peaks in the single quantum (horizontal) dimension that correspond to chemically bonded carbons. The 2D spectra of the two activated zeolites show that the ^{13}C-^{13}C correlation maps are distinct as evidenced by correlations of the 63 and 243 ppm signals in H-SSZ-13 and of the 47 and 244 ppm peaks in H-SAPO-34 (see red and blue traces in Figure 3.5 and 3.6), demonstrating that the main carbenium ions formed are different in both zeolites with the same CHA topology. The full maps are also shown in the 2D spectra and reveal experimental observation of the characteristic correlations C1(**I**) (243 ppm) - C2(**I**) (153 ppm) and C2(**I**) (153 ppm) - C3(**I**) (251 ppm) identifying cation **I** as the main retained cation species in H-SSZ-13 (Figure 3.5) and C1,3(**II**) (244 ppm) - C2(**II**) (155 ppm) and C1,3(**II**) (244 ppm) - C4,5(**II**) (47 ppm) for cation **II** in H-SAPO-34 (Figure 3.6 and Figure 3.7, 3.8, 3.9 for complete set of correlations for each cation), allowing the structure of the carbenium ions and their ^{13}C chemical shifts to be explicitly obtained (Table 3.3).

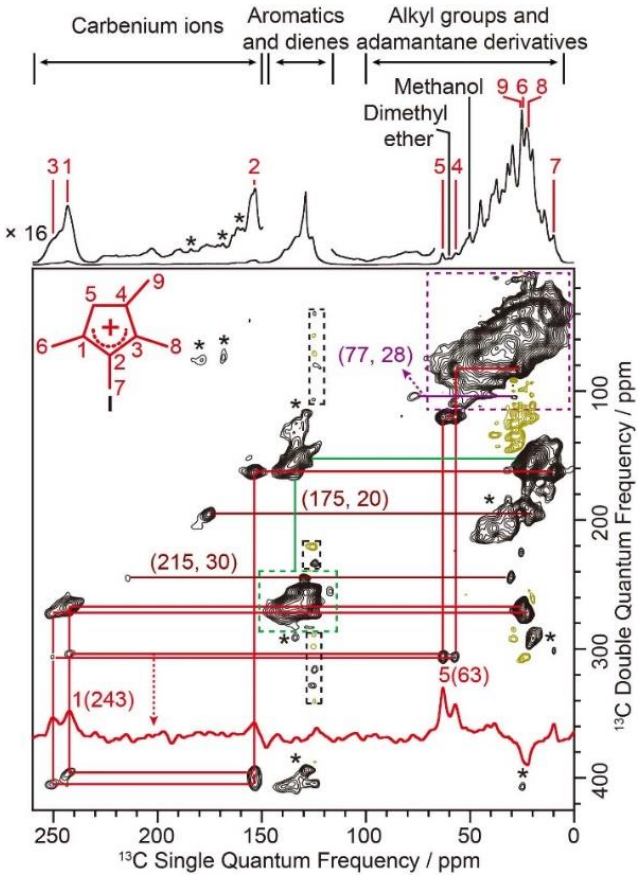

Figure 3.5 2D ^{13}C–^{13}C refocused INADEQUATE spectra of activated H-SSZ-13. Data were recorded at 9.4 T and at a MAS rate of 14 kHz. Signals of positive intensities and Fourier Transform (FT) wiggles of negative intensities are coded in black and olive, respectively. Asterisks (*) denote spinning sidebands. The assignments of the different carbenium ions and their corresponding structures are colored-coded. Some representative traces extracted along the horizontal dimension are also shown. The complete set of traces for carbenium ions **I** is given in Figure 3.7. Partial correlations for other carbenium ions are coded in maroon. The correlations coded in green and purple belong to the neutral species (aromatics, dienes and adamantane derivatives). Signals off the carrier frequency in black dashed box correspond to small artefacts caused by direct current (DC) offset. Numbers in parenthesis are the chemical shifts of the correlated ^{13}C sites.

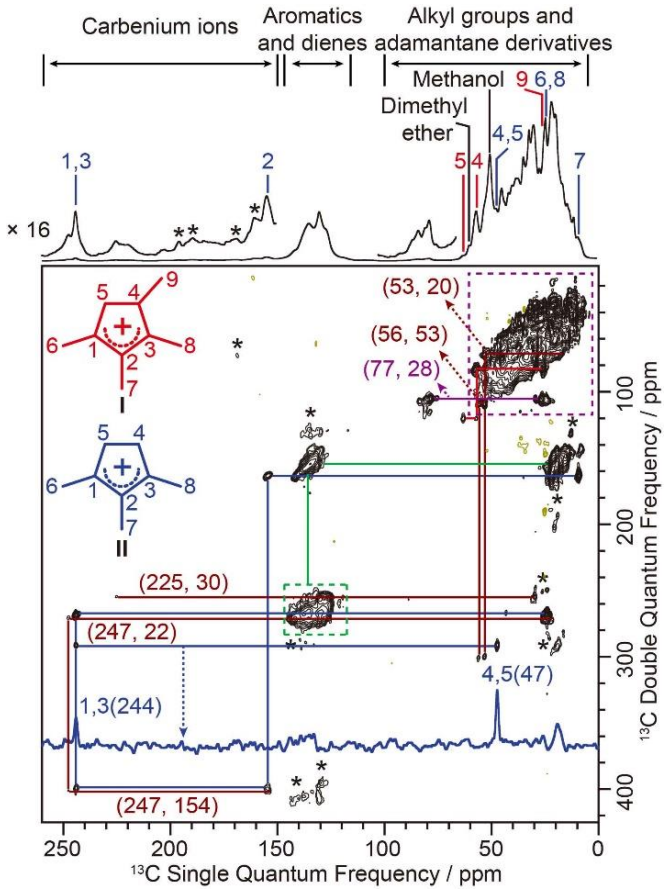

Figure 3.6 2D ^{13}C–^{13}C refocused INADEQUATE spectra of activated H-SAPO-34. Data were recorded at 9.4 T and at a MAS rate of 14 kHz. Signals of positive intensities and Fourier Transform (FT) wiggles of negative intensities are coded in black and olive, respectively. Asterisks (*) denote spinning sidebands. The assignments of the different carbenium ions and their corresponding structures are colored-coded. Some representative traces extracted along the horizontal dimension are also shown. The complete set of traces for carbenium ions **I** and **II** is given in Figure 3.8 and 3.9. Partial correlations for other carbenium ions are coded in maroon. The correlations coded in green and purple belong to the neutral species (aromatics, dienes and adamantane derivatives). Signals off the carrier frequency in black dashed box correspond to small artefacts caused by direct current (DC) offset. Numbers in parenthesis are the chemical shifts of the correlated ^{13}C sites.

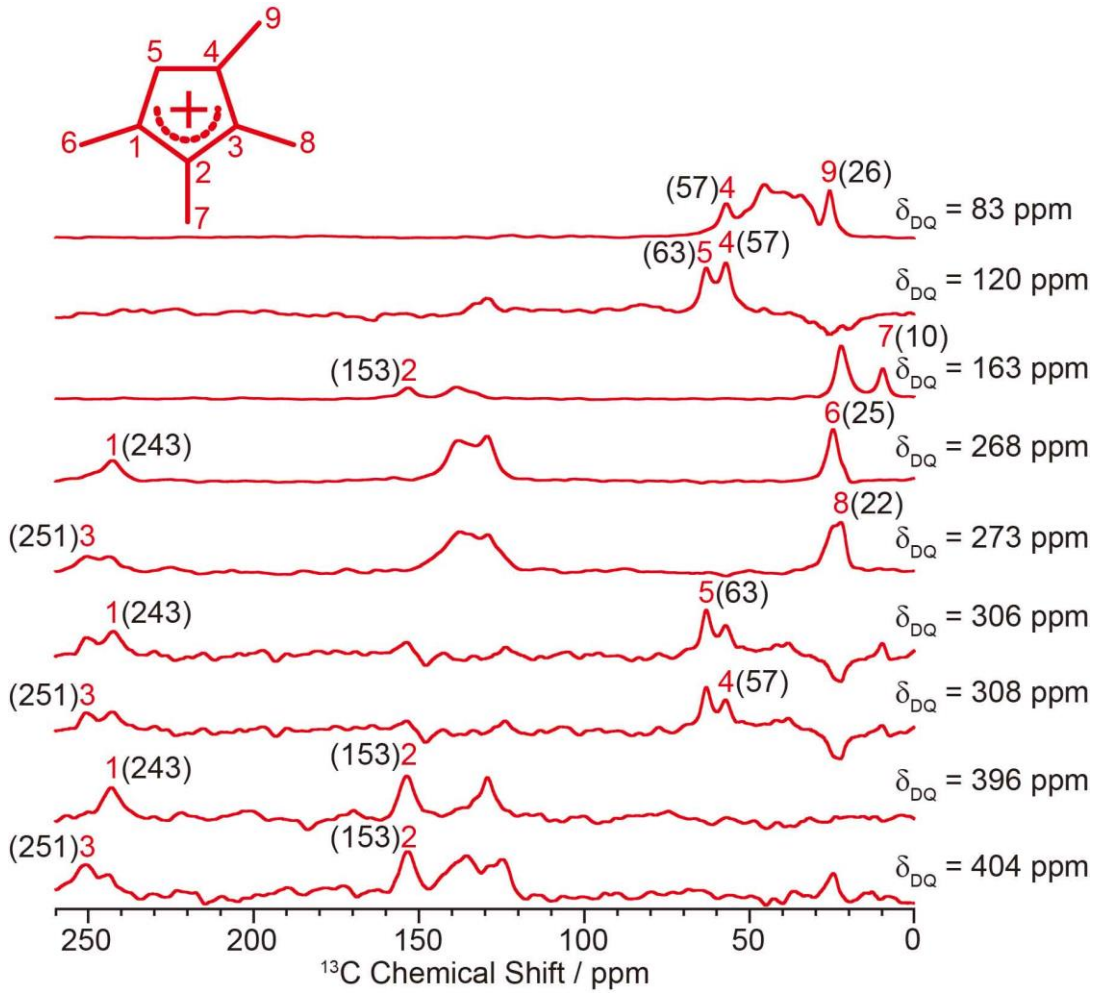

Figure 3.7 Horizontal traces for 1,2,3,4-tetramethylcyclopentenyl cation **I** in activated H-SSZ-13. The corresponding double quantum frequency δ_{DQ} of each slice is given in the figure. The chemical shifts of different ^{13}C sites are given in the parenthesis. Unlabeled peaks are from other carbenium ions or aromatic species.

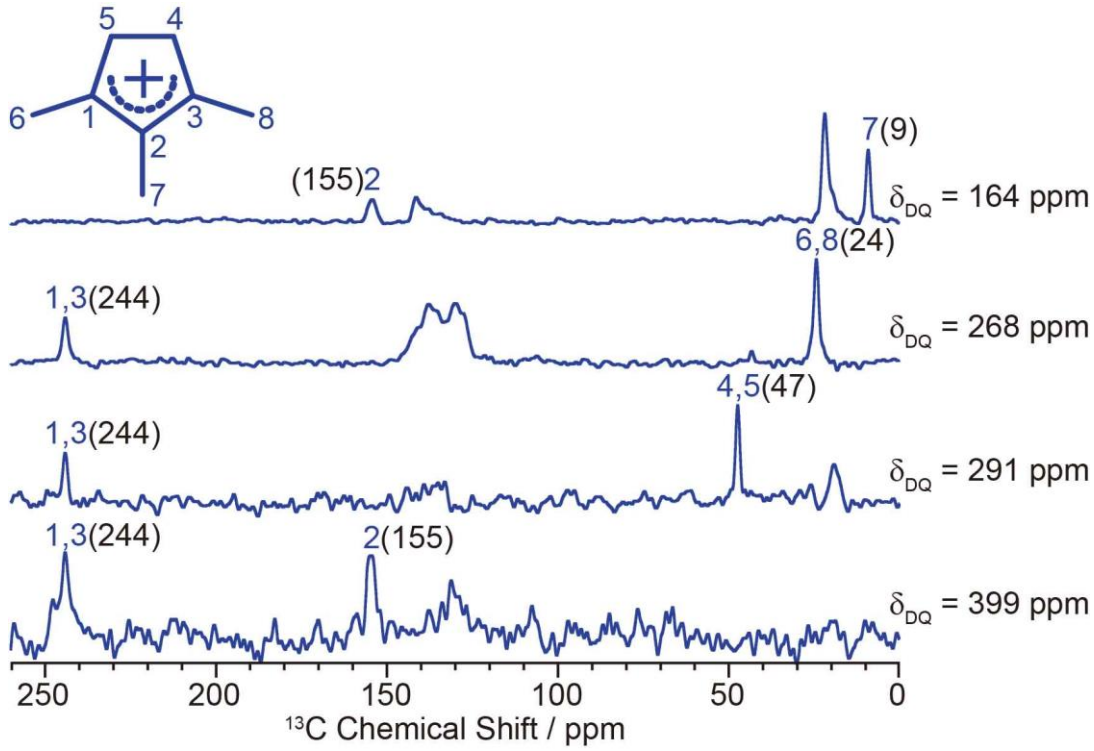

Figure 3.8 Horizontal traces for 1,2,3-trimethylcyclopentenyl cation **II** in activated H-SAPO-34. The corresponding double quantum frequency δ_{DQ} of each slice is given in the figure. The chemical shifts of different ^{13}C sites are given in the parenthesis. Unlabeled peaks are from other carbenium ions or aromatic species.

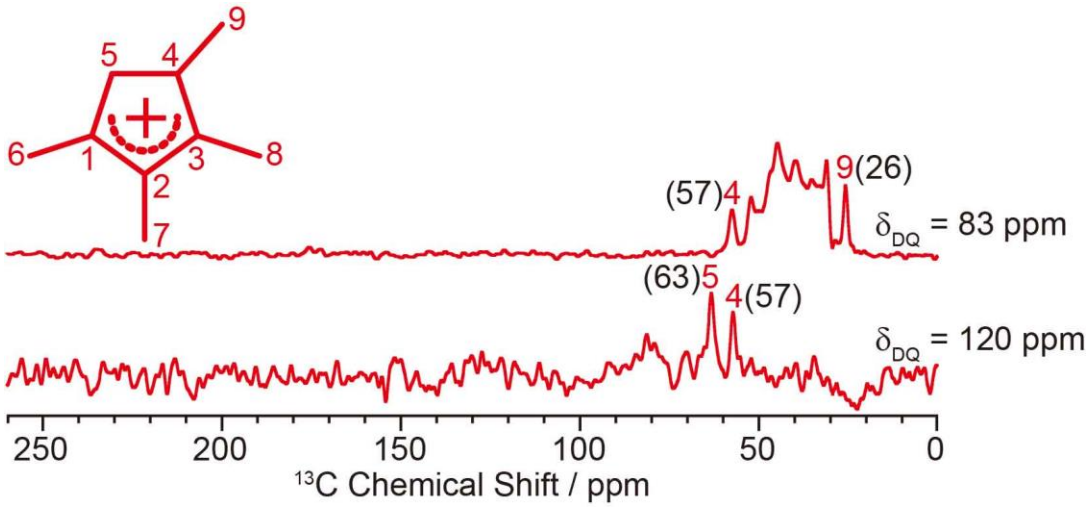

Figure 3.9 Horizontal traces for 1,2,3,4-tetramethylcyclopentenyl cation **I** in activated H-SAPO-34. The corresponding double quantum frequency δ_{DQ} of each slice is given in the figure. The chemical shifts of different ^{13}C sites are given in the parenthesis. Unlabeled peaks are from other carbenium ions or aromatic species.

Table 3.3 ^{13}C chemical shifts for carbenium ions I and II (structures are shown in Figure 3.5 and 3.6

Carbon number		C1	C2	C3	C4	C5	C6	C7	C8	C9
Chemical shift / ppm	**I**	243	153	251	57	63	25	10	22	26
	II	244	155	244	47	47	24	9	24	-[a]

a: not applicable.

Note that the tetramethyl substituted cyclopentenyl cation **I** has not been observed in the literature.[88,95,105,106,141,148] While trimethyl substituted cyclopentenyl **II** has been previously postulated in a previous study on H-SAPO-34[132] based solely on 1D ^{13}C spectra, it is worth pointing out that the 2D NMR method adopted here yields C-C bonding

information directly, providing straightforward structural identification not accessible using methods that require treatment of post-activated zeolites.[88,95,105,151]

Additional correlations involving ^{13}C signals in the high frequency range (175 to 250 ppm) are also observed (maroon lines in Figure 3.5 and 3.6). The correlations between signals at 30 - 215 ppm in H-SSZ-13 and 30 - 225 ppm in H-SAPO-34 are assigned to polymethylcyclohexenyl cations.[106,132,152] In H-SAPO-34, the 247 ppm resonance shows multiple correlations involving carbenium ions which are most likely other cyclopentenyl cations.[88,95,105] However, only a limited number of correlations is obtained, due to their low concentration as evidenced by their weak 1D signal intensities (Figure 3.2), and challenges a complete structural determination for these cations. In H-SSZ-13, there is a unique correlation between signals at 20 and 175 ppm and is characteristic of methylnaphthalenium cations,[67] the formation of this coke precursor being ascribed to the higher acid strength of H-SSZ-13 than H-SAPO-34 (as determined by infrared spectroscopy studies[146,153] and a combination of ^{1}H NMR, acetone probed ^{13}C NMR and NH_3-temperature programmed desorption methods).[88] The signals in the 190 - 203 ppm region in the 1D spectra of both zeolites (Figure 3.2, 3.3 and 3.4) arise from polymethylbenzenium cations[88] but are absent in the 2D spectra likely due to their very low concentration too.

Whilst CP MAS-based experiments like the refocused INADEQUATE are inherently not quantitative, the similar natures of the carbenium ions stabilized permit some consideration regarding the main species present. It is found that **I** dominates the 2D spectrum in H-SSZ-13 while it is a minor retained cation

species in H-SAPO-34 where **II** is the main cation. Note that only a few characteristic correlations corresponding to **I** has been detected in the later zeolite (*e.g.*, C4(**I**) - C5(**I**) and C4(**I**) - C9(**I**), as shown in Figure 3.6 and 3.9) as the others are likely beyond the detection limit of the 2D experiment. The difference in population of the main carbenium ions **I** and **II** present in these two zeolites probably arises from their different acid strengths. It is known that whether or not a carbenium ion could be persistently stabilized inside zeolites depends on its acid strength relative to that of the zeolites.[75,77,87,88] The distribution of carbenium ions in H-SSZ-13 *vs.* H-SAPO-34 may suggest that **I** is less stable than **II** and requires stronger acid sites to be stabilized.

The observation of the five-membered ring cations **I** and **II** is also strong indication of the existence of paring route in zeolites of CHA topology. It is clear that the five-membered ring cations are the main retained carbenium ion intermediates in both H-SSZ-13 and H-SAPO-34, while the six-membered ring cations are only present as minor species. This result is consistent with previous observation[88] showing that six-membered ring cations have higher activity and further transform and are therefore less likely to be observed than the five-membered ring cations in the CHA zeolites.

3.4.2.2 Neutral carbon species in MTO activated H-SSZ-13 and H-SAPO-34

In addition to carbenium species, neutral aromatics and dienes are present (correlated signals in the 115 - 150 ppm and 10 - 25 ppm regions, green dashed boxes and lines in Figure 3.5 and 3.6) and are involved as HCP species in the catalytic cycles and precursors of carbenium ions, respectively.[132] Correlations in the 10 - 50 ppm region (purple dashed boxes in Figure 3.5 and 3.6) are assigned to alkyl groups

(in aromatics and carbenium ions) and methyladamantanes, the later being consistent with GC-MS experiments performed on CHA zeolites and suggested as coke species leading to catalyst deactivation.[154] A correlation between signals at 77 and 28 ppm (purple lines in Figure 3.5 and 3.6) is also obtained on both zeolites and likely arises from hydroxy and methoxy substituted adamantanes.[155] Note that the poor resolution of the 2D spectra in these regions hinders complete assignments of the neutral species mentioned above. Finally, signals at 50 and 60 ppm do not display 2D correlations which is consistent with their assignments to strongly adsorbed methanol and dimethyl ether, respectively.[95,106]

3.5 Conclusions

In conclusion, we have explicitly obtained the molecular structures of the reactive carbenium ions in two zeolites with identical CHA topology using multidimensional through-bond NMR experiments. New types of polymethylcyclopentenyl cations are identified and may serve as crucial intermediates in the paring route for MTO reaction. The new cations identified here offer a more comprehensive understanding of the reaction routes and will inspire future research on their roles in MTO processes.

Chapter 4: Fast Detection and Structural Identification of Carbocations on Zeolites by Dynamic Nuclear Polarization Enhanced Solid-State NMR

This chapter is adapted from a paper titled of the same name that was published in *Chemical Science* in 2018,[67] for which the authors contribution are as follow: D. X. and F. B. designed the project, conducted the DNP experiments, analyzed the data and wrote the manuscript with inputs from all co-authors. S. X. prepared the activated zeolites, contributed to the DNP experiments and data analysis. N. B., S. P. and F. A. aided in carrying out the DNP experiments. F. A. performed the EPR spin counting experiments. L. C. and B. S. prepared the MMM-β zeolite. All authors discussed the results.

4.1 Abstract

Acidic zeolites are porous aluminosilicates used in a wide range of industrial processes such as adsorption and catalysis. The formation of carbocation intermediates plays a key role in reactivity, selectivity and deactivation in heterogeneous catalytic processes. However, the observation and determination of carbocations remain a significant challenge in heterogeneous catalysis due to the lack of selective techniques of sufficient sensitivity to detect their low concentrations. Here, we combine ^{13}C isotopic enrichment and efficient dynamic nuclear polarization magic angle spinning nuclear magnetic resonance spectroscopy to detect carbocations in zeolites. We use 2D ^{13}C–^{13}C through-bond correlations to establish their structures and ^{29}Si–^{13}C through-space experiments to quantitatively probe the interaction between multiple surface sites of the zeolites and the confined

hydrocarbon pool species. We show that a range of various membered ring carbocations are intermediates in the methanol to hydrocarbons reaction catalysed by different microstructural β-zeolites and highlight that different reaction routes for the formation of both targeted hydrocarbon products and coke exist. These species have strong van der Waals interaction with the zeolite framework demonstrating that their accumulation in the channels of the zeolites leads to deactivation. These results enable understanding of deactivation pathways and open up opportunities for the design of catalysts with improved performances.

4.2 Introduction

Carbocations are important intermediates in many homogeneous[71,80] and heterogeneous reactions,[73,76,78,79] especially those catalysed by solid acids (*e.g.* acidic zeolites),[74,77,81] and are formed from the corresponding hydrocarbons through protonation by the acidic protons of the Brønsted acid sites. They take part in a range of industrial processes such as cracking, isomerization, alkylation, *etc.*, which account for the conversion of hydrocarbons to a range of products.[77] For example, cyclic carbocations are proposed as important intermediates involved in the hydrocarbon pool mechanism for the conversion of methanol to hydrocarbons (MTH).[81,88,92–96,156,157] Despite the significant roles of carbocations in heterogeneous reactions, their identifications in solid catalysts are not straightforward as they are reactive, transient, difficult to capture and exist in generally low concentrations,[73,75,88,89,104]

and therefore their spectroscopic characterization is very challenging.[88–90,104]

Solid-state NMR is useful in detecting reactive carbocations on solid catalysts as shown in some limited cases on zeolites where their capture is achieved by quenching the reaction with liquid N_2[88,102] or stabilizing the intermediates with base (*e.g.* ammonia).[89] However, further development in extending the use of solid-state NMR to the study of carbocations is currently hindered by both the challenge associated with capturing enough highly reactive carbocations formed on solids (*vide supra*) and the intrinsically low sensitivity of NMR, especially when low natural abundance nuclei (*e.g.* 1.1% for ^{13}C) are targeted. Although ^{13}C isotopically enriched reagents are generally used to overcome this inherently poor sensitivity,[88,102,104] the small amount of carbocations that can be captured in successful cases (typically 0.01 $mmol \cdot g^{-1}$ in the MTH activated β-zeolite[104]) usually only permit the acquisition of 1D NMR signals, limiting the application of more informative multidimensional NMR experiments to obtain both the structures of these carbocations and their interaction with the solid catalysts. The structures of adsorbed carbocations are typically derived from such 1D ^{13}C NMR spectra combined with GC-MS and DFT calculations[88,95] and therefore prior assumption of the existing structures is required.

In chapter 2 we identified the carbocations formed in ^{13}C enriched MTH activated ZSM-5 and investigated their host-guest interaction by obtaining limited structural constraints.[106] However, the experimental times needed to acquire the multidimensional and multinuclear NMR

data were prohibitively long (> 5 days), even in this favourable case where the carbocation concentration is relatively high (> 0.02 mmol·g^{-1}). This significantly hinders the systematic use of these powerful approaches on a wider range of solid acids with a lower amount of carbocation intermediates and addressing this challenge necessitates further dramatic boost in NMR sensitivity beyond ^{13}C labelling.[90]

An emerging method with potential to delivering this increase in NMR sensitivity is DNP which can enhance the NMR signals by multiple orders of magnitude by transferring the large polarization of electrons to nearby nuclei *via* microwave induced electron-nuclear transitions, thereby leading to a very significant reduction in experimental time.[17–23] Insoluble samples for typical DNP experiments are impregnated with a solution of stable radicals as the source of electrons with the solvent providing the matrix for ^{1}H polarization transfer. Although initial work focused on water-soluble radicals[19,20] which are chemically incompatible with the investigation of carbocations, water free radicals and matrices are now known[34,42] and have enabled the structural characterization of a broad range of materials with DNP.[20] In particular in heterogeneous catalysis, this approach is starting to provide detailed access to catalytic sites on the surface or in the pores of selected catalysts,[18,27,37,45,48,52,60,61,66] including surface-enhanced NMR on mesoporous silica,[18] organometallics on silica,[52,66] Sn^{VI}-active sites in Sn-β zeolite[37,48,61] and Brønsted acid sites of aluminosilicate.[60] However, DNP investigation on reactive carbocation intermediates confined in microporous zeolites is yet to be demonstrated.

Here, we explore the use of DNP NMR to detect carbocations confined in porous zeolite catalysts during the MTH reaction.[95,104] We show that combining ^{13}C isotope enrichment and DNP enables the detection of low levels of carbocations (0.002-0.01 mmol·g^{-1}) in two types of β-zeolites within minutes. The considerable sensitivity increase obtained allows carbon connectivities to be obtained with ^{13}C-^{13}C through-bond experiments[11] yielding the molecular structures of a series of carbocations. The spatial proximities between the surface sites of the zeolites and the confined carbon species are quantitatively probed *via* ^{13}C-^{29}Si through-space NMR experiments.[16] The identification of these carbocations reveals possible reaction routes for the formation of olefins and coke species in the MTH reaction while the quantification of host-guest interaction indicates dominant interaction contributing to the adsorption of hydrocarbon pool species in zeolites. In addition, while DNP application has been shown to be limited for microporous zeolites,[37,61] here we suggest a potential way to optimize DNP efficiency on microporous zeolites, that is introducing hierarchical pores with different sizes ranging from micro (< 2 nm), meso (2–50 nm) to macro pores (> 50 nm).[158]

4.3 Experimental Procedures

4.3.1 Preparation of the activated zeolites

Two different β-zeolites with organic templates and different microstructures (microporous β-zeolite (M-β) and micro-meso-macroporous β-zeolite (MMM-β)[159]) were used. The β-zeolite has 12-ring window of 7.7 × 6.7

Å and 5.6 × 5.6 Å viewed along [100] and [001], respectively. The framework of β-zeolite and its micropore size are shown in Figure 4.1. The mesoporous and microporous structure of MMM-β was shown in ref[159]. The M-β zeolite templated with tetraethylammonium hydroxide was obtained from China University of Petroleum and has a Si/Al ratio of 13 (framework Si/Al ratio ≈ 24),[104] while MMM-β (framework Si/Al ratio ≈ 34, see Table 4.1, Figure 4.2) with tetraethylammonium hydroxide and glycerol templates was synthetized following a literature procedure.[159] Both zeolites were then calcined in air at 550 °C for 6 h to remove the templates, ion-exchanged in 1.0 M NH_4NO_3 aqueous solution at 80 °C three times and then subsequently recalcined at 550 °C for 4 h to yield the H-type zeolites. The zeolites were dehydrated at 500 °C under a continuous flow of He flow at 25 $mL \cdot min^{-1}$ for 2 h in a fixed-bed quartz tubular reactor followed by a decrease in temperature to the reaction temperature as follow. M-β was then reacted for 20 minutes (unless otherwise specified) with $^{13}CH_3OH$ (99 atom % ^{13}C, Sigma-Aldrich) with a WHSV of 2 h^{-1} at 275 °C while MMM-β was reacted for 20 minutes with either $^{13}CH_3OH$ at 300 °C or $^{13}C_2H_4$ (99 atom % ^{13}C, Sigma-Aldrich) at 275 °C with a WHSV of 2 h^{-1}. The reaction was then quenched by immersing the reactor into liquid N_2 and transferred to the N_2 glove box at room temperature where the samples were stored.

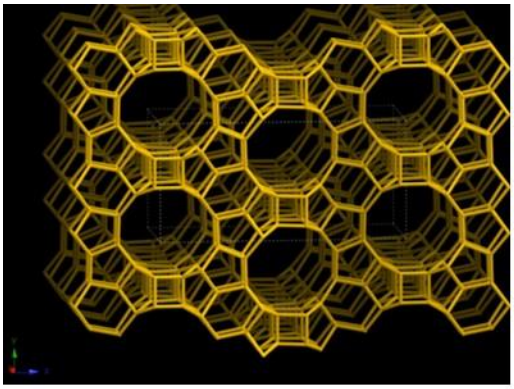

Framework viewed along [100]

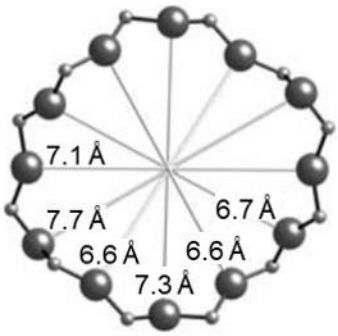

12-ring viewed along [100]

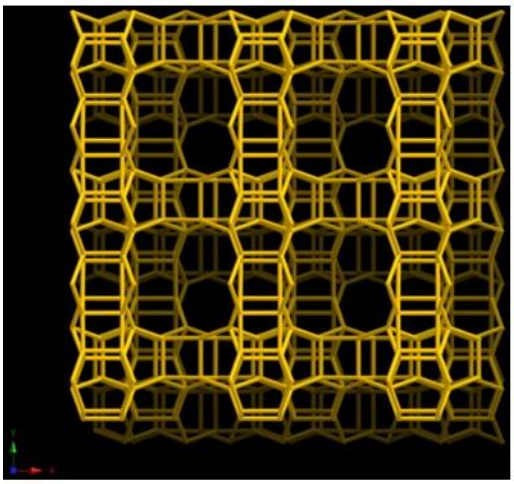

Framework viewed along [001]

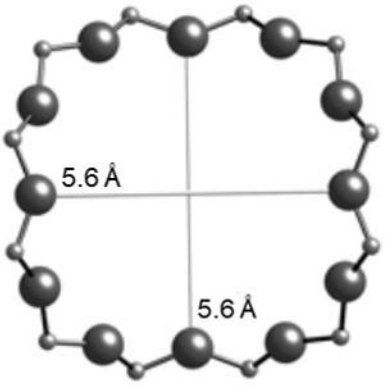

12-ring viewed along [001]

Figure 4.1 Framework of β-zeolite and its micropore size.[124,125] [100] and [001] denote crystallographic directions.

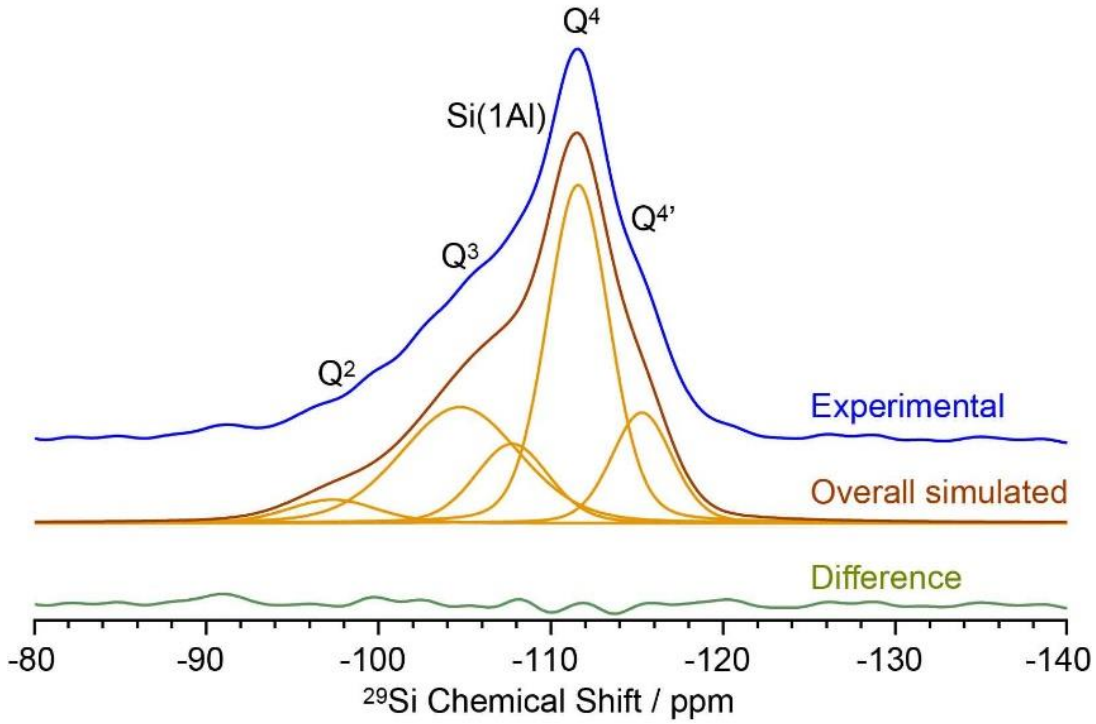

Figure 4.2 Quantitative room temperature ^{29}Si MAS NMR spectrum of H-type MMM-β at 9.4 T and a MAS rate of 10 kHz.

Table 4.1 Framework Si/Al ratios in H-type M-β and MMM-β zeolites determined from ^{29}Si MAS NMR spectra (Figure 4.2 for MMM-β)

Zeolite	Framework Si/Al
M-β	24[104]
MMM-β	34

The carbocation concentrations of activated M-β and activated MMM-β are in the order of 0.002 - 0.01 mmol/g based on the ^{13}C NMR spectra and previous work,[104] while the one of activated MMM-β is much lower.

4.3.2 Chemical compatibility between carbocations and TCE solvent

The activated zeolites (30 to 50 mg) were mixed with the halogenated solvent TCE (about 50 μL) by incipient wetness impregnation. Room temperature ^{13}C CP MAS spectra were recorded at 14.1 T before and after mixing with TCE.

4.3.3 Solid-state NMR experiments

NMR spectra were recorded on Bruker Avance III spectrometers (9.4 T and 14.1 T) using 4 mm HXY probes in double resonance mode.

^{13}C CP MAS experiments at 9.4 T were performed at a MAS rate of 12.5 kHz, while ^{29}Si CP MAS experiments were performed at a MAS rate of either 8 kHz (for M-β with template, MMM-β with template and activated M-β) or 10 kHz (for activated MMM-β). All ^{1}H pulses and SPINAL-64 heteronuclear decoupling[8] were performed at rf field amplitude of 83 kHz. ^{13}C CP MAS and ^{29}Si CP MAS experiments were obtained with a ^{13}C rf field of 51 kHz and a ^{29}Si rf field of 53 and 45 kHz at MAS rates of 8 and 10 kHz, respectively, while the ^{1}H rf field was ramped to obtain maximum signals at approximately 60 kHz.[150]

^{13}C CP MAS experiments at 14.1 T were performed at a MAS rate of 12 kHz. All ^{1}H pulses and SPINAL-64 heteronuclear decoupling were performed at a rf field of 54 kHz. ^{13}C CP MAS experiments were obtained with ^{13}C rf field of 79 kHz while the ^{1}H rf field was ramped at approximately 54 kHz.

The directly excited ^{29}Si MAS NMR spectrum of the H-type MMM-β zeolite was acquired at 9.4 T at a MAS rate of 10 kHz and with ^{1}H SPINAL-64 high-power decoupling[8] at a rf field of 83 kHz. ^{29}Si pulses were obtained with rf field

of 70 kHz. A recycle delay of 5 × T_1 = 65 s was used where T_1 is the ^{29}Si longitudinal relaxation time constant.

4.3.4 DNP MAS NMR experiments

Samples for DNP experiments were prepared by incipient wetness impregnation of the solids (typically 30 mg) with 40 μL of 20 mM of nitroxide biradicals TEKPol[34] in TCE[34,42] which is currently one of the most efficient polarizing matrix for cross-effect DNP at 9.4-14.1 T.[35,36] The freshly prepared mixtures were then packed into sapphire rotor which was then inserted into the pre-cooled DNP probe.

All DNP experiments were performed on a commercial 9.4 T Avance III DNP solid-state NMR spectrometer equipped with a 263 GHz gyrotron and on a 14.1 T Avance III DNP NMR spectrometer equipped with a 395 GHz gyrotron, using a low temperature 3.2 mm HXY probe in double or triple resonance mode. All the ^{13}C and ^{29}Si CP MAS experiments were performed with ^{1}H pulses and SPINAL-64 decoupling[8] at a rf field of 100 kHz and a recycle delay of 1.3 × $\tau_{DNP}(^{1}H)$ where $\tau_{DNP}(^{1}H)$ is the DNP build-up time. A ^{1}H pre-saturation block of 100 pulses separated by 1 ms was applied.

^{13}C and ^{29}Si CP MAS experiments at 9.4 T were performed at MAS rates of 12.5 and 8 kHz, respectively, and at T ≈ 110 K (calculated through T_1 of ^{79}Br in KBr[160] for which a very small amount was added to the rotor). The ^{13}C CP experiments were obtained with ^{13}C rf field at 62.5 kHz matched to a ramped ^{1}H rf field at approximately 100 kHz while ^{29}Si CP experiments were obtained with ^{29}Si rf field at 62.5 kHz matched to a ramped ^{1}H rf field at approximately 102 kHz. The rf field of the ^{13}C and ^{29}Si pulses was set to 62.5 kHz in the ^{13}C-

^{13}C z-filtered refocused INADEQUATE[11], ^{13}C-^{13}C PDSD[13,14,161], and $^{29}Si\{^{13}C\}$ REDOR[16] experiments (pulse programs are shown in Figure 4.3). The rotor synchronized τ delays in the INADEQUATE experiments were optimized to about 1.6 ms. The z-filter duration for activated M-β and MMM-β was 0.8 ms and 0.4 ms, respectively, during which ^{1}H CW decoupling at ^{1}H rf field of 12.5 kHz was used.[162] In the ^{13}C-^{13}C PDSD experiments, a 30 ms mixing time was used. DARR sequence was applied during the mixing period with ^{1}H rf field equal to MAS rate at 12.5 kHz. In the $^{29}Si\{^{13}C\}$ REDOR experiments, recoupling times up to 28.5 ms (for activated M-β) and 30 ms (for activated MMM-β were used. The experimental spectral lineshapes and dephasing curves from the REDOR experiments were simulated with the DMFIT[163] fitting software and using MatLab R2016a, respectively.

^{13}C CP MAS experiments at 14.1 T were performed at a MAS rate of 12.5 kHz and at T ≈ 125 K. The spectra were obtained with a ^{13}C rf field at 62 kHz matched to a ramped ^{1}H rf field at approximate 90 kHz.

4.3.5 EPR spin counting experiments

EPR experiments were recorded at room temperature on the DNP samples packed into 3.2 mm sapphire NMR rotors using an X-band Bruker Biospin EMX Nano spectrometer operating at X-band (9.6 GHz). The error on the EPR spin counting experiments was estimated to be about ±30%.[28,164] The concentration of electron spins in the DNP samples was also calculated based on the amount of zeolite and radical solution added. The error was estimated to be about ±75%, considering the evaporation of TCE solvent, error in radical concentration in solution, error in sample mass, etc.[165]

4.3.6 NMR pulse programs

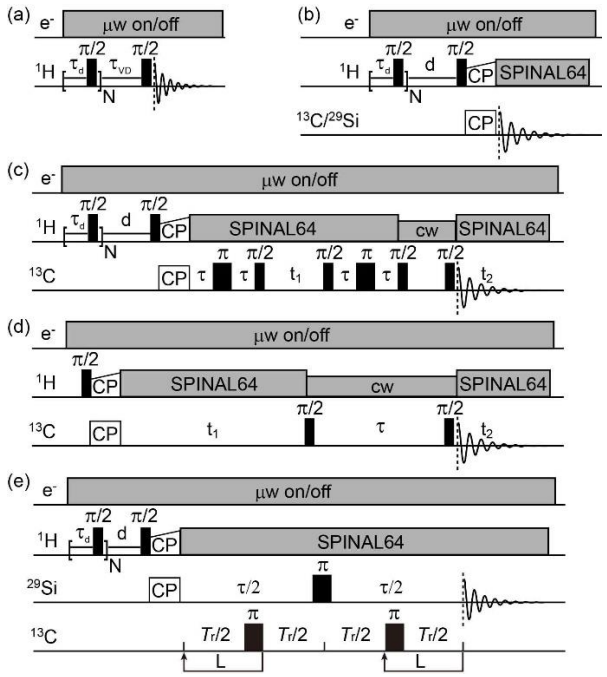

Figure 4.3 (a) ^{1}H saturation recovery pulse sequence to measure DNP polarization build-up time ($\tau_{DNP}(^{1}H)$) with μw on/off and ^{1}H longitudinal relaxation time constant (T_1) at room temperature. τ_{vd} is the variable delay list. (b) Pre-saturated CP pulse sequence. (c) Pre-saturated ^{13}C-^{13}C CP z-filtered refocused INADEQUATE pulse sequence. τ is synchronized to be an integer number of rotor periods.[11] (d) ^{13}C-^{13}C CP PDSD DARR pulse sequence with τ representing the mixing time.[13,14,161] (e) $^{29}Si\{^{13}C\}$ CP REDOR pulse sequence.[16] $T_r = 1/\nu_r$ is the rotor period, L is number of rotor periods and τ is the total recoupling time. In all the sequences, d is the recycle delay which is equal to 1.3 × $\tau_{DNP}(^{1}H)$. N = 100 is the number of ^{1}H saturation pulses with 1 ms delay τ_d between pulses. t_1 and t_2 correspond to indirect and direct dimension acquisition time, respectively. “CW” refers to continuous-wave.

4.3.7 Measurement of overall DNP sensitivity enhancement factor $\Sigma^{\dagger}$

The overall DNP sensitivity enhancement factor $\Sigma^{\dagger}$[36,43,166–172] takes into account the sensitivity improvement from low temperature thermal Boltzmann enhancement (DNP with μw on), signal attenuation due to the paramagnetic relaxation effects (bleaching) from the exogenous stable biradicals and cross-effect induced depolarization at MAS condition,[167–171] and time differences between the DNP enhanced NMR experiments and standard NMR experiments at room temperature. The following experiments are used to determine the factor $\Sigma^{\dagger}$:

(a) μw on DNP enhanced NMR at low temperature (approx. 110 K) of the zeolites impregnated by 20 mM of TEKPol[34] in TCE[34,42],

(b) μw off DNP NMR at low temperature (approx. 110 K) of the zeolites impregnated by 20 mM of TEKPol in TCE,

(c) Room temperature NMR of the neat zeolites,

(d) μw off DNP NMR at low temperature (approx. 110 K) of the zeolites impregnated with TCE and at the same field as in (a).

The equation to calculate $\Sigma^{\dagger}$ is as follows:

$$\Sigma^{\dagger} = \left(\frac{\Lambda_{RT}}{\Lambda_{DNP}}\right)\left(\frac{T_{RT}}{T_{DNP}}\right)\left(\frac{(S/N)_{DNP}\, m_{RT}}{(S/N)_{RT}\, m_{DNP}}\right)\sqrt{\frac{NS_{RT}\, T_{1,\,RT}}{NS_{DNP}\, \tau_{DNP}}}\,\theta \qquad \text{Equation 4.1}$$

where Λ, T, S/N, m, NS, $T_{1,\,RT}$, τ_{DNP} and θ are the full width at half maximum (FWHM), sample temperature, signal-to-noise ratio, mass of sample used, number of scans accumulated, ^{1}H longitudinal relaxation time constant at room temperature, DNP polarization build-up time and contribution factor,[169,171] respectively. The subscripts DNP and RT represent parameters taken from

experiments (a) and (c), respectively. The contribution factor is calculated as:

$$\theta = \frac{1}{\varepsilon}\left(\frac{(S/N)_{DNP}\, m_{LT}}{(S/N)_{LT}\, m_{DNP}}\right)\sqrt{\frac{NS_{LT}}{NS_{DNP}}} \qquad \text{Equation 4.2}$$

where ε is the DNP signal enhancement between (a) and (b), $(S/N)_{LT}$, m_{LT}, and NS_{LT} are signal-to-noise ratio, mass of sample and number of scans accumulated for (d), respectively.

In this paper, $\Sigma^{\dagger}$ values were calculated for M-β and MMM-β with templates and activated M-β and MMM-β: DNP NMR data recorded at 9.4 T or 14.1 T using 3.2 mm rotors *vs*. 9.4 T room temperature NMR data using 4 mm rotors which perhaps is the most commonly used solid-state NMR configuration.

4.3.8 Process for extraction the ^{29}Si-^{13}C dipolar couplings from the ^{29}Si{^{13}C} REDOR data

The vertical error bars in the ^{29}Si{^{13}C} REDOR curves have been derived from both the signal-to-noise ratios of the experimentally obtained S_0 and S' spectra, and error analysis in the fit of all experimental ^{29}Si lineshapes. The signal-to-noise ratios were calculated from the Topspin 3.2 software while the error analysis was extracted from the DMFIT fitting software.[163]

Fitting of the REDOR curves and calculation of dipolar coupling constants and internuclear distances refer to section 2.3.4.2.

4.4 Results and discussion

4.4.1 DNP efficiencies on zeolites

Two different β-zeolites with different microstructures (microporous β-zeolite (M-β) and micro-meso-macroporous β-zeolite (MMM-β)[159]) were used in this study. The DNP efficiencies on these zeolites were initially explored on the pristine zeolites with organic templates. While moderate enhancements were only observed for M-β ($\varepsilon_{C\ CP}$ = 14, $\varepsilon_{Si\ CP}$ = 14), much larger enhancements of 54 on ^{13}C CP and 72 on ^{29}Si CP signals were obtained on MMM-β (Figure 4.4, 4.5), clearly showing the positive effects of introducing hierarchical porosities into zeolites. A more representative parameter to evaluate the DNP efficiency as compared with standard NMR at room temperature is the overall DNP gain $\Sigma^{\dagger}$ (see calculation details in the section 4.3.7). This takes into account the increase of sensitivity from thermal Boltzmann distribution going from 298 K to 110 K (temperature at which the 9.4 T DNP with μw on data were recorded), signal attenuation due to the paramagnetic relaxation effects (bleaching) from the exogenous stable biradicals and cross-effect induced depolarization at MAS condition.[36,43,166–172] $\Sigma^{\dagger}_{C\ CP}$ values of 25 and 53 for M-β and MMM-β and $\Sigma^{\dagger}_{Si\ CP}$ values of 34 and 97 for M-β and MMM-β, respectively, were obtained at 9.4 T (Tables 4.2, 4.3 and Figure 4.4, 4.5). These large DNP gains $\Sigma^{\dagger}$ are clearly reflected in Figure 4.5 by the much larger signal-to-noise ratios obtained from the μw on DNP ^{29}Si

spectra (recorded in seconds) *vs.* the room temperature ^{29}Si MAS NMR spectra (acquired in tens of minutes).

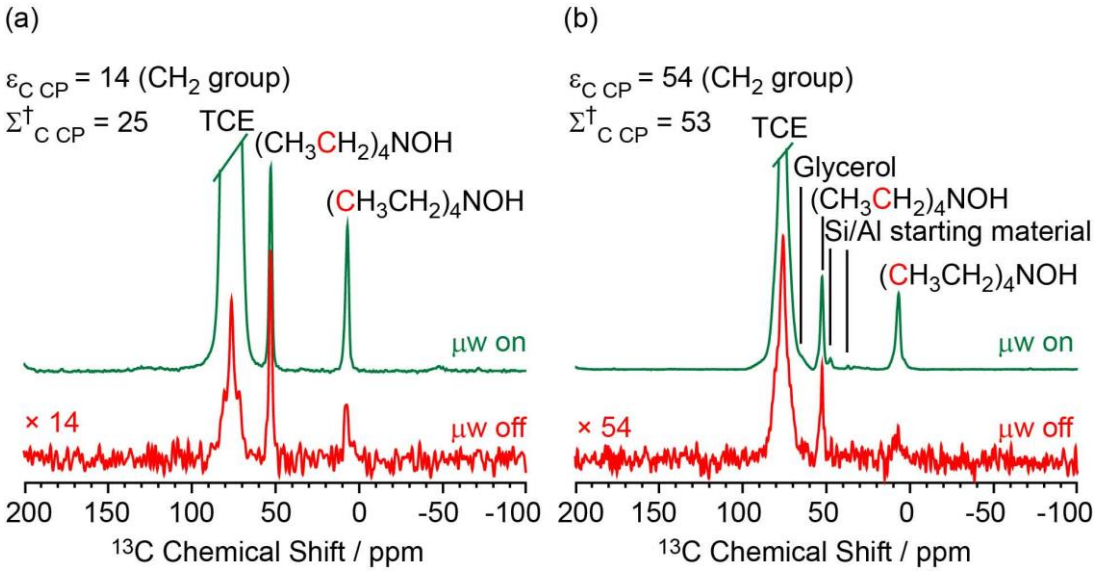

Figure 4.4 ^{13}C CP MAS DNP spectra of templated (a) M-β and (b) MMM-β with (μw on) (green) and without (μw off) microwave irradiation (red) at 9.4 T. TCE stands for 1,1,2,2-tetrachloroethane (solvent of impregnation).

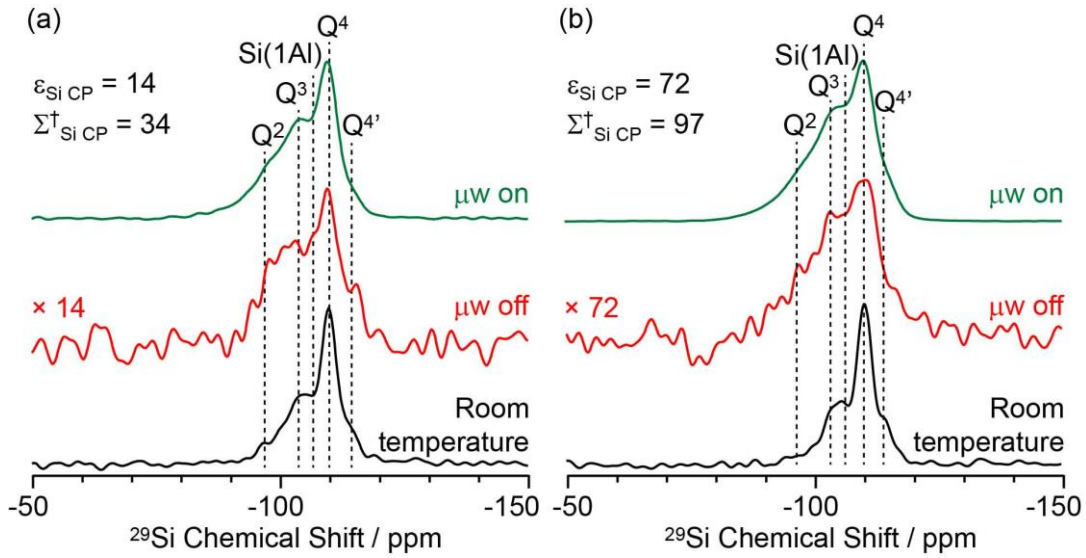

Figure 4.5 ^{29}Si CP MAS DNP spectra of (a) M-β with template and (b) MMM-β with template, with microwave irradiation (μw on) (green) and without (μw off) (red) recorded at 110 K. The sample was impregnated with 20 mM TEKPol in TCE. The black spectrum shows the ^{29}Si CP MAS spectrum at room temperature (without adding the radical solution). The experimental times for the μw on/off and room temperature spectra are 45 seconds and 26 minutes for M-β, and 166 seconds and 13 minutes for MMM-β respectively. All spectra were recorded at 9.4 T and with a MAS rate of 8 kHz.

Table 4.2 Enhancement factors $\Sigma^{\dagger}_{C\ CP}$ and $\Sigma^{\dagger}_{Si\ CP}$ calculation parameters for M-β with template

	$\Sigma^{\dagger}_{C\ CP}$			$\Sigma^{\dagger}_{Si\ CP}$		
Matrix	20 mM TEKPol[34] in TCE	TCE	None	20 mM TEKPol in TCE	TCE	None
Field / T	9.4	9.4	9.4	9.4	9.4	9.4
ε	14	-	-	14	-	-
Λ / Hz	210[a]	-	100[a]	420	-	360
T / K	110[b]	-	298	110[b]	-	298
(S/N) / a.u.	208	37	41	129	28	38
m / mg	23	24	89	23	24	89
NS	32	64	1024	16	64	512
τ_{DNP} / s	2.1	-	-	2.1	-	-
T_1 / s	-	-	0.17[c]	-	-	0.17[d]
θ	0.6	-	-	0.7	-	-
$\Sigma^{\dagger}$	25	-	-	34	-	-

[a] Signal of CH_2 group of $(CH_3CH_2)_4NOH$. [b] Calculated through T_1 of ^{79}Br in KBr added to rotor.[160] [c] A longer recycle delay of 3 s (instead of 1.3 × T_1) was used to record the CP experiments as to ensure an adequate duty cycle for the probe.

Table 4.3 Enhancement factors $\Sigma^{\dagger}_{C\ CP}$ and $\Sigma^{\dagger}_{Si\ CP}$ calculation parameters for MMM-β with template

	$\Sigma^{\dagger}_{C\ CP}$			$\Sigma^{\dagger}_{Si\ CP}$		
Matrix	20 mM TEKPol in TCE	TCE	None	20 mM TEKPol in TCE	TCE	None
Field / T	9.4	9.4	9.4	9.4	9.4	9.4
ε	54	-	-	72	-	-
Λ / Hz	210[a]	-	70[a]	500	-	320
T / K	110[b]	-	298	110[b]	-	298
(S/N) / a.u.	364	18	35	670	19	45
m / mg	12	13	60	12	13	60
NS	64	128	512	64	64	256
τ_{DNP} / s	2.0	-	-	2.0	-	-
T_1 / s	-	-	0.92[c]	-	-	0.92[c]
θ	0.6	-	-	0.5	-	-
$\Sigma^{\dagger}$	53	-	-	97	-	-

[a] Signal of CH_2 group of $(CH_3CH_2)_4NOH$. [b] Calculated through T_1 of ^{79}Br in KBr added to rotor.[160] [c] A longer recycle delay of 3 s (instead of 1.3 × T_1) was used to record the CP experiments as to ensure an adequate duty cycle for the probe.

The effects of paramagnetic centres on the NMR signals can be evaluated by the contribution factor θ and the increase of the NMR signal full width at half maximum (FWHM). The contribution factor θ corrects for

the loss of signals by paramagnetic bleaching such that signals from nuclei close to the paramagnetic centres are removed beyond detection limits and by depolarization induced by the cross-effect under MAS conditions.[167–171] A high contribution factor of 0.7 was obtained on the ^{29}Si NMR signals for M-β (see Table 4.2) while θ decreased to 0.5 for MMM-β (Table 4.3), suggesting less overall signal loss in M-β than in MMM-β. The paramagnetic effect will also cause additional line-broadening of the NMR signals if the radicals are in proximity to the observe nuclei due to the faster nuclear transverse relaxations (T_2') induced by the radicals.[43,44,173] Figure 4.6 and Figure 4.7 compare the ^{13}C CP MAS NMR spectra of both M-β and MMM-β zeolites, respectively, in the presence and absence of radicals and no obvious change on FWHM is observed (as monitored by the CH_2 resonance of the $(CH_3CH_2)_4NOH$ template). However, significant line broadening is observed when the zeolite is frozen in TCE at low temperature with the FWHM of the CH_2 increasing from 100 Hz at room temperature to 210 Hz at 110 K (for M-β) and from 70 to 210 Hz (for MMM-β). This large line-broadening is attributed to the molecules being trapped in a variety of conformations by the low temperature and frozen solvent, leading to large inhomogeneous broadening (as generally observed in proteins).[44,166,174] In this work, this broadening does not prevent the ^{13}C resonances of the organic templates from being fully resolved.

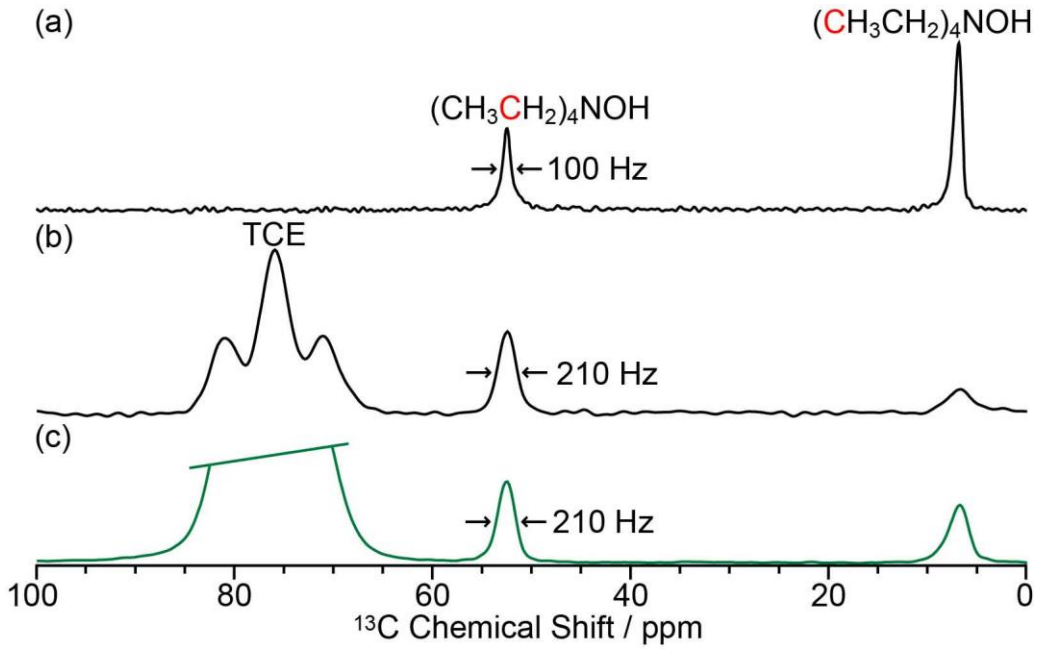

Figure 4.6 ^{13}C CP MAS spectra of M-β with template. (a) Spectrum of the neat zeolite at room temperature. (b) Spectrum of the zeolite impregnated with TCE at 110 K. (c) DNP μw on spectrum of the zeolite impregnated with 20 mM TEKPol in TCE at 110 K. All spectra were recorded at 9.4 T and with a MAS rate of 12.5 kHz.

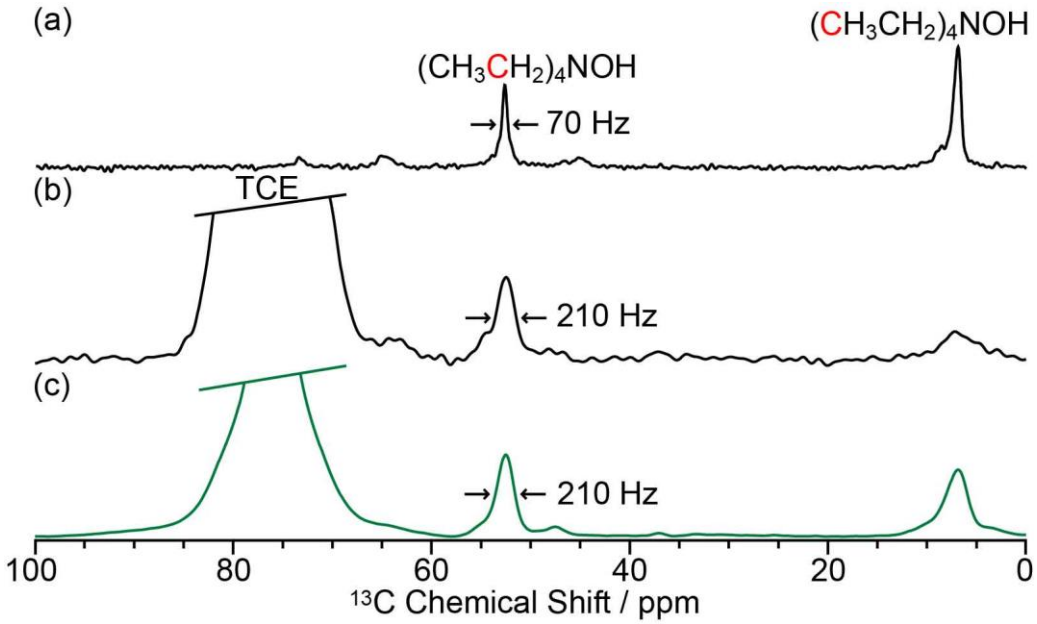

Figure 4.7 ^{13}C CP MAS spectra of MMM-β with template. (a) Spectrum of the neat zeolite at room temperature. (b) Spectrum of the zeolite impregnated with TCE at 110 K. (c) DNP μw on spectrum of the zeolite impregnated with 20 mM TEKPol in TCE at 110 K. All spectra were recorded at 9.4 T and with a MAS rate of 12.5 kHz.

The larger DNP enhancements in MMM-β *vs*. M-β can be attributed to the facilitated diffusion of both the large TEKPol radical ($d_{TEKPol} \approx 2$ nm, with *d* referring to length of molecule in a DFT optimized structure[66]) and TCE solvent which is improved by the existence of uniform mesopores and macropores in MMM-β (mesopore and macropore sizes of 2.5-4.0 and 100-300 nm,[159] respectively). Since the spin polarization transfer relies on the ^{1}H solvent spin diffusion, more efficient polarization transfer in MMM-β is expected, which translates to larger enhancements. Additionally, a larger amount of radical solution is needed to wet the MMM-β zeolite which leads to higher electron spin concentration as

confirmed by electron paramagnetic resonance (EPR) spin counting experiments (Table 4.4).

Table 4.4 Concentration of electron spins in the DNP samples

Sample	Electron spin concentration measured by EPR spin counting (mmol/g)[a]	Electron spin concentration calculated from preparation procedure (mmol/g)[b]
M-β with template	$(2.7 \pm 0.8) \times 10^{-2}$	$(2.2 \pm 1.7) \times 10^{-2}$
Activated M-β	$(1.1 \pm 0.3) \times 10^{-2}$	$(2.4 \pm 1.8) \times 10^{-2}$
MMM-β with template	$(7.4 \pm 2.2) \times 10^{-2}$	$(3.3 \pm 2.5) \times 10^{-2}$
Activated MMM-β	$(7.3 \pm 2.2) \times 10^{-2}$	$(3.3 \pm 2.5) \times 10^{-2}$

[a] EPR spin counting measurements were performed on samples after DNP experiments. [b] The electron spin concentrations were obtained based on the amount of zeolite and radical solution added.

4.4.2 Fast detection of carbocations with DNP

The activated M-β was prepared by reacting M-β with $^{13}CH_3OH$ (see section 4.3.1 for experimental details). Both $^{13}CH_3OH$ and $^{13}C_2H_4$ were initially used to activate MMM-β; however the $^{13}C_2H_4$ activated MMM-β shows much stronger carbocation signals (Figure 4.8) and was therefore used in this work (unless otherwise specified). The chemical compatibility between the reactive cations, TCE and TEKPol solutions was investigated on these activated zeolites prior to DNP experiments. The M-β and MMM-β activated zeolites were impregnated with TCE and the ^{13}C CP MAS spectra of both zeolites before and after impregnation with TCE are compared in Figure 4.9. The spectra show that, for both activated zeolites, the typical signals of carbocations (from 150 to 250

ppm), which structures identified in this work are shown in Figure 4.10, and of the aromatics (120 to 150 ppm) remain unchanged after impregnation with TCE, indicating that the carbocations are well stabilised by confinement in pores. Note also that EPR spin counting experiments on the activated zeolites impregnated with the TCE/TEKPol biradical solution quantify the electron spin concentrations added (Table 4.4) and illustrate the chemical compatibility of TCE/TEKPol with the carbocations and other carbon species formed in the activated zeolites. It is likely that the carbocations are mainly confined within the micropores of both β-zeolites (pore size < 1 nm), hence excluding, the possibility of these cations reacting with bulky TEKPol (whose size is larger than the pore size of the micropore of the β-zeolite). It was demonstrated previously that immobilizing the reactive surface species inside a mesoporous support like MCM-41 (pore size of 2.5-3.0 nm) separates them from TEKPol and eliminates possible reactions between them while the polarization is still relayed by ^{1}H spin diffusion of the solvent.[66] This phenomenon is also responsible for the transfer of DNP polarization in the micropores of Sn-β zeolite.[37,48,61]

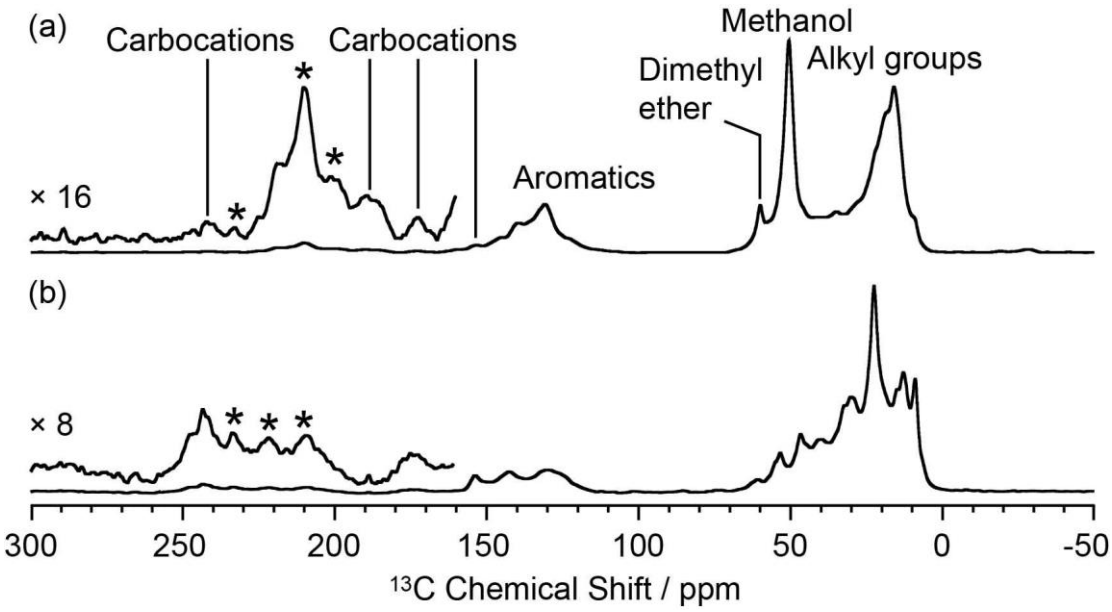

Figure 4.8 Room temperature ^{13}C CP MAS spectra of (a) MMM-β activated with $^{13}CH_3OH$ and (b) MMM-β activated with $^{13}C_2H_4$. Data were recorded at 14.1 T and with a MAS rate of 12 kHz. Asterisks (*) denote spinning sidebands.

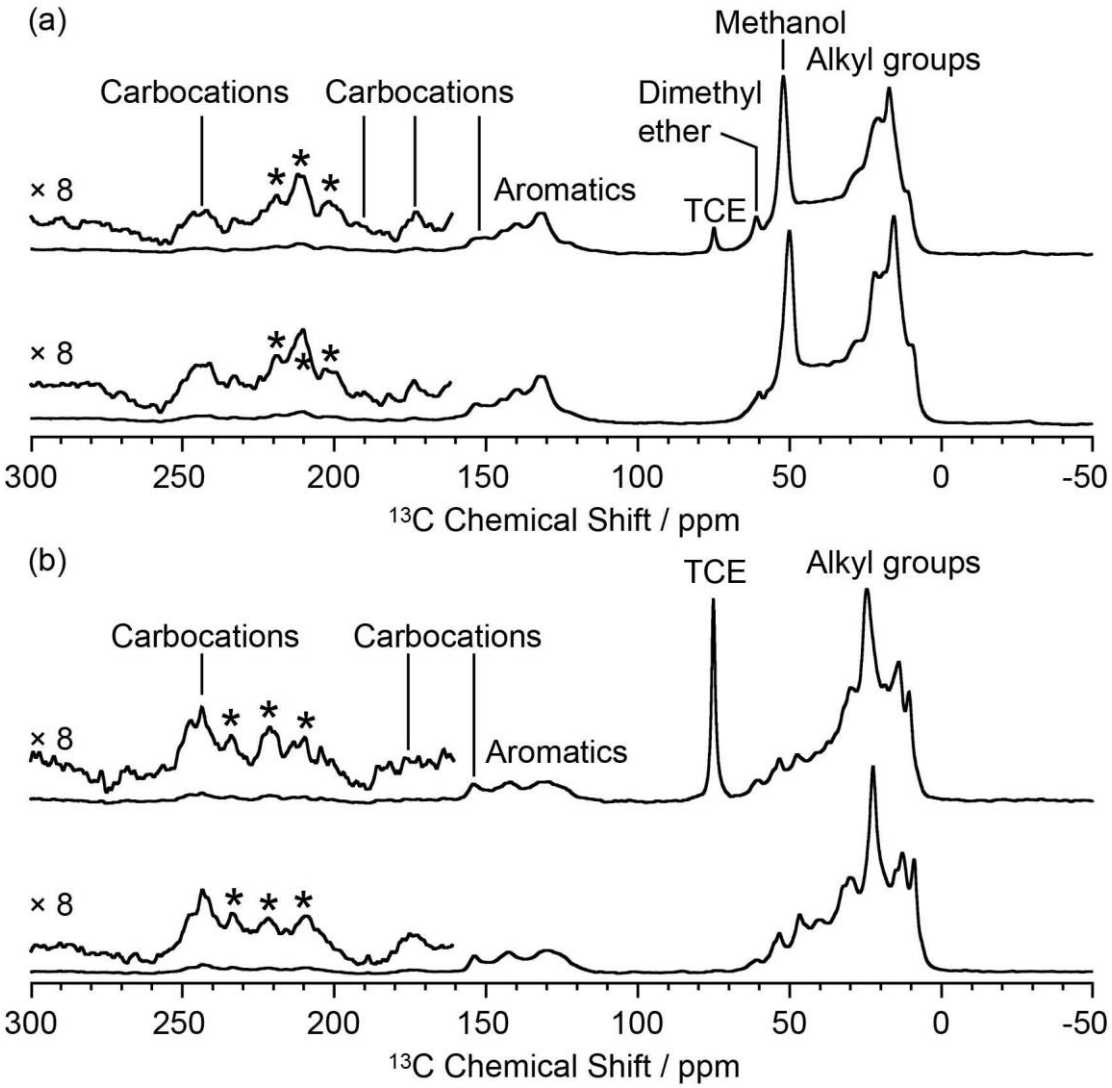

Figure 4.9 Room temperature ^{13}C CP MAS spectra of (a) activated M-β and (b) activated MMM-β. The upper and lower spectra were obtained on zeolites impregnated with TCE and neat, respectively. Data were recorded at 14.1 T and with a MAS rate of 12 kHz. Asterisks (*) denote spinning sidebands.

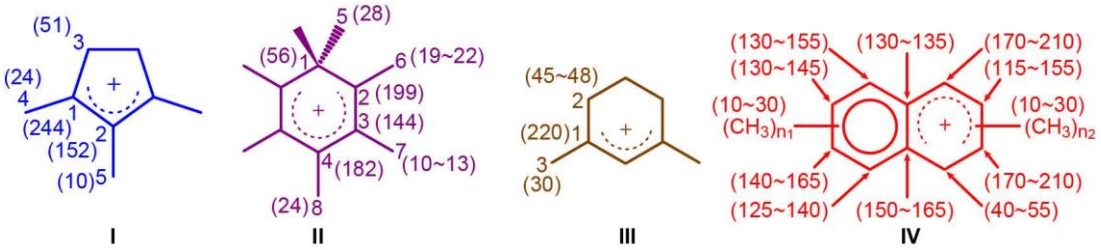

Figure 4.10 Carbocations identified in activated M-β and MMM-β (coded with the same colors as their corresponding assignments and correlations in Figure 4.11, 4.14 and 4.15. Values in the parenthesis are ^{13}C chemical shifts. n_1 and n_2 are the number of methyl groups with $3 \leq (n_1 + n_2) \leq 7$.

The DNP-enhanced ^{13}C CP MAS NMR spectra of the activated zeolites are shown in green in Figure 4.11 and reveal ^{13}C signal enhancements $\varepsilon_{C\ CP}$ of 10 and 40 at 9.4 T for M-β and MMM-β, respectively. Under microwave irradiation at 9.4 T, the carbocation signals (150 to 250 ppm) can be clearly observed within minutes (experimental times of ≈ 7 minutes for M-β and ≈ 2 minutes for MMM-β) while, importantly, no carbocation signals emerge without microwave irradiation (red spectra). Other signals at around 0 to 50 ppm can be assigned to alkanes or alkyl groups from both aromatics and carbocations, while the two additional peaks at 50 and 60 ppm in activated M-β (Figure 4.11(a)) correspond to methanol and dimethyl ether, respectively.[104] The strong peak arising from the TCE solvent is located at about 75 ppm and does not interfere with the NMR signals of the adsorbed species (black spectra). The ^{13}C signal enhancements above translate to overall DNP gains $\Sigma^{\dagger}_{C\ CP}$ of 30 and 161 for activated M-β (Table 4.5) and MMM-β (Table 4.6) zeolites, respectively. These gains correspond to a very significant reduction of experimental time

compared to the standard experiments at room temperature, showing substantial DNP efficiency. Note the much better DNP efficiency on activated MMM-β than on activated M-β which validates the use of hierarchical pores. DNP experiments at 14.1 T were also recorded on both activated zeolites. While the ^{13}C signal enhancements and DNP gains at 14.1 T are smaller than those at 9.4 T (Figure 4.11), as expected from the inverse field-dependence of the DNP enhancement with cross-effect DNP,[19,20] the carbocations can still be observed but no obvious increase in resolution is observed presumably due to strong inhomogeneous broadening and increase in chemical shift dispersion.

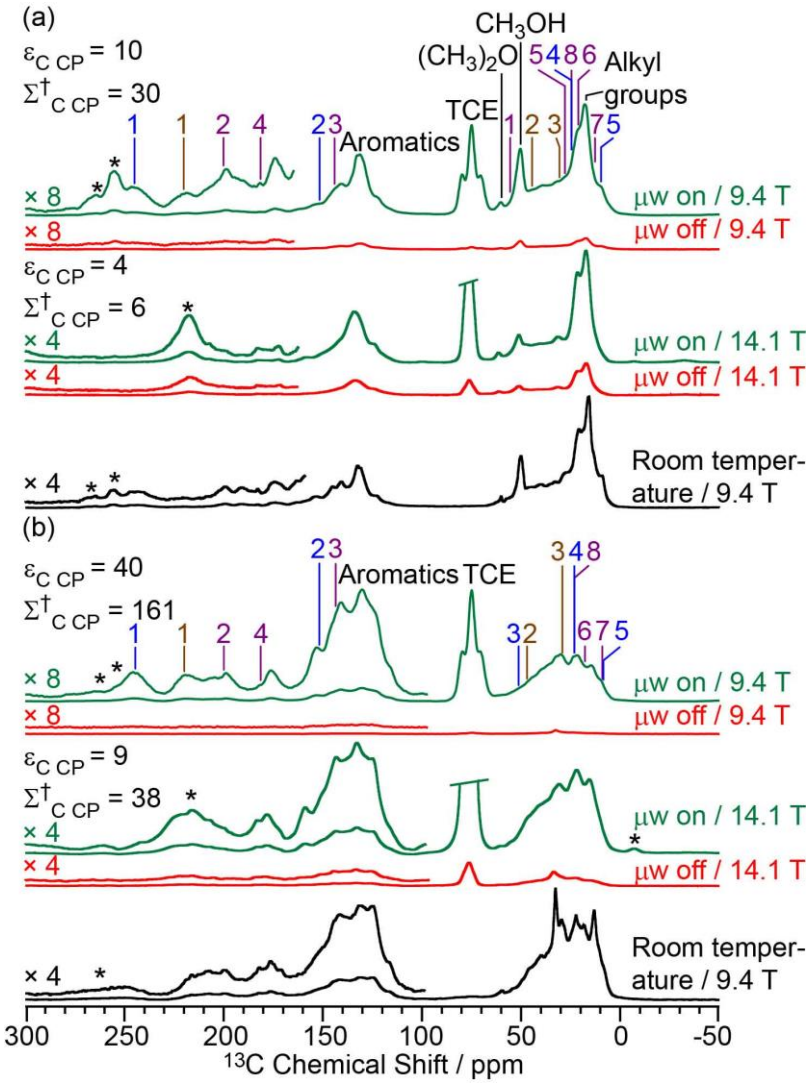

Figure 4.11 ^{13}C CP MAS DNP spectra at 9.4 T, 110 K and 14.1 T, 125 K and room temperature experiments at 9.4 T of (a) activated M-β and (b) activated MMM-β. The assignments of the different carbocations are given with the same colors as their structures in Figure 4.10 (except methylnaphthalenium ions **IV** which are omitted in these 1D spectra for clarity but shown in Figure 4.14 and 4.15). The experimental times for the spectra of activated M-β are ≈ 7 minutes at 9.4 T DNP, ≈ 9 minutes at 14.1 T DNP and ≈ 52 minutes at room temperature at 9.4 T without DNP while for activated MMM-β these are ≈ 2 minutes at 9.4 T DNP, ≈ 6 minutes at 14.1 T DNP and ≈ 1036 minutes at room

temperature at 9.4 T without DNP. $\Sigma^{\dagger}$ refers to the overall DNP gain and is calculated by comparing the DNP data to room temperature 9.4 T NMR spectra (see section 4.3.7). All spectra were recorded at MAS rate of 12.5 kHz with asterisks (*) denoting spinning sidebands.

Table 4.5 Enhancement factors $\Sigma^{\dagger}_{C\ CP}$ and $\Sigma^{\dagger}_{Si\ CP}$ calculation parameters for activated M-β

	$\Sigma^{\dagger}_{C\ CP}$					$\Sigma^{\dagger}_{Si\ CP}$		
Matrix	20 mM TEKPol in TCE		TCE		None	20 mM TEKPol in TCE	TCE	None
Field / T	9.4	14.1	9.4	14.1	9.4	9.4	9.4	9.4
ε	10	4	-	-	-	9	-	-
Λ / Hz	490[a]	900[a]	-	-	365[a]	520	-	400
T / K	110[b]	125[b]	-	-	298	110[b]	-	298
(S/N) / a.u.	851	274	192	217	242	273	50	108
m / mg	22	14	20	15	75	17	15	75
NS	32	32	128	160	1024	16	32	5656
τ_{DNP} / s	10.2	13	-	-	-	9.7	-	-
T_1 / s	-	-	-	-	0.74[c]	-	-	0.74[c]
θ	0.8	0.8	-	-	-	0.8	-	-
$\Sigma^{\dagger}$	30	6[d]	-	-	-	96	-	-

[a] Signal of methanol. [b] Calculated through T_1 of ^{79}Br in KBr added to rotor.[160] [c] A longer recycle delay of 2 s or 3 s (instead of 1.3 × T_1) was used to record the CP experiments as to ensure an adequate duty cycle for the probe. [d] Compared to the 9.4 T room temperature spectrum.

Table 4.6 Enhancement factors $\Sigma^{\dagger}_{C\ CP}$ and $\Sigma^{\dagger}_{Si\ CP}$ calculation parameters for activated MMM-β

	$\Sigma^{\dagger}_{C\ CP}$						$\Sigma^{\dagger}_{Si\ CP}$		
Matrix	20 mM TEKPol in TCE			TCE		None	20 mM TEKPol in TCE	TCE	None
Field / T	9.4[a]	9.4	14.1	9.4[a]	14.1	9.4	9.4	9.4	9.4
ε	34	40	9	-	-	-	45	-	-
Λ / Hz	2900[b]	2800[b]	4500[b]	-	-	3100[b]	500	-	570
T / K	110[c]	110[c]	125[c]	-	-	298	110[c]	-	298
(S/N) / a.u.	325	168	159	15	58	89	854	41	20
m / mg	13	11	13	15	14	53	13	15	53
NS	128	32	64	128	256	20480	64	128	1024
τ_{DNP} / s	4.2	2.9	4.3	-	-	-	4.2	-	-
T_1 / s	-	-	-	-	-	0.31[d]	-	-	0.31[d]
θ	0.7	0.7	0.7	-	-	-	0.8	-	-
$\Sigma^{\dagger}$	111	161	38[e]	-	-	-	462	-	-

[a] Used to calculate θ. [b] Signal of aromatic rings. [c] Calculated through T_1 of ^{79}Br in KBr added to rotor.[160] [d] A longer recycle delay of 2 s or 3 s (instead of 1.3 × T_1) was used to record the CP experiments as to ensure an adequate duty cycle for the probe. [e] Compared to the 9.4 T room temperature spectrum.

Large contribution factors (θ values ranging between 0.7 and 0.8) were obtained for the ^{13}C signals of activated M-β and MMM-β (Tables 4.5 and 4.6). These results indicate less signal loss by paramagnetic bleaching and depolarization in the two activated zeolites. The FWHM of

the CH_3OH signal in activated M-β was measured and used to monitor the changes of the ^{13}C lineshapes in the presence of TEKPol and TCE and at low temperatures. Figure 4.12 shows that adding TEKPol only increases the linewidth slightly by about 8% (from 455 to 490 Hz). However, a significant larger line broadening is observed when activated M-β is frozen at low temperatures with the FWHM of CH_3OH increasing by 25% (from 365 Hz at room temperature to 455 Hz at 110 K), resulting in a slight loss of resolution (*e.g.* the double peaks at 145 ppm and at 21 ppm are not resolved anymore, Figure 4.12). A similar observation is made in activated MMM-β (see Figure 4.13) with a clear loss of resolution of the signals arising from the alkyl groups. The results indicate inhomogeneous broadening due to molecules being trapped in a variety of conformations as the main contribution to the line-broadening, as on the zeolites with templates.[44,166,174]

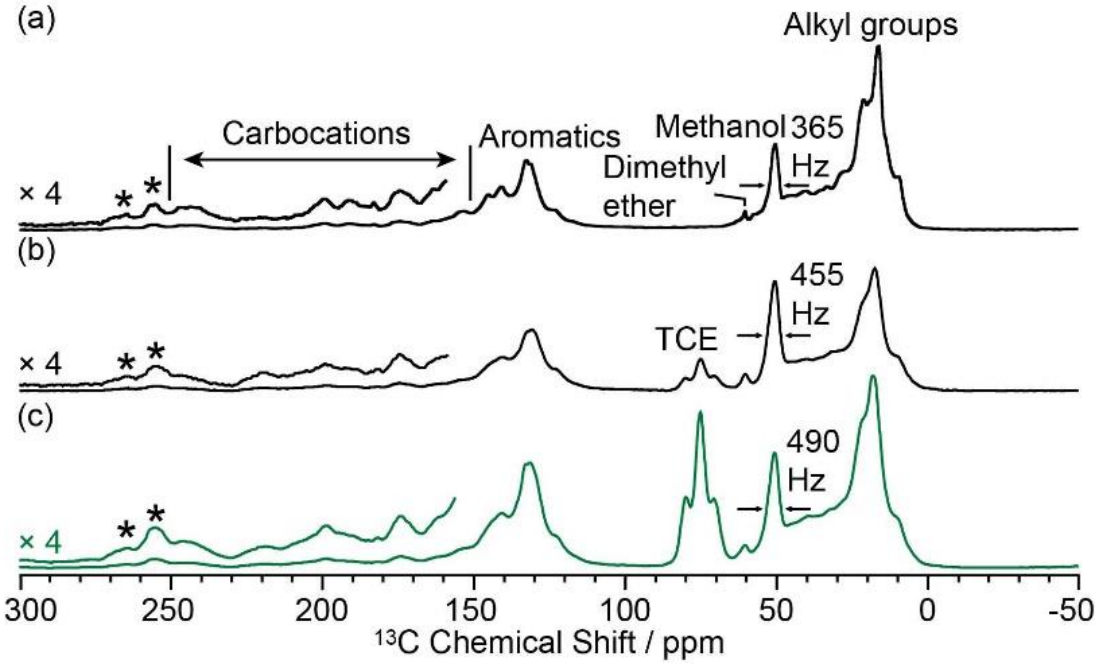

Figure 4.12 ^{13}C CP MAS spectra of activated M-β. (a) Spectrum of the neat activated zeolite at room temperature. (b) Spectrum of the activated zeolite impregnated with TCE at 110 K. (c) DNP μw on spectrum of the activated zeolite impregnated with 20 mM TEKPol in TCE at 110 K. All spectra were recorded at 9.4 T and with a MAS rate of 12.5 kHz. Asterisks (*) denote spinning sidebands.

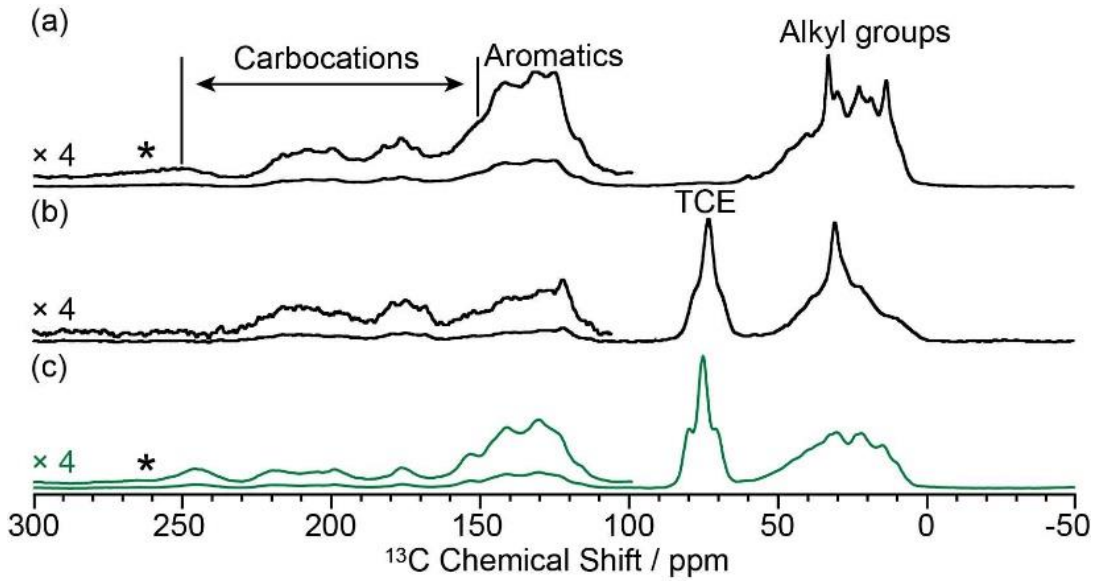

Figure 4.13 ^{13}C CP MAS spectra of activated MMM-β. (a) Spectrum of the neat activated zeolite at room temperature. (b) Spectrum of the activated zeolite impregnated with TCE at 110 K. (c) DNP μw on spectrum of the activated zeolite impregnated with 20 mM TEKPol in TCE at 110 K. All spectra were recorded at 9.4 T and with a MAS rate of 12.5 kHz. Asterisks (*) denote spinning sidebands.

4.4.3 Structure identification of the carbocations

To identify the molecular structures of the confined carbon species, 2D ^{13}C-^{13}C refocused INADEQUATE experiments,[11] based on scalar J couplings and providing ^{13}C-^{13}C through-bond correlations, were performed. Spectra are shown in Figure 4.14 (M-β) and 4.15 (MMM-β) : three single ring carbocations can be identified which are trimethylcyclopentenyl cation **I**, heptamethylbenzenium cation **II** and dimethylcyclohexenyl cation **III**, confirming the previously postulated structures.[95,104,132,175] More explicitly, the structure of **I** is obtained through the following correlations: C1(**I**) (244 ppm) – C2(**I**) (152 ppm),

C1(**I**) (244 ppm) – C3(**I**) (51 ppm), C1(**I**) (244 ppm) – C4(**I**) (24 ppm) and C2(**I**) (152 ppm) – C5(**I**) (10 ppm) (see captions of Figure 4.14 and 4.15 for the derivation of **II** and **III** from these data). Note that cation **I** was previously identified as intermediate over ZSM-5[95,106] and SAPO-34[132], but has only been postulated over β zeolites,[104] with the data presented here therefore confirming its presence. These five- and six-membered ring cations suggest that both the paring and side-chain catalytic cycles may exist in the β zeolite for the conversion of methanol to hydrocarbons, and the experimentally structural identification of these cations here provides more directly spectroscopic supports for the previously proposed mechanisms.[88,95,104,176]

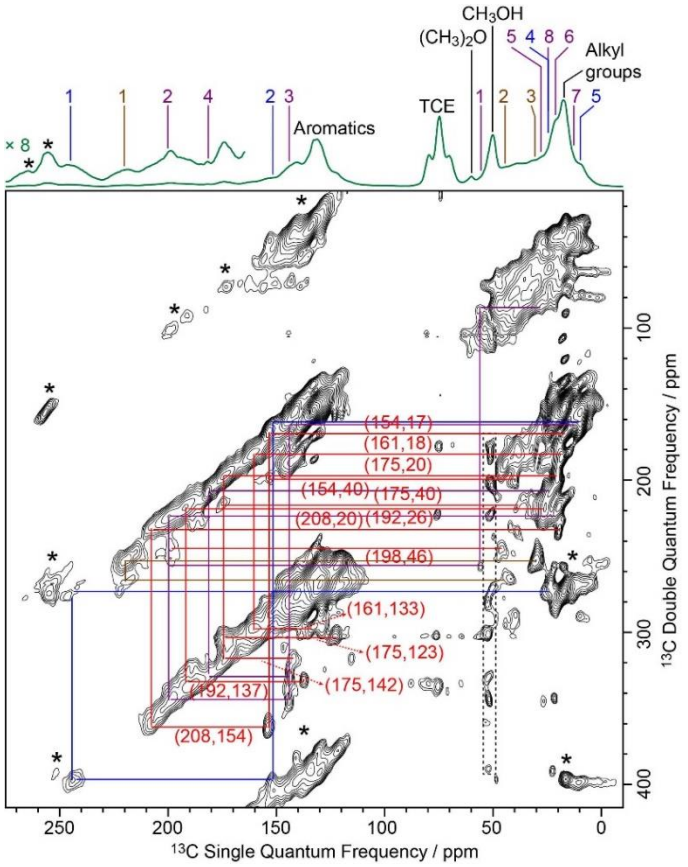

Figure 4.14 DNP enhanced 2D ^{13}C-^{13}C refocused INADEQUATE spectrum of activated M-β. Data was recorded at B_0 = 9.4 T and with a MAS frequency of ν_r = 12.5 kHz. The correlations and spectral assignments are coded with the same colors as their corresponding carbocations in Figure 4.10. Signals in the black dashed box correspond to t_1 noise. Correlations corresponding to naphthalenium ions (**IV**) are shown with the ^{13}C chemical shifts in the Single Quantum dimension of the two correlated carbon atoms given in the parenthesis. Correlations for cation **II** are C1(**II**) (56 ppm) – C2(**II**) (199 ppm), C1(**II**) (56 ppm) – C5(**II**) (28 ppm), C2(**II**) (199 ppm) – C3(**II**) (144 ppm), C2(**II**) (199 ppm) – C6(**II**) (22 ppm), C3(**II**) (144 ppm) – C4(**II**) (182 ppm), C3(**II**) (144 ppm) – C7(**II**) (13 ppm), C4(**II**) (182 ppm) – C8(**II**) (24 ppm), while for cation **III** are C1(**III**) (220 ppm) – C2(**III**) (45 ppm) and C1(**III**) (220 ppm) – C3(**III**) (30 ppm). Asterisks (*) denote spinning sidebands.

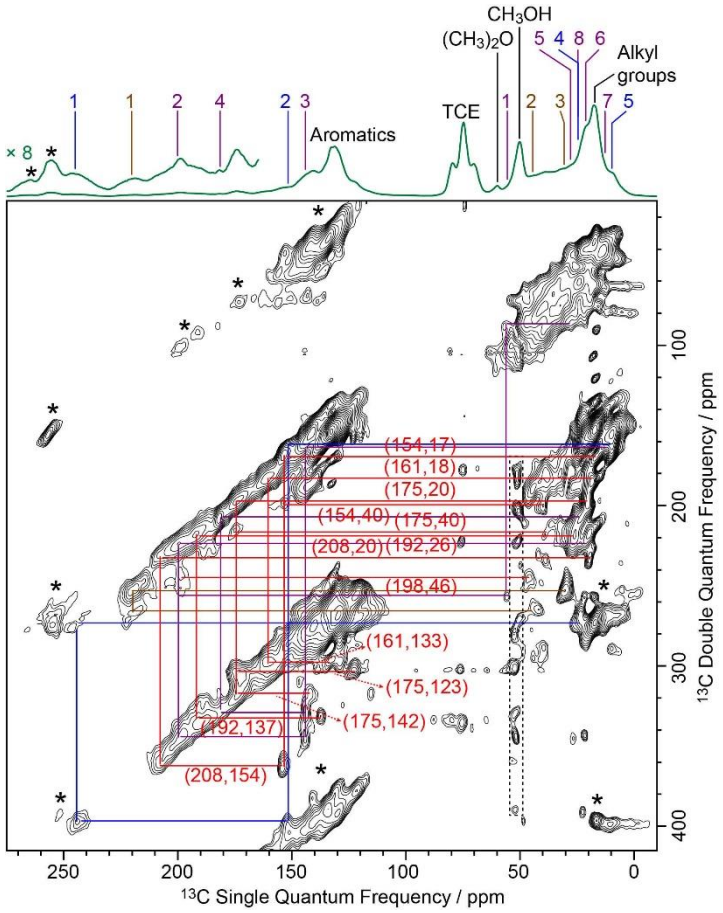

Figure 4.15 DNP enhanced 2D ^{13}C-^{13}C refocused INADEQUATE spectrum of activated MMM-β. Data was recorded at B_0 = 9.4 T and with a MAS frequency of ν_r = 12.5 kHz. The correlations and spectral assignments are coded with the same colors as their corresponding carbocations in Figure 4.10. Correlations corresponding to naphthalenium ions (**IV**) are shown with the ^{13}C chemical shifts in the Single Quantum dimension of the two correlated carbon atoms given in the parenthesis. Correlations for cation **II** are C2(**II**) (199 ppm) – C3(**II**) (144 ppm), C2(**II**) (199 ppm) – C6(**II**) (19 ppm), C3(**II**) (144 ppm) – C4(**II**) (182 ppm), C3(**II**) (144 ppm) – C7(**II**) (10 ppm), C4(**II**) (182 ppm) – C8(**II**) (24 ppm), while for cation **III** are C1(**III**) (220 ppm) – C2(**III**) (48 ppm) and C1(**III**) (220 ppm) – C3(**III**) (30 ppm). Asterisks (*) denote spinning sidebands.

Neutral methylnaphthalenes have been identified by GC-MS as part of the hydrocarbon pool species in the β zeolite,[104,176,177] however observation of their active cationic counterparts (methylnaphthalenium ions) and determination of those cations' structures have only been elusive so far even when ^{13}C solid-state NMR was previously deployed.[88,95,104] The extra sensitivity obtained with DNP permits the detection of additional ^{13}C correlations (shown in red) involving lower field signals at 208 and 176 ppm to be also resolved (Figure 4.14 and 4.15). These characteristic peaks have been observed in previous liquid-state ^{13}C NMR studies of methylnaphthalenium ions bearing up to four methyl substituents and are obtained by protonation of methylnaphthalenes by magic acids.[178,179]

The DNP enhanced 2D ^{13}C-^{13}C NMR correlation experiments provide direct support for identifying the structure of these methylnaphthalenium ions. Characteristic correlations in the single quantum (horizontal) dimension at, for example, 208–154 ppm and 176–131 ppm are assigned to ring carbons while those at 208–21, 176–20 ppm correspond to bonds between ring carbons and methyl substituents, and enable methylnaphthalenium ions with structures **IV** to be proposed (Figure 4.10). The range of connectivities shown in Figure 4.14 and 4.15 demonstrates that more than one methylnapthalenium ion is present and highlights the actual complexity of these species in activated zeolites.

These results confirmed previous computational[180] and UV−vis spectroscopy[181] studies that postulated the presence of methylnaphthalenium ions and methylnaphthalenes. This is also in

agreement with previous GC-MS data which suggest that methylnaphthalenes with 3 to 7 methyl groups exist in the β zeolite.[176,177] These species can act as both active hydrocarbon pool species to convert methanol into targeted hydrocarbons,[177,180–182] and as coke precursors leading to zeolite deactivation.[180,181]

Correlations arising from neutral carbon species such as aromatics and alkanes[104] are also shown in Figure 4.16 and 4.17 from which structures such as methylnaphthalenes,[119,177] hexamethylmethylenecyclohexadiene,[118,176] hexamethylbenzene,[119,183] *etc*., could be possibly derived.

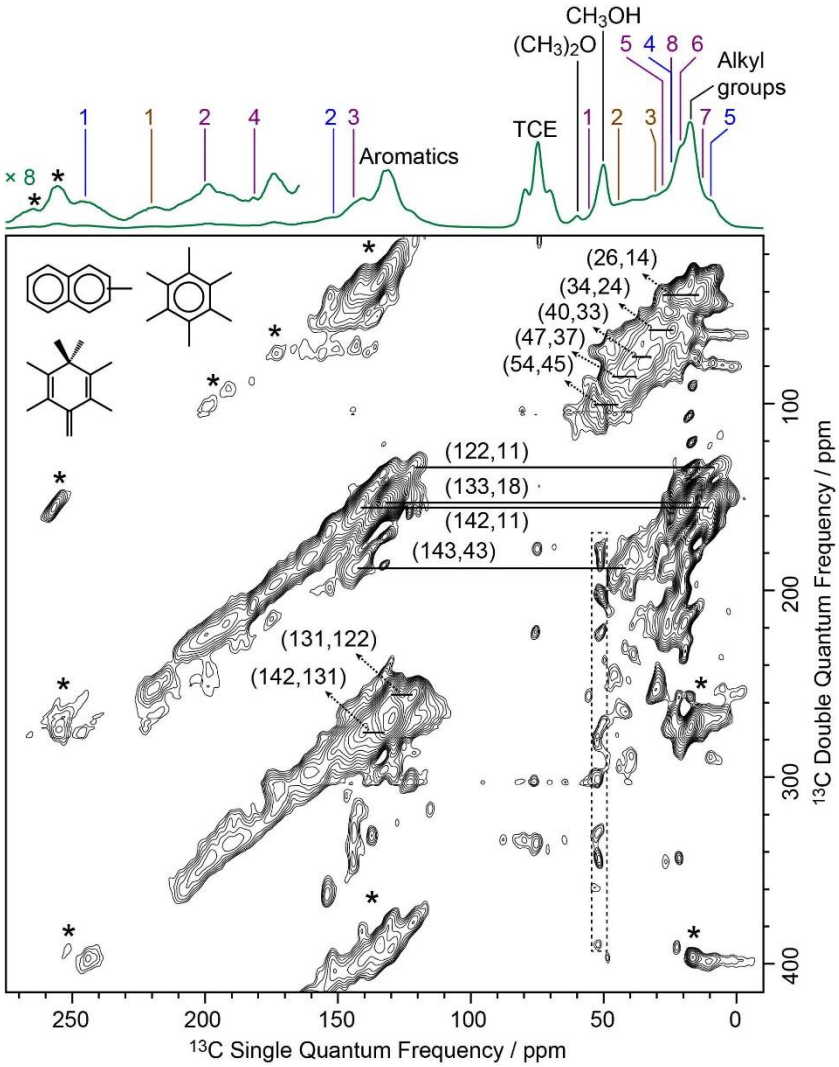

Figure 4.16 DNP enhanced 2D ^{13}C-^{13}C refocused INADEQUATE spectrum of activated M-β. Data was recorded at B_0 = 9.4 T and a MAS frequency of ν_r = 12.5 kHz. Signals in the black dashed box correspond to t_1 noise. Correlations corresponding to the neutral species such as aromatics and alkanes[104] are shown with the ^{13}C chemical shifts in the Single Quantum dimension of the two correlated carbon atoms given in the parenthesis. Structures of such possible compounds are shown in the figure and include methylnaphthalenes,[119,177] hexamethylbenzene,[119,183] hexamethylmethylenecyclohexadiene.[118,176] Asterisks (*) denote spinning sidebands.

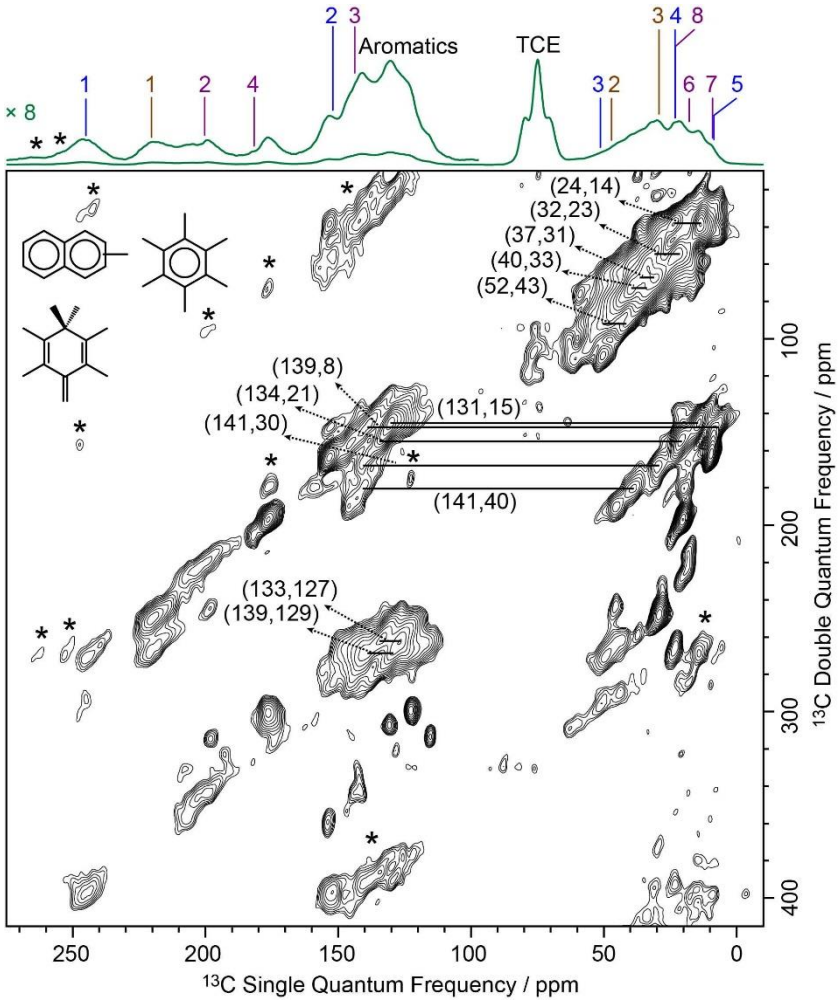

Figure 4.17 DNP enhanced 2D ^{13}C-^{13}C refocused INADEQUATE spectrum of activated MMM-β. Data was recorded at B_0 = 9.4 T and a MAS frequency of ν_r = 12.5 kHz. Correlations corresponding to the neutral species such as aromatics and alkanes[104] are shown with the ^{13}C chemical shifts in the Single Quantum dimension of the two correlated carbon atoms given in the parenthesis. Structures of such possible compounds are shown in the figure and include methylnaphthalenes,[119,177] hexamethylbenzene,[119,183] hexamethylmethylenecyclohexadiene.[118,176] Asterisks (*) denote spinning sidebands.

It is noteworthy that fairly similar cyclic hydrocarbon pool species were identified in both $^{13}CH_3OH$ activated M-β and $^{13}C_2H_4$ activated

MMM-β zeolites (Figure 4.14, 4.15, 4.16 and 4.17). A reasonable route for the formation of the cyclic hydrocarbon species can be proposed here and starts with the initial C-C bond formation from C1 reactants such as CH_3OH and its derivatives to produce ethylene first[110–112] which can then produce cyclic hydrocarbon species *via* polymerization and cyclization[184–187] (Figure 4.18).

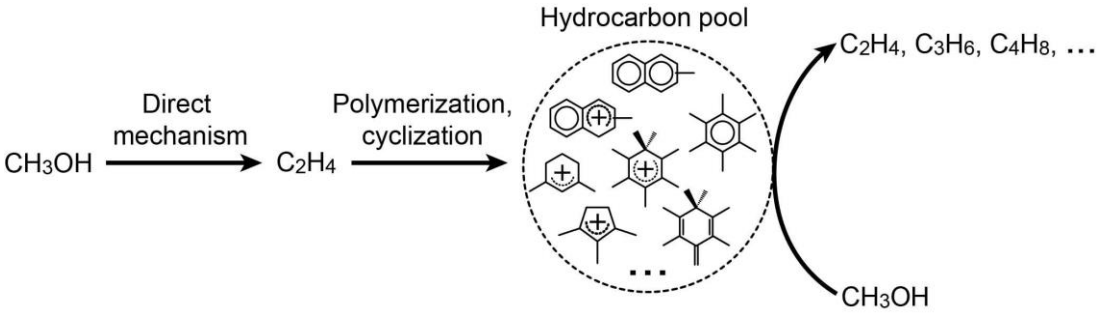

Figure 4.18 Reaction route for the formation of hydrocarbon pool species.[110–112,184–187]

In addition to the scalar coupling based INADEQUATE experiments discussed above, a 2D ^{13}C–^{13}C PDSD DARR MAS correlation experiment on activated MMM-β (Figure 4.19) was also obtained. In this experiment, cross peaks arise from spatial proximities of the species or chemical exchange.[13,14,161] Using a short mixing time of 30 ms, intramolecular correlations are observed,[166] and indeed, correlations from the directly bonded ^{13}C nuclei from the same carbocations are identified in Figure 4.19, which is consistent with the INADEQUATE results. A very small number of correlations from non-bonded ^{13}C nuclei can also be observed in the PDSD DARR spectrum (for example, C1(**I**)

(244 ppm) – C5(**I**) (10 ppm)), reinforcing the INADEQUATE spectral interpretation and the identified carbocations (Figure 4.10).

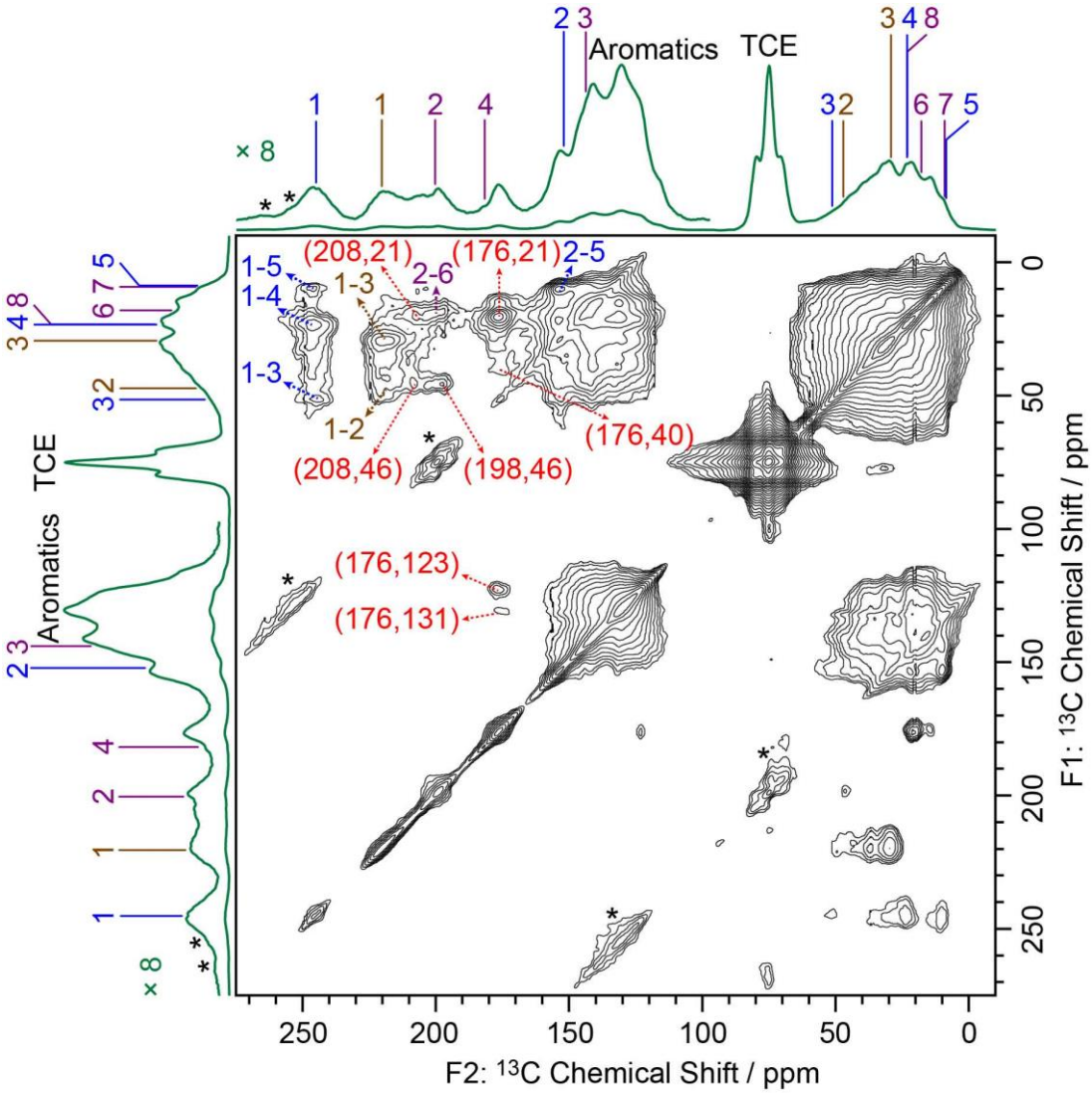

Figure 4.19 DNP enhanced 2D ^{13}C-^{13}C PDSD DARR spectrum of activated MMM-β. Data was recorded at B_0 = 9.4 T and with a MAS frequency of ν_r = 12.5 kHz. The correlations and spectral assignments are coded with the same colors as their corresponding carbocations in Figure 4.10. Correlations corresponding to naphthalenium ions (**IV**) are shown with the ^{13}C chemical shifts of the two correlated carbon atoms given in the parenthesis. Asterisks (*) denote spinning sidebands.

4.4.4 Investigation of the reaction process

Based on the structural determination of the carbon species and the largely increased sensitivity provided by DNP, we further investigated the reaction process by monitoring *ex-situ* the evolution of the DNP enhanced ^{13}C NMR spectra of activated M-β zeolites with variable $^{13}CH_3OH$ activation times (Figure 4.20). The spectra show that even after a very short activation of only one minute, signals from aromatics and carbocations (*e.g.* resonances at 244 and 152 for **I**) are detected. The results demonstrate that the hydrocarbon pool species can be formed at a very early stage of the induction period of the MTH reaction. As activation times increased, the signals of aromatics and carbocations increase in intensity pointing out to the accumulation of these species. The spectrum of M-β activated for 60 minutes is fairly similar to the one after 20 minutes, suggesting that the components of the hydrocarbon pool species are steady over these reaction times.

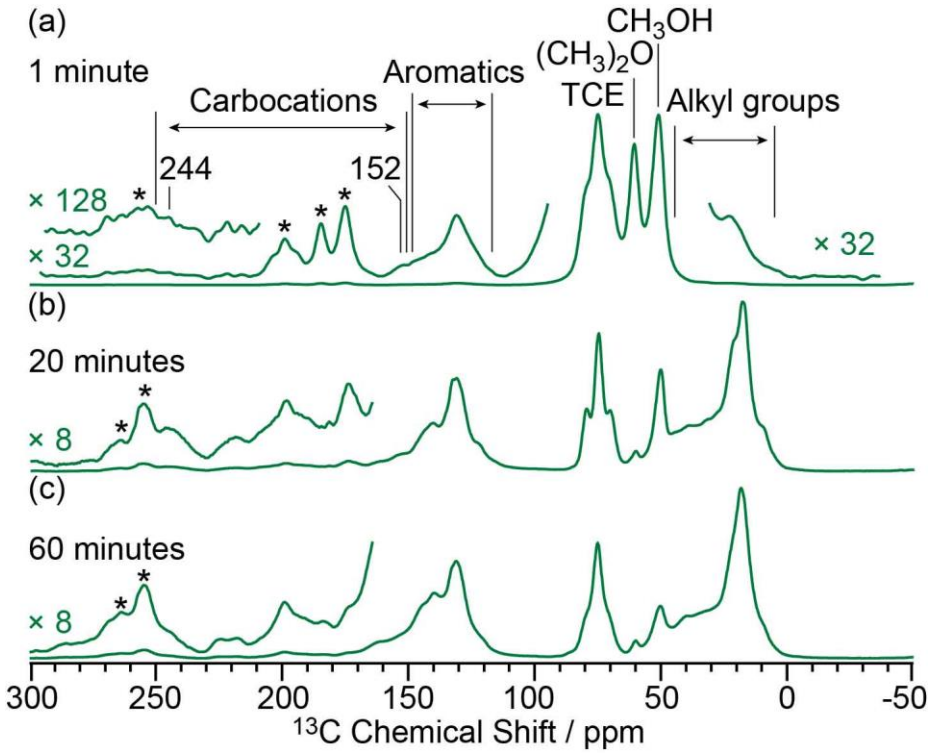

Figure 4.20 μw on ^{13}C CP MAS DNP spectra of M-β activated for (a) one minute, (b) 20 minutes and (c) 60 minutes. Spectra were recorded at 9.4 T and at a MAS rate of 12.5 kHz. Asterisks (*) denote spinning sidebands. Additional spectra at different MAS rate of M-β activated for 20 minutes are shown in Figure 4.21.

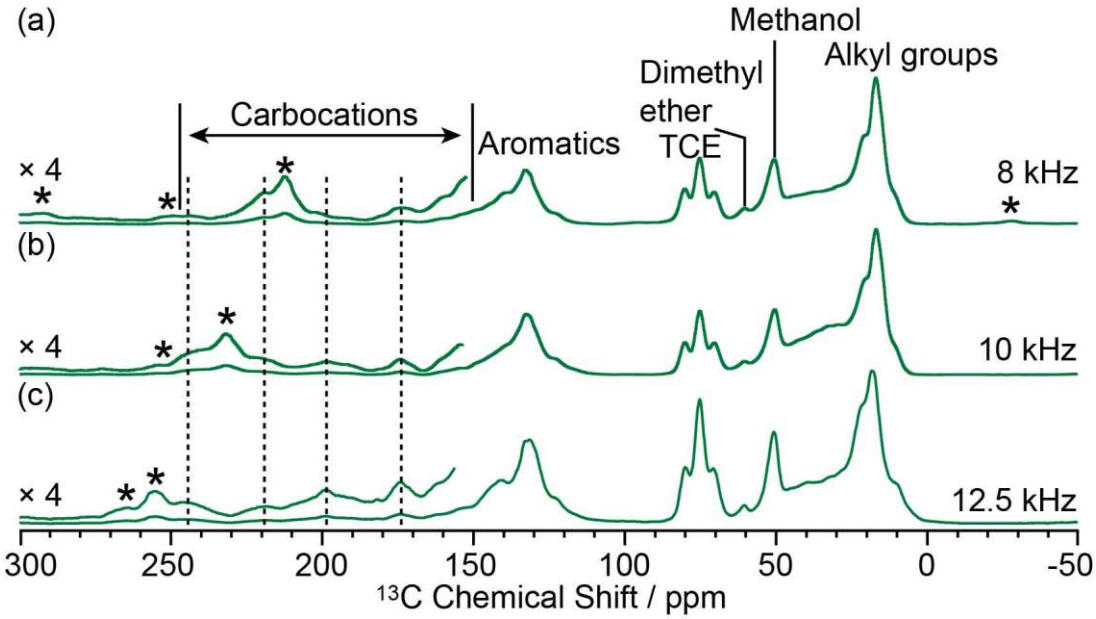

Figure 4.21 ^{13}C CP MAS DNP spectra of activated M-β. Data were recorded at 9.4 T and with a MAS rate of (a) 8 kHz, (b) 10 kHz and (c) 12.5 kHz. Asterisks (*) denote spinning sidebands.

4.4.5 Investigation of host-guest interaction using $^{29}Si\{^{13}C\}$ REDOR

The DNP enhanced ^{29}Si CP MAS spectra of activated M-β and activated MMM-β are shown in Figure 4.22 and both show multiple resonances at -96, -103, -107, -111 and -116 ppm which are characteristic of the $(SiO)_2Si(OH)_2$ (Q^2), $(SiO)_3SiOH$ (Q^3), $Si(OSi)_3(OAl)$ (Si(1Al)), $Si(OSi)_4$ (Q^4) and the crystallographically inequivalent $Si(OSi)_4$ ($Q^{4'}$) sites, respectively, of which the Si(1Al) sites contribute to the Brønsted acid sites.[188,189] $\varepsilon_{Si\,CP}$ DNP enhancement of 9 and overall DNP gain $\Sigma^{\dagger}_{Si\,CP}$ of 96 for M-β (Figure 4.22(a)) and $\varepsilon_{Si\,CP}$ of 45 and $\Sigma^{\dagger}_{Si\,CP}$ of 462 for MMM-β (Figure 4.22(c)) were obtained.

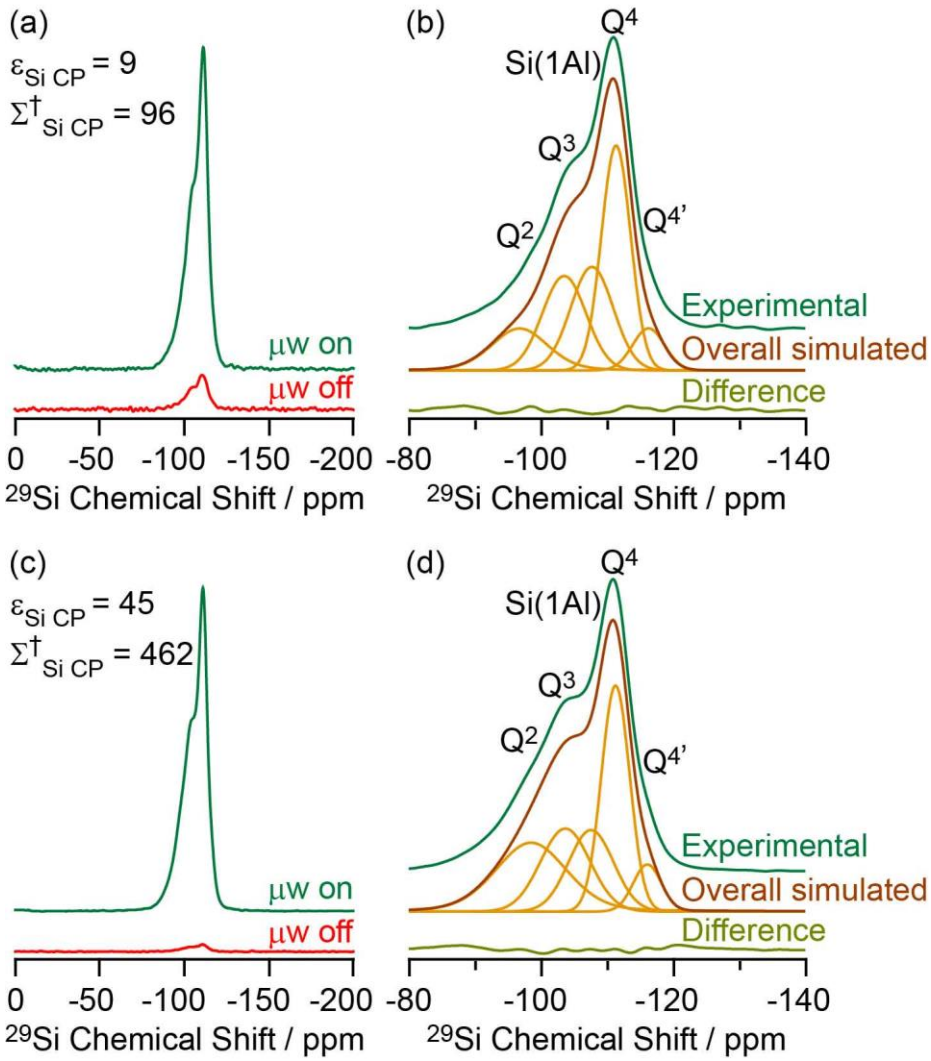

Figure 4.22 (a and c) ^{29}Si CP MAS DNP spectra and (b and d) μw on experimental ^{29}Si CP MAS DNP spectrum with spectral deconvolution, overall simulated lineshape and difference between experimental and simulated spectra of activated M-β (a and b) and activated MMM-β (c and d). All spectra were recorded at 9.4 T and at a MAS rate of 8 kHz. $\Sigma^{\dagger}$ refers to the overall DNP gain and is calculated by comparing the DNP data to room temperature 9.4 T NMR spectra (see section 4.3.7).

These sensitivities permit the fast collection of ^{29}Si detected ^{29}Si{^{13}C} REDOR[16] experiments with high signal-to-noise ratios which would otherwise be extremely time consuming. These experiments reintroduce

the ^{29}Si–^{13}C dipolar couplings under MAS[16] allowing the spatial proximities between the confined carbon species and surface sites of the zeolite to be quantitatively probed. At a recoupling time of 28.5 ms for M-β (Figure 4.23(a)) and 30 ms for MMM-β (Figure 4.24(a)), the ^{13}C dephased ^{29}Si detected signals *S*' show significant reduction in intensities compared with the spin echo signal S_0, demonstrating spatial proximities between ^{29}Si and ^{13}C nuclei. The high S/N ratios permit small differences in the evolutionary pattern of the REDOR fraction $\Delta S/S_0$ as a function of the recoupling times for individual Si sites to be distinguished. The REDOR curves for different Si sites are overlaid in Figure 4.23(b) (for M-β) and 4.24 (b) (for MMM-β) and demonstrate clear differences between these Si sites. Separate figures for each Si site can also be found in Figure 4.25 and 4.26.

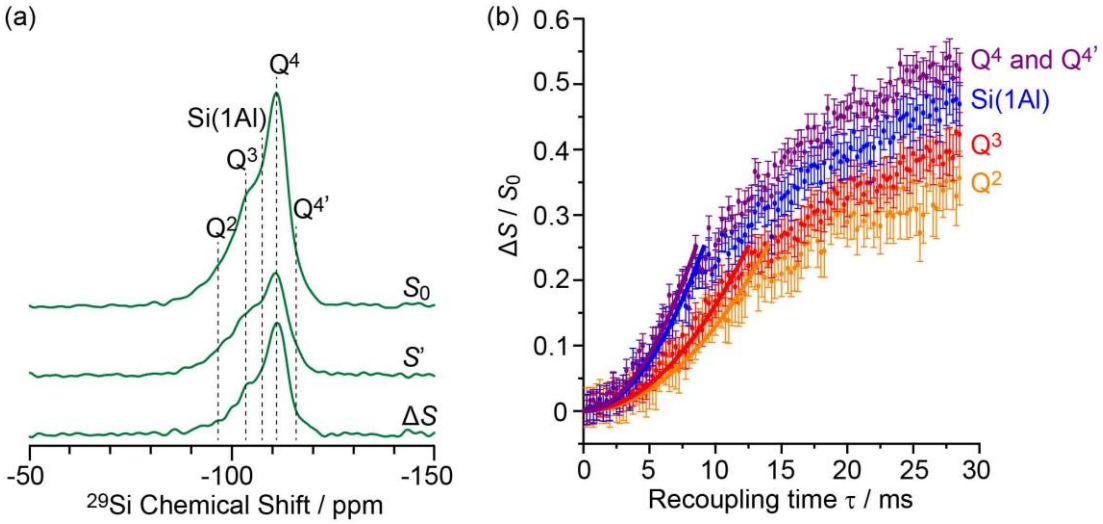

Figure 4.23 (a) DNP enhanced ^{29}Si CP spin echo spectrum (S_0) and ^{29}Si{^{13}C} REDOR spectrum (S') with the reintroduction of dipolar couplings at a recoupling time of 28.5 ms. ΔS is the difference spectrum S_0 - S'. Spectra were recorded at 9.4 T on activated M-β. (b) ^{29}Si{^{13}C} REDOR fraction $\Delta S/S_0$ as a function of the recoupling time up to 28.5 ms. The experimental time is ≈ 15 hours. The solid lines are best-fit of the REDOR curves up to a $\Delta S/S_0$ of 0.3 using a first-order approximation and equation 2.2 in section 2.3.4.2.[128] The ^{29}Si-^{13}C dipolar coupling values are given in Table 4.7. The vertical error bars correspond to the error analysis as given in section 4.3.8. The REDOR curves for each ^{29}Si site are also shown separately in Figure 4.25.

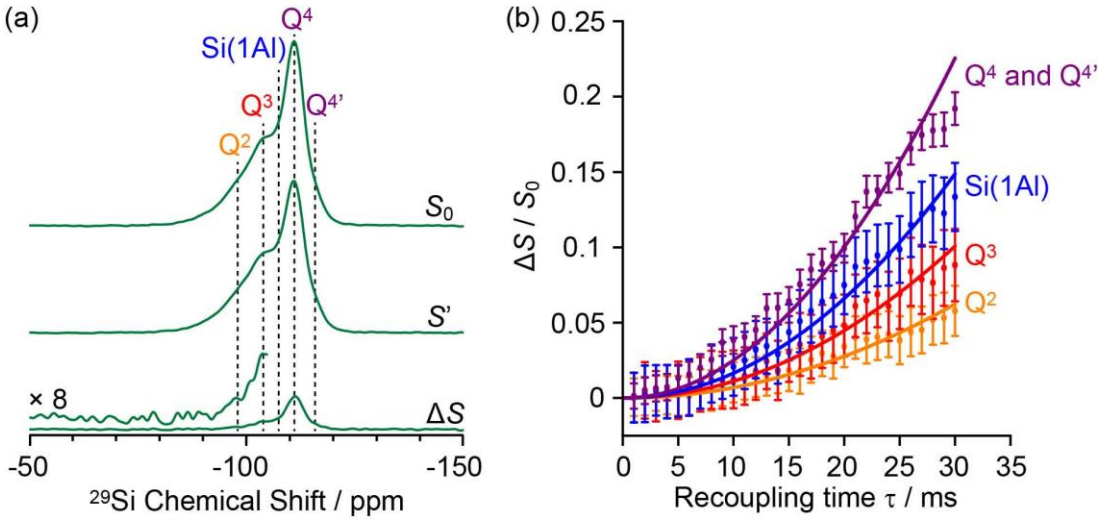

Figure 4.24 (a) DNP enhanced ^{29}Si CP spin echo spectrum (S_0) and ^{29}Si{^{13}C} REDOR spectrum (S') with the reintroduction of dipolar couplings at a recoupling time of 30 ms. ΔS is the difference spectrum S_0 - S'. Spectra were recorded at 9.4 T on activated MMM-β. (b) ^{29}Si{^{13}C} REDOR fraction $\Delta S/S_0$ as a function of the recoupling times up to 30 ms. The experimental time is ≈ 11 hours. The solid lines are best-fit of the REDOR curves using equation 2.2 and the ^{29}Si-^{13}C dipolar coupling values given in Table 4.7. The vertical error bars correspond to the error analysis as given in section 4.3.8. The REDOR curves for each ^{29}Si sites are also shown separately in Figure 4.26.

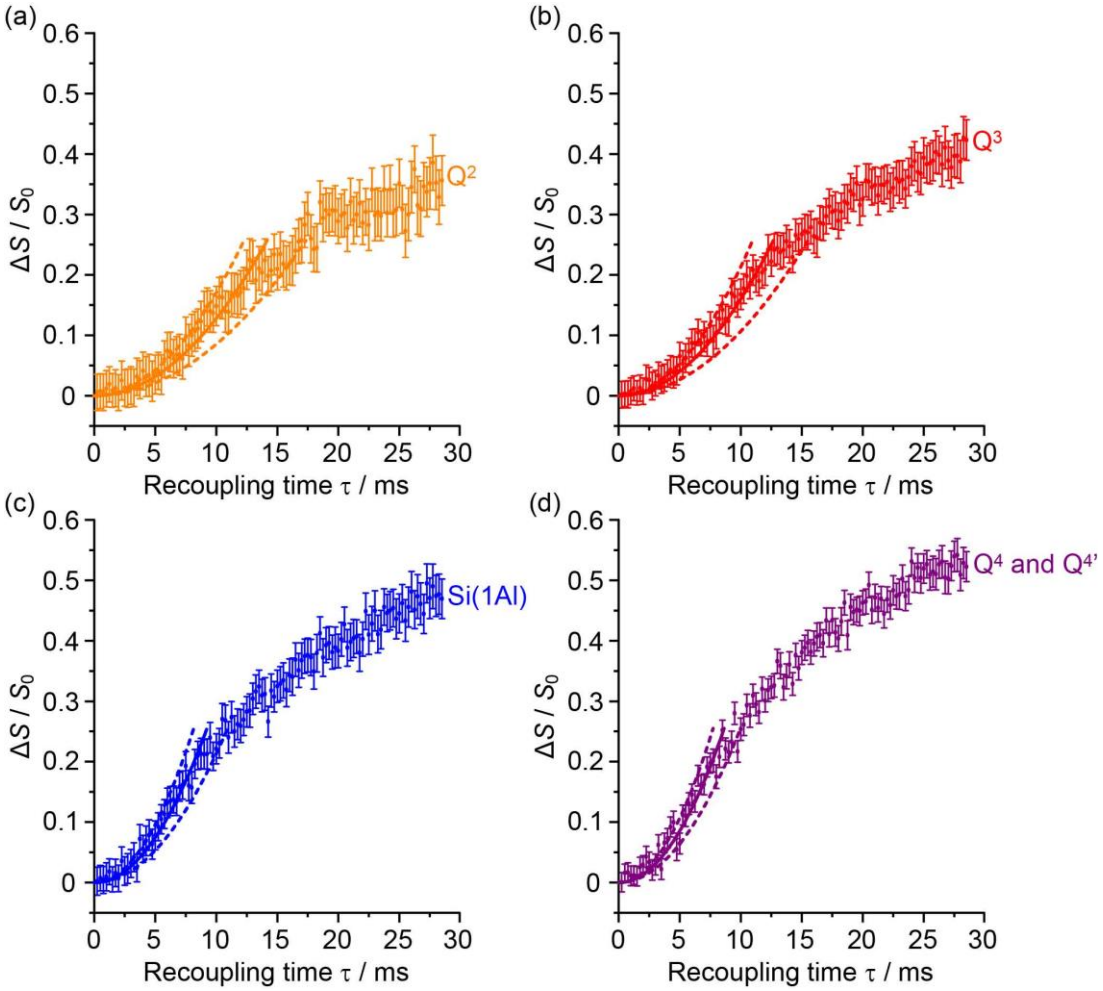

Figure 4.25 Individual $^{29}Si\{^{13}C\}$ REDOR curves for each ^{29}Si sites of activated M-β. The solid lines are best-fit of the REDOR curves (see Figure 4.23(b)) while the dashed lines correspond to the fit boundaries corresponding to the errors in the simulated ^{29}Si-^{13}C dipolar coupling values given in Table 4.7.

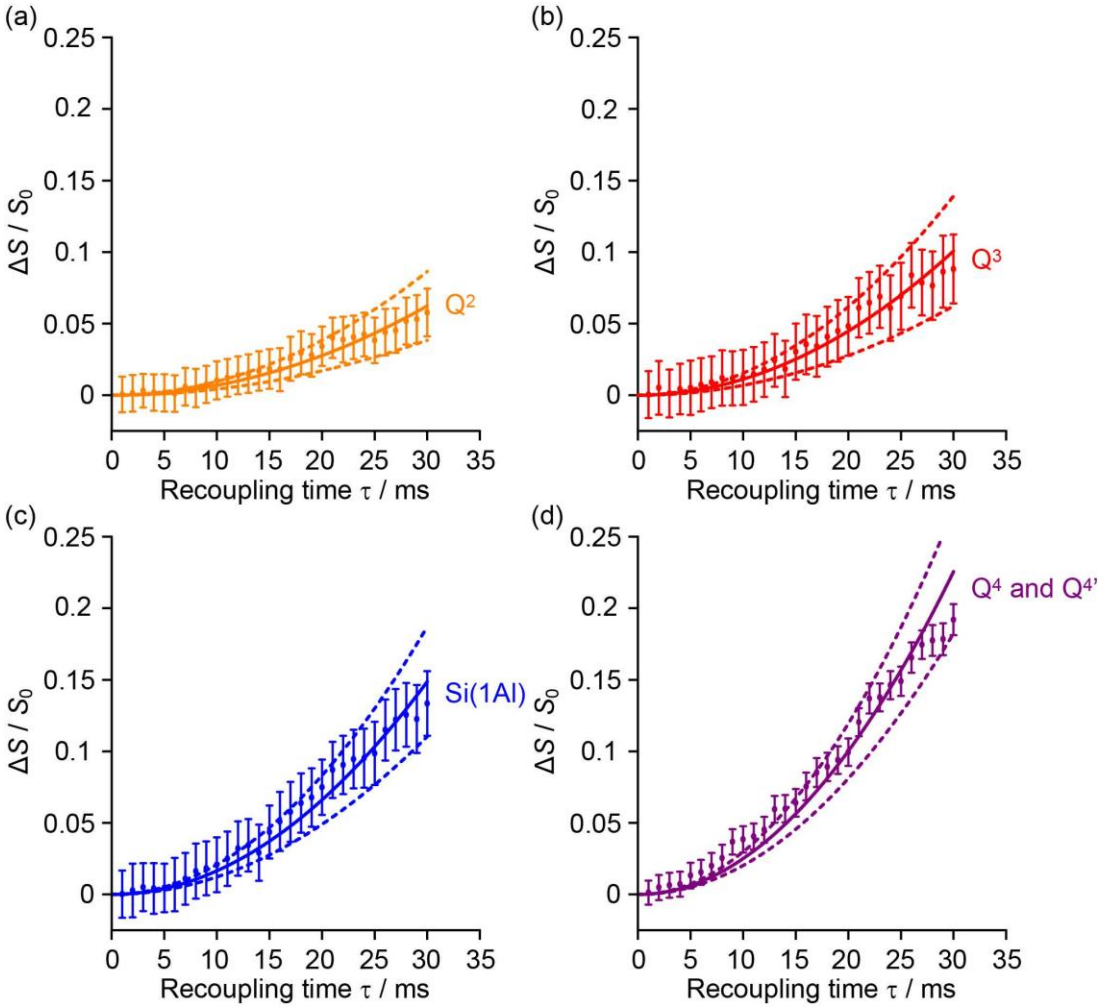

Figure 4.26 Individual $^{29}Si\{^{13}C\}$ REDOR curves for each ^{29}Si sites of activated MMM-β. The solid lines are best-fit of the REDOR curves (see Figure 4.24(b)) while the dashed lines correspond to the fit boundaries corresponding to the errors in the simulated ^{29}Si-^{13}C dipolar coupling values given in Table 4.7.

Table 4.7 ^{29}Si-^{13}C dipolar coupling strengths D and distances r in activated M-β and MMM-β obtained from the ^{29}Si{^{13}C} REDOR experiments (see section 4.3.8 for the fitting procedure and description of the fitting model)

Zeolite	^{29}Si sites	$\sum D_i^2$ / Hz^2	D / Hz[a]	r / Å[a]
Activated M-β	Q^2	1200 ± 400	35 ± 7	5.6 ± 0.4
	Q^3	1500 ± 500	39 ± 7	5.4 ± 0.3
	Si(1Al)	2800 ± 800	53 ± 8	4.8 ± 0.3
	Q^4 + $Q^{4'}$	3200 ± 800	57 ± 8	4.7 ± 0.3
Activated MMM-β	Q^2	65 ± 25	8 ± 2	9.1 ± 0.7
	Q^3	105 ± 40	10 ± 2	8.4 ± 0.7
	Si(1Al)	155 ± 40	12 ± 2	7.8 ± 0.4
	Q^4 + $Q^{4'}$	235 ± 45	15 ± 2	7.3 ± 0.3

[a] Assuming a simplified 29Si-13C single spin pair model.

Considering the number of retained carbon species and their unknown geometries in the zeolites, a geometrically independent REDOR curve model which only requires data at short dipolar recoupling times ($\Delta S/S_0$ up to 0.3)[128] was used to fit the REDOR data (see section 4.3.8 for further details) and the results are summarized in Table 4.7. By further assuming a ^{29}Si-^{13}C single spin pair model, an estimation of the ^{29}Si-^{13}C dipolar coupling strengths and distances is also given.

The ^{29}Si{^{13}C} REDOR data (Table 4.7) show that both Q^4 and Si(1Al) sites have the strongest interaction with the hydrocarbon pool species in activated M-β with $\sum D_i^2$ being 3200 ± 800 Hz^2 and 2800 ± 800 Hz^2, respectively. This major contribution to the ^{29}Si{^{13}C} REDOR curves is expected as neutral aromatic species are the main hydrocarbon pool

species, as shown in the ^{13}C CP spectra, and interact more strongly with the zeolite frameworks. The similar interaction between the hydrocarbons and both Q^4 and Si(1Al) sites also suggests that the van der Waals interaction with the zeolite framework dominates the adsorption of these hydrocarbon pool species within the micropores (known as the confinement effects)[138] and that, surprisingly, there is no evidence for preferential interaction with the Brønsted acid sites of the zeolites. The zeolite deactivation during the MTH process is therefore likely due to the accumulation of aromatics in the channels of the zeolite and their further growth to form polycyclic cokes blocking the reactants' accesses to the catalytic acid sites supporting previous computational studies.[138,140] The quantitative information provides here also promotes understanding of the nature of the previously proposed supramolecular reaction centers[137] and yields structural constraints (distance of around 4.8 Å) between the hydrocarbon pool species and zeolite frameworks. Table 4.7 also shows that the Q^2 and Q^3 sites have much weaker interaction with the hydrocarbon pool species suggesting that these silanol defects are mainly located at the external surface.

Comparison of the $^{29}Si\{^{13}C\}$ REDOR data for both activated zeolites (Table 4.7) revealed that the Si sites show much weaker interaction with the hydrocarbon pool species in MMM-β than in M-β. We ascribe this phenomenon to the presence of the mesopores in MMM-β which weaken the confinement effects and suggest that some carbon species should predominantly locate in the mesopores.

Note that the $^{29}Si\{^{13}C\}$ REDOR results do not exclude the possibility that carbocations have strong interaction with the Brønsted acid sites, likely *via* the formation of ion-pair complexes,[141] since the $^{29}Si\{^{13}C\}$ REDOR experiments measure the overall dipolar coupling to ^{29}Si from ^{13}C spins of different molecules while not distinguishing the source of the contribution.

4.5 Conclusions

In summary, we have demonstrated that a small concentration of carbocations confined in zeolites can be detected within minutes by DNP enhanced multinuclear NMR spectroscopy. The large DNP signal enhancements enable acquisition of 2D ^{13}C-^{13}C NMR correlation experiments in hours which would otherwise take days or even weeks without DNP. These correlations permit the identification of a series of five- and six-membered ring carbocations serving as intermediates in the MTH reaction. In particular, methylnaphthalenium ions are identified and reinforce their importance as hydrocarbon pool species for the formation of targeted hydrocarbon products and coke precursors leading to zeolite deactivation. Additionally, the host-guest interaction between various silicon sites of zeolites and hydrocarbon pool species is quantitatively determined *via* DNP enhanced $^{29}Si\{^{13}C\}$ REDOR experiments, which indicate that van der Waals interaction with the zeolite frameworks dominates the adsorption of the majority hydrocarbon pool species, suggesting accumulation of these species in the channels and leading to zeolite deactivation. Finally, we show that introducing hierarchical pores into zeolites is a promising way to improve DNP efficiency on this type

of materials. The implications of this strategy to tackle the understanding of hierarchically structured porous materials of considerable interests in catalysis, gas adsorption, sensing, *etc.*,[158,190] are potentially very large.

Chapter 5: Overall Conclusions and Outlook

5.1 Overall Conclusions

In Chapter 2 it is shown that the scalar J coupling based ^{13}C-^{13}C INADEQUATE experiment leads to unambiguous assignment of the ^{13}C NMR spectrum of the MTO activated H-ZSM-5 and directly yields the molecular structures of a series of carbocation intermediates in it with atomic precision. The identified carbocations further confirm some previous proposed structures and include a previously undetected 1,5-dimethyl-3-*sec*-butyl cyclopentenyl cation. The experimental identification of the new cation provides direct support for the aromatic-based paring route for butene formation in H-ZSM-5. In addition, the host-guest interactions are quantitatively probed from the perspectives of both the confined carbon species and the H-ZSM-5 framework *via* ^{13}C detected $^{13}C\{^{27}Al\}$ S-RESPDOR and ^{29}Si detected $^{29}Si\{^{13}C\}$ REDOR experiments. The results reveal carbon–aluminium and carbon–silicon host–guest distances in the range of 4.2–4.7 °A, providing quantitative information for the pore confinement interactions.

In Chapter 3 the same NMR experiment is applied to the investigation of carbocations in the MTO activated H-SAPO-34 and H-SSZ-13 zeolites. These two zeolites possess identical CHA topology but are with different framework components. Previous works using a combination of indirect methods tend to assuming same carbocations in these two zeolites. However, the 2D ^{13}C-^{13}C

INADEQUATE spectra with better resolution offered by the additional second dimension than the 1D ^{13}C CP NMR spectra clearly demonstrate different ^{13}C-^{13}C correlation patterns for H-SAPO-34 and H-SSZ-13, indicating different carbon species. It is shown that 1,2,3,4-tetramethylcyclopentenyl and 1,2,3-trimethylcyclopentenyl cations are the major retained cation species on H-SSZ-13 and H-SAPO-34 CHA zeolites, respectively.

Chapter 2 and 3 demonstrate that multidimensional and multinuclear NMR methods are very powerful for structural identification and investigation on host-guest interactions. However, the experimental times needed to acquire the multidimensional and multinuclear NMR data were prohibitively long (>5 days), even with ^{13}C labelling on the carbocations. This is due to the low concentrations of the reactive carbocations than can be captured and significantly hinders the systematic use of these informative approaches on a wider range of solid acids with a low amount of carbocation intermediates. Therefore, in chapter 4 we explore the use of DNP NMR to detect carbocations confined in porous zeolites. The recent DNP literature shows limited applications for microporous zeolites perhaps due to possible chemically incompatible between radical solutions and zeolites, difficulties associated with polarization transfer to the interior of micropores, etc., the results in chapter 4 demonstrate that introducing hierarchical pores with different sizes ranging from micro (<2 nm), meso (2–50 nm) to macro pores (>50 nm) effectively optimizes DNP efficiency on zeolites. It is also shown that the

nonaqueous TEKPol/TCE matrix is chemically compatible with the investigated carbocations. Significant enhancements (> 40) were obtained on both the ^{13}C signals of carbocations and ^{29}Si signals of the zeolite framework, which enable the detection of carbocations within minutes and the acquisition of multidimensional and multinuclear NMR experiments within hours, corresponding to a very significant reduction in experimental time. Methylnaphthalenium ions are identified and reinforce their importance as hydrocarbon pool species for the formation of targeted hydrocarbon products and coke precursors leading to zeolite deactivation. Additionally, the quantitative information of the host–guest interaction between various silicon sites of zeolites and hydrocarbon pool species indicates that van der Waals interaction with the zeolite frameworks dominates the adsorption of the majority hydrocarbon pool species, suggesting accumulation of these species in the channels and leading to zeolite deactivation.

5.2 Outlook

Chapter 2 and 3 fully demonstrate that multidimensional and multinuclear NMR methods are very useful for determining the molecular structures of carbocations directly without post treatments on samples which are commonly needed in indirect approaches previously used[88,105,151]. The informative results shown in this thesis will potentially inspire the application of those powerful multidimensional and multinuclear NMR approaches in heterogeneous

catalysis research.

This thesis has demonstrated that introducing hierarchical pores into zeolites is a promising way to improve DNP performances on this type of materials. Since the hierarchically porous materials have been widely used in energy storage and conversion, catalysis, gas adsorption separation, biomedicine sensing, *etc*.[158,190] DNP NMR will undoubtedly play an important role in research of these areas.

In this thesis, we choose zeolites with carbocation intermediates formed during the MTH reactions as model samples to investigate the applicability of DNP to the studies of carbocations. The nonaqueous TEKPol/TCE solution was found to be compatible with the carbocations and can be a routine choice of radical solution for future DNP investigation on carbocations. DNP shows great potential to improve the detecting limit of carbocation intermediates, enables their detection within minutes and structural identification within hours which would otherwise take days or even weeks without DNP. Therefore, DNP opens new opportunities to the fundamental research on some heterogenous catalysis reactions with reaction intermediates and mechanisms unclear.

For the fundamental research of MTH mechanism, the HCP mechanism has been extensively studied and generally accepted as main route for methanol conversion to hydrocarbons during the steady-state period. Recent research on MTH mechanism have turned to answering how the initial C-C bond forms from C1 reactants (methanol and its derivatives) at the early stage

of reaction and bridging the gap between those initial C-C species and hydrocarbon pool species.[110–112,184–186] Answering these questions requires capturing the low concentration of early products and reactive intermediates such as trimethyloxonium ions[112] and monitoring their evolution along reaction processes. For these studies, DNP NMR and those informative multidimensional and multinuclear NMR techniques can undoubtedly play important roles.

The properties of zeolite catalysts, especially the structures of their acid sites such as Brønsted and Lewis acid sites, are of great interests to both zeolite and catalysis communities.[191–193] Oxygen is the main component of these structures, and ^{17}O NMR could have provided direct structural information for these acid sites. However, the application of ^{17}O NMR is currently hindered by its low sensitivity and rather low natural abundance of ^{17}O (0.0373%). Previously, ^{17}O enrichment on zeolites was explored, which was shown requiring rather harsh experimental conditions (^{17}O exchange temperature as high as 580 °C).[194] Such high temperature may cause unfavorable structural destruction to zeolite framework. ^{17}O DNP NMR provides a non-destructive way to investigate the acid properties of zeolites at natural abundance. The great potential of ^{17}O DNP NMR has recently been shown on silica–alumina for which natural abundance ^{17}O DNP NMR was used to measure the O-H bond length of different acidic hydroxyls on the surface with an unprecedented, sub-pm precision.[60] ^{17}O DNP NMR investigation on

acid sites of zeolites has yet to be demonstrated.

Notes and references

1 J. Keeler, *Understanding NMR spectroscopy*, John Wiley & Sons, 2002.
2 M. H. Levitt, *Spin Dynamics: Basics of Nuclear Magnetic Resonance*, John Wiley & Sons, 2001.
3 D. D. Laws, H.-M. L. Bitter and A. Jerschow, *Angew. Chem. Int. Ed.*, 2002, **41**, 3096–3129.
4 E. R. Andrew, A. Bradbury and R. G. Eades, *Nature*, 1958, 182, 1659.
5 A. Pines, M. G. Gibby and J. S. Waugh, *J. Chem. Phys.*, 1973, **59**, 569–590.
6 S. V. Dvinskikh, H. Zimmermann, A. Maliniak and D. Sandström, *J. Magn. Reson.*, 2004, **168**, 194–201.
7 A. E. Bennett, C. M. Rienstra, M. Auger, K. V Lakshmi and R. G. Griffin, *J. Chem. Phys.*, 1995, **103**, 6951–6958.
8 B. M. Fung, A. K. Khitrin and K. Ermolaev, *J. Magn. Reson.*, 2000, **142**, 97–101.
9 P. Hodgkinson, Ed., *Modern Methods in Solid-state NMR: A Practitioner's Guide*, The Royal Society of Chemistry, 2018.
10 A. Lesage, C. Auger, S. Caldarelli and L. Emsley, *J. Am. Chem. Soc.*, 1997, **119**, 7867–7868.
11 A. Lesage, M. Bardet and L. Emsley, *J. Am. Chem. Soc.*, 1999, **121**, 10987–10993.
12 D. Massiot, F. Fayon, B. Alonso, J. Trebosc and J. P. Amoureux, *J. Magn. Reson.*, 2003, **164**, 160–164.
13 N. M. Szeverenyi, M. J. Sullivan and G. E. Maciel, *J. Magn. Reson.*, 1982, **47**, 462–475.
14 K. Takegoshi, S. Nakamura and T. Terao, *Chem. Phys. Lett.*, 2001, **344**, 631–637.
15 B. Hu, J. Trébosc and J. P. Amoureux, *J. Magn. Reson.*, 2008, **192**, 112–122.
16 T. Gullion, *Concepts Magn. Reson.*, 1998, **10**, 277–289.
17 D. A. Hall, D. C. Maus, G. J. Gerfen, S. J. Inati, L. R. Becerra, F. W. Dahlquist and R. G. Griffin, *Science*, 1997, **276**, 930–932.
18 A. Lesage, M. Lelli, D. Gajan, M. A. Caporini, V. Vitzthum, P. Miéville, J. Alauzun, A. Roussey, C. Thieuleux, A. Mehdi, G. Bodenhausen, C. Copéret and L. Emsley, *J. Am. Chem. Soc.*, 2010, **132**, 15459–15461.
19 Q. Z. Ni, E. Daviso, T. V. Can, E. Markhasin, S. K. Jawla, T. M. Swager, R. J. Temkin, J. Herzfeld and R. G. Griffin, *Acc. Chem. Res.*, 2013, **46**, 1933–1941.
20 A. J. Rossini, A. Zagdoun, M. Lelli, A. Lesage, C. Copéret and L. Emsley, *Acc. Chem. Res.*, 2013, **46**, 1942–1951.
21 A. W. Overhauser, *Phys. Rev.*, 1953, **92**, 411–415.
22 T. R. Carver and C. P. Slichter, *Phys. Rev.*, 1953, 92, 212–213.

23 T. R. Carver and C. P. Slichter, *Phys. Rev.*, 1956, **102**, 975–980.
24 A. G. M. Rankin, J. Trébosc, F. Pourpoint, J. P. Amoureux and O. Lafon, *Solid State Nucl. Magn. Reson.*, 2019, **101**, 116–143.
25 L. R. Becerra, G. J. Gerfen, R. J. Temkin, D. J. Singel and R. G. Griffin, *Phys. Rev. Lett.*, 1993, **71**, 3561.
26 G. J. Gerfen, L. R. Becerra, D. A. Hall, R. G. Griffin, R. J. Temkin and D. J. Singel, *J. Chem. Phys.*, 1998, **102**, 9494–9497.
27 F. Blanc, in *Nanotechnology in Catalysis: Applications in the Chemical Industry, Energy Development, and Environment Protection*, eds. M. Van de Voorde and B. Sels, Wiley-Blackwell, 2017, pp. 1003–1028.
28 M. Rosay, L. Tometich, S. Pawsey, R. Bader, R. Schauwecker, M. Blank, P. M. Borchard, S. R. Cauffman, K. L. Felch, R. T. Weber, R. J. Temkin, R. G. Griffin and W. E. Maas, *Phys. Chem. Chem. Phys.*, 2010, **12**, 5850–5860.
29 T. V. Can, M. A. Caporini, F. Mentink-Vigier, B. Corzilius, J. J. Walish, M. Rosay, W. E. Maas, M. Baldus, S. Vega, T. M. Swager and R. G. Griffin, *J. Chem. Phys.*, 2014, **141**, 064202.
30 M. Lelli, S. R. Chaudhari, D. Gajan, G. Casano, A. J. Rossini, O. Ouari, P. Tordo, A. Lesage and L. Emsley, *J. Am. Chem. Soc.*, 2015, **137**, 14558–14561.
31 C. Song, K. N. Hu, C. G. Joo, T. M. Swager and R. G. Griffin, *J. Am. Chem. Soc.*, 2006, **128**, 11385–11390.
32 Y. Matsuki, T. Maly, O. Ouari, H. Karoui, F. Le Moigne, E. Rizzato, S. Lyubenova, J. Herzfeld, T. Prisner, P. Tordo and R. G. Griffin, *Angew. Chem. Int. Ed.*, 2009, **48**, 4996–5000.
33 A. Zagdoun, G. Casano, O. Ouari, G. Lapadula, A. J. Rossini, M. Lelli, M. Baffert, D. Gajan, L. Veyre, W. E. Maas, M. Rosay, R. T. Weber, C. Thieuleux, C. Coperet, A. Lesage, P. Tordo and L. Emsley, *J. Am. Chem. Soc.*, 2012, **134**, 2284–2291.
34 A. Zagdoun, G. Casano, O. Ouari, M. Schwarzwälder, A. J. Rossini, F. Aussenac, M. Yulikov, G. Jeschke, C. Copéret, A. Lesage, P. Tordo and L. Emsley, *J. Am. Chem. Soc.*, 2013, **135**, 12790–12797.
35 C. Sauvée, M. Rosay, G. Casano, F. Aussenac, R. T. Weber, O. Ouari and P. Tordo, *Angew. Chem. Int. Ed.*, 2013, **52**, 10858–10861.
36 A. J. Rossini, A. Zagdoun, F. Hegner, M. Schwarzwälder, D. Gajan, C. Copéret, A. Lesage and L. Emsley, *J. Am. Chem. Soc.*, 2012, **134**, 16899–16908.
37 W. R. Gunther, V. K. Michaelis, M. A. Caporini, R. G. Griffin and Y. Román-Leshkov, *J. Am. Chem. Soc.*, 2014, **136**, 6219–6222.
38 M. Afeworki and J. Schaefer, *Macromolecules*, 1992, **25**, 4092–4096.
39 O. Lafon, M. Rosay, F. Aussenac, X. Lu, J. Trébosc, O. Cristini, C. Kinowski, N. Touati, H. Vezin and J.-P. P. Amoureux, *Angew. Chem. Int. Ed.*, 2011, **50**, 8367–8370.
40 M. A. Hope, D. M. Halat, P. C. M. M. Magusin, S. Paul, L. Peng and C.

P. Grey, *Chem. Commun.*, 2017, **53**, 2142–2145.
41 M. Rosay, M. Blank and F. Engelke, *J. Magn. Reson.*, 2016, **264**, 88–98.
42 A. Zagdoun, A. J. Rossini, D. Gajan, A. Bourdolle, O. Ouari, M. Rosay, W. E. Maas, P. Tordo, M. Lelli, L. Emsley, A. Lesage and C. Copéret, *Chem. Commun.*, 2012, **48**, 654–656.
43 A. J. Rossini, A. Zagdoun, M. Lelli, D. Gajan, F. Rascón, M. Rosay, W. E. Maas, C. Copéret, A. Lesage and L. Emsley, *Chem. Sci.*, 2012, **3**, 108–115.
44 P. Fricke, D. Mance, V. Chevelkov, K. Giller, S. Becker, M. Baldus and A. Lange1, *J. Biomol. NMR*, 2016, **65**, 121–126.
45 T. Kobayashi, F. A. Perras, I. I. Slowing, A. D. Sadow and M. Pruski, *ACS Catal.*, 2015, **5**, 7055–7062.
46 F. Blanc, S. Y. Chong, T. O. McDonald, D. J. Adams, S. Pawsey, M. A. Caporini and A. I. Cooper, *J. Am. Chem. Soc.*, 2013, **135**, 15290–15293.
47 F. A. Perras, T. Kobayashi and M. Pruski, *J. Am. Chem. Soc.*, 2015, **137**, 8336–8339.
48 P. Wolf, M. Valla, A. J. Rossini, A. Comas‐Vives, F. Núñez‐Zarur, B. Malaman, A. Lesage, L. Emsley, C. Copéret and I. Hermans, *Angew. Chem. Int. Ed.*, 2014, **53**, 10179–10183.
49 F. Blanc, L. Sperrin, D. Lee, R. Dervişoğlu, Y. Yamazaki, S. M. Haile, G. De Paëpe and C. P. Grey, *J. Phys. Chem. Lett.*, 2014, **5**, 2431–2436.
50 N. J. Brownbill, D. Lee, G. De Paëpe and F. Blanc, *J. Phys. Chem. Lett.*, 2019, **10**, 3501–3508.
51 M. Lelli, D. Gajan, A. Lesage, M. A. Caporini, V. Vitzthum, P. Miéville, F. Héroguel, F. Rascón, A. Roussey, C. Thieuleux, M. Boualleg, L. Veyre, G. Bodenhausen, C. Copéret and L. Emsley, *J. Am. Chem. Soc.*, 2011, **133**, 2104–2107.
52 T.-C. Ong, W.-C. Liao, V. Mougel, D. Gajan, A. Lesage, L. Emsley and C. Copéret, *Angew. Chem. Int. Ed.*, 2016, **55**, 4743–4747.
53 V. Vitzthum, P. Miéville, D. Carnevale, M. a. Caporini, D. Gajan, C. Copéret, M. Lelli, A. Zagdoun, A. J. Rossini, A. Lesage, L. Emsley and G. Bodenhausen, *Chem. Commun.*, 2012, **48**, 1988–1990.
54 D. Lee, H. Takahashi, A. S. L. Thankamony, J.-P. Dacquin, M. Bardet, O. Lafon and G. De Paëpe, *J. Am. Chem. Soc.*, 2012, **134**, 18491–18494.
55 D. Lee, N. T. Duong, O. Lafon and G. De Paëpe, *J. Phys. Chem. C*, 2014, **118**, 25065–25076.
56 R. L. Johnson, F. A. Perras, T. Kobayashi, T. J. Schwartz, J. A. Dumesic, B. H. Shanks and M. Pruski, *Chem. Commun.*, 2016, **52**, 1859–1862.
57 F. A. Perras, J. D. Padmos, R. L. Johnson, L. L. Wang, T. J. Schwartz, T. Kobayashi, J. H. Horton, J. A. Dumesic, B. H. Shanks, D. D. Johnson and M. Pruski, *J. Am. Chem. Soc.*, 2017, **139**, 2702–2709.
58 M. Valla, A. J. Rossini, M. Caillot, C. Chizallet, P. Raybaud, M. Digne, A.

Chaumonnot, A. Lesage, L. Emsley, J. A. van Bokhoven and Christophe Copéret, *J. Am. Chem. Soc.*, 2015, **137**, 10710–10719.

59 A. G. M. Rankin, P. B. Webb, D. M. Dawson, J. Viger-Gravel, B. J. Walder, L. Emsley and S. E. Ashbrook, *J. Phys. Chem. C*, 2017, **121**, 22977–22984.

60 F. A. Perras, Z. Wang, P. Naik, I. I. Slowing and M. Pruski, *Angew. Chem. Int. Ed.*, 2017, **56**, 9165–9169.

61 P. Wolf, M. Valla, F. Núñez-Zarur, A. Comas-Vives, A. J. Rossini, C. Firth, H. Kallas, A. Lesage, L. Emsley, C. Copéret and I. Hermans, *ACS Catal.*, 2016, **6**, 4047–4063.

62 A. J. Rossini, A. Zagdoun, M. Lelli, J. Canivet, S. Aguado, O. Ouari, P. Tordo, M. Rosay, W. E. Maas, C. Copéret, D. Farrusseng, L. Emsley and A. Lesage, *Angew. Chem. Int. Ed.*, 2012, **51**, 123–127.

63 Z. Guo, T. Kobayashi, L. L. Wang, T. W. Goh, C. Xiao, M. A. Caporini, M. Rosay, D. D. Johnson, M. Pruski and W. Huang, *Chem. - A Eur. J.*, 2014, **20**, 16308–16313.

64 P. Berruyer, M. Lelli, M. P. Conley, D. L. Silverio, C. M. Widdifield, G. Siddiqi, D. Gajan, A. Lesage, C. Copéret and L. Emsley, *J. Am. Chem. Soc.*, 2017, **139**, 849–855.

65 F. A. Perras, U. Chaudhary, I. I. Slowing and M. Pruski, *J. Phys. Chem. C*, 2016, **120**, 11535–11544.

66 E. Pump, J. Viger-Gravel, E. Abou-Hamad, M. K. Samantaray, B. Hamzaoui, A. Gurinov, D. H. Anjum, D. Gajan, A. Lesage, A. Bendjeriou-Sedjerari, L. Emsley and J.-M. Basset, *Chem. Sci.*, 2017, **8**, 284–290.

67 D. Xiao, S. Xu, N. J. Brownbill, S. Paul, L.-H. Chen, S. Pawsey, F. Aussenac, B.-L. Su, X. Han, X. Bao, Z. Liu and F. Blanc, *Chem. Sci.*, 2018, **9**, 8184–8193.

68 W. C. Liao, T. C. Ong, D. Gajan, F. Bernada, C. Sauvée, M. Yulikov, M. Pucino, R. Schowner, M. Schwarzwälder, M. R. Buchmeiser, G. Jeschke, P. Tordo, O. Ouari, A. Lesage, L. Emsley and C. Copéret, *Chem. Sci.*, 2017, **8**, 416–422.

69 E. Pump, A. Bendjeriou-Sedjerari, J. Viger-Gravel, D. Gajan, B. Scotto, M. K. Samantaray, E. Abou-Hamad, A. Gurinov, W. Almaksoud, Z. Cao, A. Lesage, L. Cavallo, L. Emsley and J. M. Basset, *Chem. Sci.*, 2018, **9**, 4866–4872.

70 J. P. Majoral and A. M. Caminade, *Chem. Rev.*, 1999, **99**, 845–880.

71 G. A. Olah, *Angew. Chem. Int. Ed.*, 1995, **34**, 1393–1405.

72 G. A. Olah, *J. Am. Chem. Soc.*, 1972, **94**, 808–820.

73 V. B. Kazansky, *Acc. Chem. Res.*, 1991, **24**, 379–383.

74 A. Corma, *Chem. Rev.*, 1995, **95**, 559–614.

75 J. F. Haw, J. B. Nicholas, T. Xu, L. W. Beck and D. B. Ferguson, *Acc. Chem. Res.*, 1996, **29**, 259–267.

76 V. Adeeva, H.-Y. Liu, B.-Q. Xu and W. M. H. Sachtler, *Top. Catal.*, 1998, **6**, 61–76.

77 I. Kiricsi, H. Förster, G. Tasi and J. B. Nagy, *Chem. Rev.*, 1999, **99**, 2085–2114.
78 Y. V. Kissin, *Catal. Rev. Sci. Eng.*, 2001, **43**, 85–146.
79 J. Weitkamp, *ChemCatChem*, 2012, **4**, 292–306.
80 R. R. Naredla and D. A. Klumpp, *Chem. Rev.*, 2013, **113**, 6905–6948.
81 U. Olsbye, S. Svelle, K. P. Lillerud, Z. H. Wei, Y. Y. Chen, J. F. Li, J. G. Wang and W. B. Fan, *Chem. Soc. Rev.*, 2015, **44**, 7155–7176.
82 R. J. Gillespie, T. E. Peel and E. A. Robinson, *J. Am. Chem. Soc.*, 1971, **93**, 5083–5087.
83 G. A. Olah and R. H. Schlosberg, *J. Am. Chem. Soc.*, 1968, **90**, 2726–2727.
84 G. A. Olah, J. S. Staral and G. Liang, *J. Am. Chem. Soc.*, 1974, **96**, 6233–6235.
85 G. A. Olah and D. J. Donovan, *J. Am. Chem. Soc.*, 1977, **99**, 5026–5039.
86 J. F. Haw, B. R. Richardson, I. S. Oshiro, N. D. Lazo and J. A. Speed, *J. Am. Chem. Soc.*, 1989, **111**, 2052–2058.
87 J. B. Nicholas and J. F. Haw, *J. Am. Chem. Soc.*, 1998, **120**, 11804–11805.
88 S. Xu, A. Zheng, Y. Wei, J. Chen, J. Li, Y. Chu, M. Zhang, Q. Wang, Y. Zhou, J. Wang, F. Deng and Z. Liu, *Angew. Chem. Int. Ed.*, 2013, **52**, 11564–11568.
89 W. Dai, C. Wang, X. Yi, A. Zheng, L. Li, G. Wu, N. Guan, Z. Xie, M. Dyballa and M. Hunger, *Angew. Chem. Int. Ed.*, 2015, **54**, 8783–8786.
90 G. Buntkowsky and T. Gutmann, *Angew. Chem. Int. Ed.*, 2015, **54**, 9450–9451.
91 M. Huang, Q. Wang, X. Yi, Y. Chu, W. Dai, L. Li, A. Zheng and F. Deng, *Chem. Commun.*, 2016, **52**, 10606–10608.
92 I. M. Dahl and S. Kolboe, *J. Catal.*, 1994, **149**, 458–464.
93 I. M. Dahl and S. Kolboe, *J. Catal.*, 1996, **161**, 304–309.
94 J. L. White, *Catal. Sci. Technol.*, 2011, **1**, 1630–1635.
95 C. Wang, Y. Chu, A. Zheng, J. Xu, Q. Wang, P. Gao, G. Qi, Y. Gong and F. Deng, *Chem. - A Eur. J.*, 2014, **20**, 12432–12443.
96 P. Tian, Y. Wei, M. Ye and Z. Liu, *ACS Catal.*, 2015, **5**, 1922–1938.
97 B. V Vora, T. L. Marker, P. T. Barger, H. R. Nilsen, S. Kvisle and T. Fuglerud, *Stud. Surf. Sci. Catal.*, 1997, **107**, 87–98.
98 H. Koempel and W. Liebner, *Stud. Surf. Sci. Catal.*, 2007, **167**, 261–267.
99 J. F. Haw, W. Song, D. M. Marcus and J. B. Nicholas, *Acc. Chem. Res.*, 2003, **36**, 317–326.
100 B. Arstad, J. B. Nicholas and J. F. Haw, *J. Am. Chem. Soc.*, 2004, **126**, 2991–3001.
101 D. M. McCann, D. Lesthaeghe, P. W. Kletnieks, D. R. Guenther, M. J. Hayman, M. W. Veronique Van Speybroeck and J. F. Haw, *Angew. Chem. Int. Ed.*, 2008, **47**, 5179–5182.
102 J. F. Haw, P. W. Goguen, T. Xu, T. W. Skloss, W. Song and Z. Wang,

Angew. Chem. Int. Ed., 1998, **37**, 948–949.
103 W. Song, J. B. Nicholas and J. F. Haw, *J. Am. Chem. Soc.*, 2001, **123**, 121–129.
104 M. Zhang, S. Xu, J. Li, Y. Wei, Y. Gong, Y. Chu, A. Zheng, J. Wang, W. Zhang, X. Wu, F. Deng and Z. Liu, *J. Catal.*, 2016, **335**, 47–57.
105 C. Wang, X. Yi, J. Xu, G. Qi, P. Gao, W. Wang, Y. Chu, Q. Wang, N. Feng, X. Liu, A. Zheng and F. Deng, *Chem. - A Eur. J.*, 2015, **21**, 12061–12068.
106 D. Xiao, S. Xu, X. Han, X. Bao, Z. Liu and F. Blanc, *Chem. Sci.*, 2017, **8**, 8309–8314.
107 M. Stöcker, *Microporous Mesoporous Mater.*, 1999, **29**, 3–48.
108 U. Olsbye, S. Svelle, M. Bjørgen, P. Beato, T. V. W. Janssens, F. Joensen, S. Bordiga and K. P. Lillerud, *Angew. Chem. Int. Ed.*, 2012, **51**, 5810–5831.
109 C. Wang, Q. Wang, J. Xu, G. Qi, P. Gao, W. Wang, Y. Zou, N. Feng, X. Liu and F. Deng, *Angew. Chem. Int. Ed.*, 2016, **55**, 2507–2511.
110 A. D. Chowdhury, K. Houben, G. T. Whiting, M. Mokhtar, A. M. Asiri, S. A. Al-Thabaiti, S. N. Basahel, M. Baldus and B. M. Weckhuysen, *Angew. Chem. Int. Ed.*, 2016, **55**, 15840–15845.
111 Y. Liu, S. Müller, D. Berger, J. Jelic, K. Reuter, M. Tonigold, M. Sanchez-Sanchez and J. A. Lercher, *Angew. Chem. Int. Ed.*, 2016, **55**, 5723–5726.
112 X. Wu, S. Xu, W. Zhang, J. Huang, J. Li, B. Yu, Y. Wei and Z. Liu, *Angew. Chem. Int. Ed.*, 2017, **56**, 9039–9043.
113 J. D. A. Pelletier and J.-M. Basset, *Acc. Chem. Res.*, 2016, **49**, 664–677.
114 F. Blanc, R. Berthoud, C. Copéret, A. Lesage, L. Emsley, R. Singh, T. Kreickmann and R. R. Schrock, *Proc. Natl. Acad. Sci.*, 2008, **105**, 12123–12127.
115 F. Blanc, C. Copéret, A. Lesage and L. Emsley, *Chem. Soc. Rev.*, 2008, **37**, 518–526.
116 W. Zhang, S. Xu, X. Han and X. Bao, *Chem. Soc. Rev.*, 2012, **41**, 192–210.
117 C. Copéret, A. Comas-Vives, M. P. Conley, D. P. Estes, A. Fedorov, V. Mougel, H. Nagae, F. Núñez-Zarur and P. A. Zhizhko, *Chem. Rev.*, 2016, **116**, 323–421.
118 J. Li, Y. Wei, J. Chen, P. Tian, X. Su, S. Xu, Y. Qi, Q. Wang, Y. Zhou, Y. He and Z. Liu, *J. Am. Chem. Soc.*, 2012, **134**, 836–839.
119 M. Bjørgen, U. Olsbye, D. Petersen and S. Kolboe, *J. Catal.*, 2004, **221**, 1–10.
120 C. Bonhomme, C. Gervais, F. Babonneau, C. Coelho, F. Pourpoint, T. Azaïs, S. E. Ashbrook, J. M. Griffin, J. R. Yates, F. Mauri and C. J. Pickard, *Chem. Rev.*, 2012, **112**, 5733–5779.
121 S. E. Ashbrook and D. M. Dawson, *Acc. Chem. Res.*, 2013, **46**, 1964–1974.

122 X. Lu, O. Lafon, J. Trébosc and J.-P. Amoureux, *J. Magn. Reson.*, 2012, **215**, 34–49.
123 F. Pourpoint, J. Trébosc, R. M. Gauvin, Q. Wang, O. Lafon, F. Deng and J.-P. Amoureux, *ChemPhysChem*, 2012, **13**, 3605–3615.
124 C. Baerlocher and L. B. McCusker, Database of Zeolite Structures, http://www.iza-structure.org/databases/.
125 C. Baerlocher, L. B. McCusker and D. H. Olson, *Atlas of Zeolite Framework Types, 6th revised edition*, Elsevier, 2007.
126 A. Brinkmann and A. P. M. Kentgens, *J. Am. Chem. Soc.*, 2006, **128**, 14758–14759.
127 T. Gullion and J. Schaefer, *J. Magn. Reson.*, 1989, **81**, 196–200.
128 M. Bertmer and H. Eckert, *Solid State Nucl. Magn. Reson.*, 1999, **15**, 139–152.
129 M. Bjørgen, S. Svelle, F. Joensen, J. Nerlov, S. Kolboe, F. Bonino, L. Palumbo, S. Bordiga and U. Olsbye, *J. Catal.*, 2007, **249**, 195–207.
130 S. Ilias and A. Bhan, *J. Catal.*, 2012, **290**, 186–192.
131 P. Dejaifve, J. C.Védrine, V. Bolis and E. G.Derouane, *J. Catal.*, 1980, **63**, 331–345.
132 W. Dai, C. Wang, M. Dyballa, G. Wu, N. Guan, L. Li, Z. Xie and M. Hunger, *ACS Catal.*, 2015, **5**, 317–326.
133 Z. W. Qiu, D. M. Grant and R. J. Pugmire, *J. Am. Chem. Soc.*, 1982, **104**, 2747–2753.
134 D. Freude, H. Ernst and I. Wolf, *Solid State Nucl Magn Reson*, 1994, **3**, 271–286.
135 Q. Wang, S. Xu, J. Chen, Y. Wei, J. Li, D. Fan, Z. Yu, Y. Qi, Y. He, S. Xu, C. Yuan, Y. Zhou, J. Wang, M. Zhang, B. Su and Z. Liu, *RSC Adv.*, 2014, **4**, 21479–21491.
136 S. de Monredon–Senani, C. Bonhomme, F. Ribot and F. Babonneau, *J. Sol-Gel Sci. Technol.*, 2009, **50**, 152–157.
137 J. F. Haw and D. M. Marcus, *Top. Catal.*, 2005, **34**, 41–48.
138 R. Y. Brogaard, B. M. Weckhuysen and J. K. Nørskov, *J. Catal.*, 2013, **300**, 235–241.
139 C. Raksakoon and J. Limtrakul, *J. Mol. Struct. THEOCHEM*, 2003, **631**, 147–156.
140 R. Rungsirisakun, B. Jansang, P. Pantu and J. Limtrakul, *J. Mol. Struct.*, 2005, **733**, 239–246.
141 J. F. Haw, J. B. Nicholas, W. Song, F. Deng, Z. Wang, T. Xu and C. S. Heneghan, *J. Am. Chem. Soc.*, 2000, **122**, 4763–4775.
142 H. Fang, A. Zheng, J. Xu, S. Li, Y. Chu, L. Chen and F. Deng, *J. Phys. Chem. C*, 2011, **115**, 7429–7439.
143 D. Xiao, X. Han, X. Bao, G. Hou and F. Blanc, *RSC Adv.*, 2019, **9**, 12415–12418.
144 S. Xu, Y. Zhi, J. Han, W. Zhang, X. Wu, T. Sun, Y. Wei and Z. Liu, *Advances in Catalysis for Methanol-to-Olefins Conversion*, Elsevier Inc.,

2017, vol. 61.
145 I. Yarulina, A. D. Chowdhury, F. Meirer, B. M. Weckhuysen and J. Gascon, *Nat. Catal.*, 2018, **1**, 398–411.
146 F. Bleken, M. Bjørgen, L. Palumbo, S. Bordiga, S. Svelle, K. P. Lillerud and U. Olsbye, *Top. Catal.*, 2009, **52**, 218–228.
147 M. J. Wulfers and F. C. Jentoft, *ACS Catal.*, 2014, **4**, 3521–3532.
148 W. Song, J. B. Nicholas and J. F. Haw, *J. Phys. Chem. B*, 2001, **105**, 4317–4323.
149 R. Fu, S. A. Smith and G. Bodenhausen, *Chem. Phys. Lett.*, 1997, **272**, 361–369.
150 G. Metz, X. Wu and S. O. Smith, *J. Magn. Reson. Ser. A*, 1994, **110**, 219–227.
151 W. Zhang, J. Chen, S. Xu, Y. Chu, Y. Wei, Y. Zhi, J. Huang, A. Zheng, X. Wu, X. Meng, F. Xiao, F. Deng and Z. Liu, *ACS Catal.*, 2018, **8**, 10950–10963.
152 G. A. Olah and G. Liang, *J. Am. Chem. Soc.*, 1972, **94**, 6434–6441.
153 S. Bordiga, L. Regli, D. Cocina, C. Lamberti, M. Bjørgen and K. P. Lillerud, *J. Phys. Chem. B*, 2005, **109**, 2779–2784.
154 Y. Wei, J. Li, C. Yuan, S. Xu, Y. Zhou, J. Chen, Q. Wang, Q. Zhang and Z. Liu, *Chem. Commun.*, 2012, **48**, 3082–3084.
155 P. R. Seidl, K. Z. Leal and J. D. Yoneda, *J. Phys. Org. Chem.*, 2002, **15**, 801–807.
156 US Patent, 9586197, 2017.
157 US Patent, 9611203, 2017.
158 X.-Y. Yang, L.-H. Chen, Y. Li, J. C. Rooke, C. Sanchez and B.-L. Su, *Chem. Soc. Rev.*, 2017, **46**, 481–558.
159 L.-H. Chen, X.-Y. Li, G. Tian, Y. Li, H.-Y. Tan, G. Van Tendeloo, G.-S. Zhu, S.-L. Qiu, X.-Y. Yang and B.-L. Su, *ChemSusChem*, 2011, **4**, 1452–1456.
160 K. R. Thurber and R. Tycko, *J. Magn. Reson.*, 2009, **196**, 84–87.
161 C. R. Morcombe, V. Gaponenko, R. A. Byrd and K. W. Zilm, *J. Am. Chem. Soc.*, 2004, **126**, 7196–7197.
162 A. L. Webber, A. J. Pell, E. Barbet-Massin, M. J. Knight, I. Bertini, I. C. Felli, R. Pierattelli, L. Emsley, A. Lesage and G. Pintacuda, *ChemPhysChem*, 2012, **13**, 2405–2411.
163 D. Massiot, F. Fayon, M. Capron, I. King, S. Le Calvé, B. Alonso, J.-O. Durand, B. Bujoli, Z. Gan and G. Hoatson, *Magn. Reson. Chem.*, 2002, **40**, 70–76.
164 F. M. Vigier, D. Shimon, V. Mugnaini, J. Veciana, A. Feintuch, M. Pons, S. Vega and D. Goldfarb, *Phys. Chem. Chem. Phys.*, 2014, **16**, 19218–19228.
165 N. J. Brownbill, B. B. Reiner Sebastian Sprick, S. Pawsey, F. Aussenac, A. J. Fielding, A. I. Cooper and F. Blanc, *Macromolecules*, 2018, **51**, 3088–3096.

166 H. Takahashi, D. Lee, L. Dubois, M. Bardet, S. Hediger and G. De Paëpe, *Angew. Chem. Int. Ed.*, 2012, **51**, 11766–11769.
167 K. R. Thurber and R. Tycko, *J. Chem. Phys.*, 2014, **140**, 184201.
168 F. Mentink-Vigier, S. Paul, D. Lee, A. Feintuch, S. Hediger, S. Vega and G. De Paëpe, *Phys. Chem. Chem. Phys.*, 2015, **17**, 21824–21836.
169 S. R. Chaudhari, P. Berruyer, D. Gajan, C. Reiter, F. Engelke, D. L. Silverio, C. Copéret, M. Lelli, A. Lesage and L. Emsley, *Phys. Chem. Chem. Phys.*, 2016, **18**, 10616–10622.
170 F. Mentink-Vigier, G. Mathies, Y. Liu, A.-L. Barra, M. A. Caporini, D. Lee, S. Hediger, R. G. Griffin and G. De Paëpe, *Chem. Sci.*, 2017, **8**, 8150–8163.
171 S. R. Chaudhari, D. Wisser, A. C. Pinon, P. Berruyer, D. Gajan, P. Tordo, O. Ouari, C. Reiter, F. Engelke, C. Copéret, M. Lelli, A. Lesage and L. Emsley, *J. Am. Chem. Soc.*, 2017, **139**, 10609–10612.
172 N. J. Brownbill, D. Gajan, A. Lesage, L. Emsley and F. Blanc, *Chem. Commun.*, 2017, **53**, 2563–2566.
173 C. Copéret, W. C. Liao, C. P. Gordon and T.-C. Ong, *J. Am. Chem. Soc.*, 2017, **139**, 10588–10596.
174 A. H. Linden, W. T. Franks, Ü. Akbey, S. Lange, B. J. Van Rossum and H. Oschkinat, *J. Biomol. NMR*, 2011, **51**, 283–292.
175 W. Song, J. B. Nicholas, A. Sassi and J. F. Haw, *Catal. Letters*, 2002, **81**, 49–53.
176 M. Bjørgen, U. Olsbye, S. Svelle and S. Kolboe, *Catal. Letters*, 2004, **93**, 37–40.
177 M. Bjørgen, S. Akyalcin, U. Olsbye, S. Benard, S. Kolboe and S. Svelle, *J. Catal.*, 2010, **275**, 170–180.
178 K. Lammertsma and H. Cerfontain, *J. Am. Chem. Soc.*, 1979, **101**, 3618–3624.
179 K. Lammertsma, *J. Am. Chem. Soc.*, 1981, **103**, 2062–2069.
180 K. Hemelsoet, A. Nollet, V. Van Speybroeck and M. Waroquier, *Chem. - A Eur. J.*, 2011, **17**, 9083–9093.
181 E. Borodina, F. Meirer, I. Lezcano-González, M. Mokhtar, A. M. Asiri, S. A. Al-Thabaiti, S. N. Basahel, J. Ruiz-Martinez and B. M. Weckhuysen, *ACS Catal.*, 2015, **5**, 992–1003.
182 W. Song, H. Fu and J. F. Haw, *J. Phys. Chem. B*, 2001, **105**, 12839–12843.
183 M. Bjørgen, U. Olsbye and S. Kolboe, *J. Catal.*, 2003, **215**, 30–44.
184 K. H. Abhishek Dutta Chowdhury, Alessandra Lucini Paioni, G. T. Whiting, M. Baldus and B. M. Weckhuysen, *Angew. Chem. Int. Ed.*, 2018, **57**, 8095–8099.
185 X. Wu, S. Xu, Y. Wei, W. Zhang, J. Huang, S. Xu, Y. He, S. Lin, T. Sun and Z. Liu, *ACS Catal.*, 2018, **8**, 7356–7361.
186 I. B. Minova, S. K. Matam, A. Greenaway, C. R. A. Catlow, M. D. Frogley, G. Cinque, P. A. Wright and R. F. Howe, *ACS Catal.*, 2019, **9**, 6564–

6570.
187 D. Lesthaeghe, J. Van der Mynsbrugge, M. Vandichel, M. Waroquier and V. Van Speybroeck, *ChemCatChem*, 2011, **3**, 208–212.
188 T. I. Korányi and J. B. Nagy, *J. Phys. Chem. B*, 2005, **109**, 15791–15797.
189 J. Pérez-Pariente, J. Sanz, V. Fornés and A. Corma, *J. Catal.*, 1990, **124**, 217–223.
190 M.-H. Sun, S.-Z. Huang, L.-H. Chen, Y. Li, X.-Y. Yang, Z.-Y. Yuan and B.-L. Su, *Chem. Soc. Rev.*, 2016, **45**, 3479–3563.
191 Z. Wang, Y. Jiang, O. Lafon, J. Trébosc, K. Duk Kim, C. Stampfl, A. Baiker, J. P. Amoureux and J. Huang, *Nat. Commun.*, 2016, **7**, 13820.
192 C. Wang, Y. Chu, J. Xu, Q. Wang, G. Qi, P. Gao, X. Zhou and F. Deng, *Angew. Chem. Int. Ed.*, 2018, **57**, 10197–10201.
193 X. Yi, K. Liu, W. Chen, J. Li, S. Xu, C. Li, Y. Xiao, H. Liu, X. Guo, S. Bin Liu and A. Zheng, *J. Am. Chem. Soc.*, 2018, **140**, 10764–10774.
194 L. Peng, Y. Liu, N. Kim, J. E. Readman and C. P. Grey, *Nat. Mater.*, 2005, **4**, 216–219.